

## 1 Mechanical Properties of Graphene

2 Y.W. Sun,<sup>1, a)</sup> D.G. Papageorgiou,<sup>1, b)</sup> C.J. Humphreys,<sup>1, c)</sup> D.J. Dunstan,<sup>2, d)</sup> P.  
3 Puech,<sup>3, e)</sup> J.E. Proctor,<sup>4, f)</sup> C. Bousige,<sup>5, g)</sup> D. Machon,<sup>6, h)</sup> and A. San-Miguel<sup>6, i)</sup>

4 <sup>1)</sup>*School of Engineering and Materials Science, Queen Mary University of London,*  
5 *London E1 4NS, United Kingdom*

6 <sup>2)</sup>*School of Physics and Astronomy, Queen Mary University of London,*  
7 *London E1 4NS, United Kingdom*

8 <sup>3)</sup>*CEMES/CNRS UPR8011, University of Toulouse, F-31055 Toulouse,*  
9 *France*

10 <sup>4)</sup>*School of Science, Engineering and Environment, University of Salford,*  
11 *Manchester M5 4WT, United Kingdom*

12 <sup>5)</sup>*Laboratoire des Multimatériaux et Interfaces, UMR CNRS 5615,*  
13 *Univ. Lyon, Université Claude Bernard Lyon 1, F-69622 Villeurbanne,*  
14 *France*

15 <sup>6)</sup>*Université de Lyon, F-69000 Lyon, France and Institut Lumière Matière,*  
16 *CNRS, UMR 5306, Université Lyon 1, F-69622 Villeurbanne,*  
17 *France*

18 (Dated: 9 April 2021)

19 The mechanical properties of graphene are reviewed with particular attention to what  
20 is established and what is still uncertain. The thickness and the elastic constants are  
21 clarified, and by considering also phonon frequencies it is argued that “best values”  
22 come from graphite, when available. Properties not available from graphite include  
23 the bending stiffness; this can be determined from studies of carbon nanotubes as  
24 well as graphene. In many ways nanotubes provide access to fundamental properties  
25 of graphene, not least as they are the only form of graphene that can be unsupported  
26 (unstrained) in vacuum. Environmental effects are considered, both interactions with  
27 substrates and with other solid and liquid media which may affect the geometrical  
28 parameters defining graphene and associated elastic constant. Major uncertainties  
29 persist whether slipping or sticking dominates experimental observation, both be-  
30 tween graphene and solid media, and between the layers of bilayer and multilayer  
31 graphene. The paper concludes with a short discussion of continuum and atomistic  
32 models of graphene.

---

a) [yiwei.sun@qmul.ac.uk](mailto:yiwei.sun@qmul.ac.uk)

b) [d.papageorgiou@qmul.ac.uk](mailto:d.papageorgiou@qmul.ac.uk)

c) [c.humphreys@qmul.ac.uk](mailto:c.humphreys@qmul.ac.uk)

d) [d.dunstan@qmul.ac.uk](mailto:d.dunstan@qmul.ac.uk)

e) [pascal.puech@cemes.fr](mailto:pascal.puech@cemes.fr)

f) [j.e.proctor@salford.ac.uk](mailto:j.e.proctor@salford.ac.uk)

g) [colin.bousige@univ-lyon1.fr](mailto:colin.bousige@univ-lyon1.fr)

h) [denis.machon@univ-lyon1.fr](mailto:denis.machon@univ-lyon1.fr)

i) [alfonso.san-miguel@univ-lyon1.fr](mailto:alfonso.san-miguel@univ-lyon1.fr)

## 33 CONTENTS

34	<b>I. Introduction</b>	5
35	<b>II. Basic properties</b>	5
36	A. Thickness of graphene	6
37	B. Graphene elastic stiffness tensor	7
38	<b>III. Graphene reference mechanical properties</b>	8
39	A. Graphite 3D mechanical properties	8
40	B. In-plane graphene mechanical properties	9
41	C. Out-of-plane stiffness of graphene	11
42	D. Properties not related to graphite	12
43	1. Acoustic phonons in graphene; their effect on the thermal expansion and	
44	stability of graphene samples	13
45	2. Mechanical stability of graphene	13
46	3. Thermal expansion coefficient of graphene	17
47	4. Grüneisen parameters and elastic bands	20
48	5. Bending stiffness	20
49	6. Folding	22
50	7. Shearing, sliding and friction between graphene layers	23
51	<b>IV. Measuring graphene mechanical properties</b>	24
52	A. Atomic force microscopy	24
53	B. Raman spectroscopy	27
54	C. <i>In situ</i> tensile tests	28
55	D. Pressurized blister method	29
56	E. Inelastic X-ray scattering	30
57	F. Density functional theory	31
58	<b>V. Graphene in interaction with its environment at high pressure</b>	33
59	A. Suspended graphene in a fluid PTM	34
60	B. Supported Graphene in a fluid PTM	37
61	1. Role of the substrate	38

62	2. Role of the PTM	42
63	C. Graphene sandwiched between two solids	43
64	1. Different solids	43
65	2. Identical solids	44
66	<b>VI. Dressed graphene</b>	46
67	A. Functionalisation	46
68	B. Derivative geometry	46
69	C. Effect of vdW interactions	47
70	<b>VII. Carbon nanotubes: Properties of graphene</b>	51
71	A. G-mode in nanotubes	52
72	B. RBM in nanotubes	53
73	C. SWCNTs under pressure	54
74	D. SWCNT Collapse	55
75	E. DWCNTs coefficients under pressure	56
76	<b>VIII. Models for the mechanics of graphene</b>	59
77	<b>IX. Conclusions</b>	62
78	<b>Acknowledgments</b>	63
79	<b>Data availability</b>	63
80	<b>References</b>	63

## 81 I. INTRODUCTION

82 Graphene has attracted enormous attention (*e.g.* the 2010 Nobel Prize) and research  
83 effort, because of its extraordinary properties, not the least of which is its two-dimensional  
84 (2D) nature. While many layered materials such as graphite and MoS<sub>2</sub> were already known,  
85 graphene was the first material in which all the atoms are in a single plane – so for theoreticians,  
86 at least, who may ignore the electrons and consider the carbon nuclei as point masses,  
87 it is a genuinely 2D material. Yet it is also a very familiar material. It is the material that  
88 in stacks of millions or billions of layers, constitutes graphite, much as many sheets of paper  
89 make a book.

90 There are many excellent review articles that cover the mechanical properties of graphene,  
91 both experimental and theoretical, and which to be comprehensive have to have about 500  
92 references.<sup>1-3</sup> Why another? Our purpose is different. We aim to clarify points that are often  
93 confused in the literature, and where we deem appropriate to identify problems that are as  
94 yet unsolved. Some properties of graphene are just what one might expect, given what we  
95 know of graphite. Here we review primarily the accuracy to which this is known. Second,  
96 some properties are expected to be different, for reasons that are understood. Third, and  
97 perhaps most interesting, are the anomalies. By this, we mean the behaviours of graphene  
98 that are well-established experimentally, yet which lack adequate explanation according to  
99 our current understanding.

100 An interesting question is “to which extent is the continuum mechanics view applicable  
101 to graphene?” Of course, this leads to the definition of a thickness for graphene, which is  
102 comparable to trying to define the thickness of an atom. The quantum nature of matter,  
103 predominant at this scale, will obviously only lead to an approximate or to a probabilistic  
104 answer.

## 105 II. BASIC PROPERTIES

106 The most basic properties determining the mechanical behaviour of a piece of a mate-  
107 rial are its physical dimensions and its elastic moduli. But how can we define or measure  
108 these mechanical properties of graphene? This apparently naive question arises from the  
109 fact that the one-atom-thick character of graphene challenges the science of the mechanics

110 of materials, a discipline based on continuum mechanics and which has developed its suc-  
111 cessful non-atomistic view since the publication of the first book addressing the strength of  
112 materials, “Two New Sciences”, written by Galileo Galilei in 1638.<sup>4</sup> Of course, the discipline  
113 has subsequently integrated the atomistic nature of materials into its thinking, as in the  
114 concepts of theoretical strength and of dislocations, and in the use of molecular dynamics  
115 (MD) and density-functional (DFT) modelling.

116 From the material mechanics point of view, a large part of the challenge of graphene  
117 mechanics arises from the ambiguities of defining the thickness of a structure – here a one-  
118 atom-thick surface. From this point of view, it is important to recognise that thickness is  
119 not a material property, but a property of a structure, such as a plate. Moreover, even a  
120 simple structure such as a corrugated-iron roofing sheet has more than one property equally  
121 deserving of being called the thickness – maybe the 0.5 mm thickness of the sheet, maybe  
122 the 30 mm depth of the corrugations. So the issue is not to define what the thickness of  
123 graphene is, but to be clear what the context is and how the concept of thickness enters in, in  
124 each context. If one wants to stack  $n$  corrugated-iron sheets at random angles, the height of  
125 a stack of  $n$  sheets will be  $30 \times n$  mm, while if they are aligned, the stack will be  $0.5 \times n$  mm  
126 high. So graphene in AB stacking as in graphite has a thickness of  $3.35 \text{ \AA}$ , unambiguously.  
127 We should not be surprised if this value changes for other stackings<sup>5</sup> (*e.g.* around  $3.6 \text{ \AA}$  for  
128 random-angle stacking called turbostratic, and see Table I for some graphene thicknesses  
129 as described by the distances from various substrates). Nevertheless, while the stacking of  
130 corrugated-iron sheets may have no bearing on the physical characteristics of the individual  
131 sheets, this can be a totally different issue for graphene. Depending on the geometrical  
132 arrangements, modifications of the electronic structure of the individual graphene sheets  
133 could be significant.

## 134 A. Thickness of graphene

135 The thickness of graphene is a vexed question. The common description of graphene as  
136 a 2D material implies extension in two dimensions but not in the third (*i.e.* zero thickness).  
137 Indeed, the very definition of the thickness of graphene is complicated from a quantum  
138 mechanics point of view, as it pertains to defining the diameter of atoms. The Yakobson  
139 paradox<sup>6</sup> arose through the attribution of values as low as  $0.6 \text{ \AA}$  to the thickness – and hence

140 Young’s moduli as high as 5 TPa. It is interesting to see how the similar issue of the size of  
141 atoms was addressed a century ago.

142 Sir William Bragg proposed the hypothesis that atoms of a given element could be con-  
143 sidered to be spheres with a fixed radius.<sup>7</sup> However, the crystal structures of some metals  
144 and compounds led to proposals that some atoms have lower symmetry than spherical.<sup>8</sup>  
145 Wyckoff re-examined the question and concluded that the hypothesis of constant radii (or  
146 other shapes with fixed sizes) must be rejected but that the evidence supported atomic radii  
147 that vary more or less according to their environment.<sup>9</sup> This is the basis of the modern view.  
148 Modern data compilations give for example the covalent radius of the carbon atom as 0.70  
149 Å. More precisely, the covalent radius of carbon is largest for single-bonded carbon with the  
150 C-C bonds in ethane and diamond both at 1.54 Å, smaller for sp<sup>2</sup>-bonded (graphite at 1.42  
151 Å and ethene at 1.33 Å bond length) and smallest for triple-bonded carbon (acetylene, 1.20  
152 Å). On the other hand, the van der Waals (vdW) radius of a carbon atom is given as 1.70  
153 Å. An early measurement of the thickness of the benzene molecule gave 4.70 Å,<sup>10</sup> while the  
154 thickness of the larger pyrene molecule is 3.53 Å,<sup>11</sup> very close to the spacing of the graphene  
155 sheets in graphite at 3.35 Å.

156 These considerations appear to give a clear meaning to the concept of the vdW thickness  
157 of graphene, as much as of simpler molecules such as benzene and the higher polycyclic  
158 aromatic compounds such as pyrene. It expresses the distance of closest approach of other  
159 physisorbed atoms – whether carbon or anything else, because the repulsive interatomic  
160 potential deriving from Pauli exclusion is largely independent of the nature of the interacting  
161 atoms, and in the absence of a chemical bond, so is the vdW attractive potential. Following  
162 Wyckoff,<sup>9</sup> the thickness should be expected to vary with the environment, whether it is a  
163 surrounding gas or a substrate, as can be seen in Table I – even quite considerably as the  
164 vdW forces, while always weak, can vary by an order of magnitude.

## 165 B. Graphene elastic stiffness tensor

166 Only in graphite is graphene found in a symmetrical environment (sandwiched between  
167 graphene sheets with only a vdW potential binding them) and with a known thickness. We  
168 may then define the graphene elastic stiffness constants  $c_{ij}$  in this situation as a reference  
169 system. To deal with possible variations in thickness in other environments, it makes sense

TABLE I. Experimental graphene-substrate distance for various substrates.

Substrate	Distance [Å]
Ir(111) <sup>12</sup>	3.38
Graphite	3.35
Pt(111) <sup>13</sup>	3.30
SiC(0001) <sup>14</sup>	3.24
Ru(0001) <sup>15</sup>	2.2
Co(0001) <sup>16</sup>	2.2
Ni(111) <sup>17,18</sup>	2.1

170 to define the in-plane 2D elastic stiffness tensor  $c_{ij}^{2D} = c_{ij}d_0$  with  $i, j = 1, 2$ , and  $d_0$  is the  
 171 graphite interlayer spacing at ambient pressure. This tensor comes simply from the  $sp^2$  bond  
 172 bending and stretching stiffnesses, and so is independent of the graphene thickness  $d$  *per se*.  
 173 To see this, consider making the graphene layers in graphite thinner, spaced more closely  
 174 and reducing  $a_{33}$ , as happens under pressure. Then there are more graphene layers per  
 175 unit volume,  $a_{33}^{-1}$ , and the 3D constants  $c_{11}$  and  $c_{12}$  are increased proportionately – leaving  
 176  $c_{ij}^{2D}$  unchanged. The out-of-plane elastic constants, particularly  $c_{33}$  but also  $c_{13}$ , have to be  
 177 considered separately. This is done in Sec. III C.

178 A crucial aspect is then to know if the graphene  $sp^2$  bonds – which largely determine  
 179  $c_{ij}^{2D}$  – are significantly influenced either by the environment of the graphene (what it is in  
 180 contact with) or by its geometry (for example, bending) leading to a modification of the  
 181 reference elastic stiffness constants. The zeroth-order approximation would be that there  
 182 are no such influences. But if there are, we will need also to consider what are the limits  
 183 in such modifications which can be admitted before saying that we are dealing with a new  
 184 system. These issues are addressed in Sec. VI.

### 185 III. GRAPHENE REFERENCE MECHANICAL PROPERTIES

#### 186 A. Graphite 3D mechanical properties

187 Graphite consists of a macroscopic multilayer stack of graphene layers, held apart by the  
 188  $\pi$ -orbitals and Pauli exclusion, and held together by the vdW interaction, with a spacing of

189 3.35 Å.<sup>19</sup> It is, consequently, highly anisotropic, while being isotropic in-plane. The elastic  
 190 moduli reported in Table II were obtained from inelastic X-ray scattering,<sup>20</sup> but similar  
 191 values were reported from ultrasonic and static mechanical testing.<sup>21</sup>

TABLE II. Elastic moduli values obtained from inelastic X-ray scattering<sup>20</sup> in Voigt notation

	$c_{ij}$ [GPa]	$c_{ij}^{2D}$ [Nm <sup>-1</sup> ]
$c_{11}$	$1109 \pm 16$	$372 \pm 5$
$c_{33}$	$38.7 \pm 0.7$	
$c_{12}$	$139 \pm 36$	$47 \pm 12$
$c_{13}$	$0 \pm 3$	
$c_{44}$	$5 \pm 0.3$	
$c_{66}$	$485 \pm 10$	
$Y$	$1092 \pm 18$	$362 \pm 27$
$\nu$	$0.125 \pm 0.033$	(no units)

192 Within experimental error, the  $c_{13}$  of graphite may be negative – and DFT calculations  
 193 support this.<sup>22</sup> While DFT may not evaluate the interlayer spacing accurately without vdW  
 194 correction,<sup>23</sup> the related elastic constant  $c_{33}$  calculated at the experimental equilibrium spac-  
 195 ing agrees well with the experimental  $c_{33}$ . That improves confidence in the reliability of the  
 196 negative calculated value of  $c_{13}$ .<sup>22</sup> If  $c_{13}$  is truly negative, it might be due to ripples in  
 197 the measured graphite sample, like what happens with auxetics, prominent structures that  
 198 have negative Poisson’s ratio.<sup>24</sup> This could be further linked to the negative thermal ex-  
 199 pansion of graphene, which will be discussed later. In a general 3D anisotropic medium,  
 200 the Young’s moduli for a stress  $\sigma_{11}$  are given by more complicated expressions than the  
 201 usual  $Y = c_{11} - 2c_{12}^2/(c_{11} + c_{12})$ . The small or vanishing value of  $c_{13}$  simplifies this to  
 202  $Y = c_{11} - c_{12}^2/c_{11}$  for the in-plane Young’s modulus of graphene. Similarly the in-plane  
 203 Poisson’s ratio simplifies to  $\nu = c_{12}/c_{11}$ .

## 204 B. In-plane graphene mechanical properties

205 Under the hypothesis that graphene can be treated as a continuous elastic medium, it  
 206 is thus expected to have the 3D values given in Table II and hence the  $c_{ij}^{2D}$  values also

207 given there. Indeed, the in-plane Young’s modulus  $Y^{2D} = 362 \text{ Nm}^{-1}$  is consistent with  
208 the  $Y^{2D} = 340 \pm 50 \text{ Nm}^{-1}$  of monolayer freestanding graphene measured by atomic force  
209 microscopy (AFM)<sup>25</sup>, which will be discussed in Sec. IV A.

210 For graphene in vacuum, the greatest difference from graphite is likely to be an increase  
211 in the thickness, as the  $\pi$ -orbitals are no longer compressed by the vdW attractive force –  
212 indeed, as discussed above, the thickness becomes defined by whatever convention is used  
213 to specify where the  $\pi$ -orbitals end. The 3D elastic constants will vary inversely with the  
214 thickness. The 2D elastic constants are unaffected. Neglecting any small effect on the  $\text{sp}^2$   
215 bond strength caused by the relaxation of the  $\pi$ -orbitals, and any small contribution of  
216 the  $\pi$ -bonds to  $c_{11}$  and  $c_{12}$ , the 2D elastic constants will be unchanged; they are mostly  
217 determined by the carbon  $\text{sp}^2$ -network.<sup>26</sup>

218 Direct experimental determinations of the in-plane elastic constants of graphene are much  
219 less accurate than those of graphite, but are generally consistent with them within experi-  
220 mental uncertainty (see Sec. IV). The results of *ab initio* theoretical calculations also show  
221 very similar in-plane elastic constants of graphene to graphite, with the caveat that it is  
222 much harder to assess the uncertainty of these calculations than to assess experimental  
223 uncertainties.<sup>22</sup>

224 Given the large uncertainties on experimental determinations of  $c_{ij}^{2D}$  in graphene, the  
225 best information about possible perturbations of the in-plane  $\text{sp}^2$  bonding comes from a  
226 comparison of the phonon frequencies, and in particular the zone-centre  $E_{2g}$  optical phonon.  
227 It is a Raman active mode, named the G-mode (G for graphite), at about  $1600 \text{ cm}^{-1}$  in all  
228  $\text{sp}^2$ -bonded forms of carbon.<sup>27</sup> In graphite, the frequency of the G-mode is at  $1575 - 1580$   
229  $\text{cm}^{-1}$ ,<sup>27–30</sup> and it is reported at  $1581 - 1592 \text{ cm}^{-1}$  in graphene.<sup>31–34</sup> This difference of about  
230 0.5% puts an upper limit of about 1% on any change in the stiffness of the  $\text{sp}^2$  bonds or  $c_{ij}^{2D}$   
231 in going from graphite to graphene.

232 Chemical perturbations such as [substitutional doping and](#) doping by charge transfer from  
233 a substrate or nitric acid, etc, mechanical perturbations such as bending, stretching or high  
234 pressure, or structural perturbations such as stacking order, again scarcely perturb the GM  
235 frequency [relative to graphite](#), a few tens of  $\text{cm}^{-1}$  at most. The  $\text{sp}^2$  covalent bonding is  
236 clearly robust. This is actually true of small molecules generally, which like graphene are  
237 “all surface”, yet whose vibrational frequencies are little affected from the vapour phase,  
238 through solvation or liquefaction, to crystalline solid forms. It is not surprising, then, that

239 this is so for graphene. Of course, the concept of a material that is all surface is not novel;  
240 chemistry deals largely with such things. Some readers might be alerted here that shift of  
241 tens of  $\text{cm}^{-1}$  in the G-mode could be considered to be huge in specific studies, but when  
242 considering the corresponding change in the in-plane stiffness, such shifts are still very little  
243 compared to the large experimental uncertainties from the direct measurements on graphene  
244 by AFM (Sec. IV A).

245 We conclude that graphene and graphite are the same regarding in-plane stiffness within  
246 experimental uncertainty, from the G-mode frequency. More details about the G-mode  
247 frequency, such as the contributions from the deformed  $\pi$ -orbitals and up to the fifth nearest  
248 neighbour C atoms, will be discussed in Sec. VIC and VIII, respectively.

### 249 C. Out-of-plane stiffness of graphene

250 On the assumption that graphene has the vdW thickness equal to the interlayer spacing  
251 of graphite (Sec. II A), we may suppose that it has a stiffness in that direction, equal to that  
252 of graphite,  $38.7 \pm 0.7$  GPa.<sup>20</sup> This basic assumption is challenged by various objections.  
253 For example, in graphite,  $c_{33}$  probes the interlayer potentials defined through the  $\pi$ -orbital  
254 interaction in an AB stacking. What sense does this make when considering graphene in  
255 vacuum or in a solid or liquid molecular environment? Deformation of solids is usually  
256 described in terms of the changes in the distances between atoms, measured from nuclei to  
257 nuclei, or in crystals, by the spacing of planes of atomic nuclei. It could be argued that with  
258 only one plane of atoms, one plane of nuclei, out-of-plane deformation or strain of graphene  
259 is meaningless, and with that, the  $c_{33}$  of graphene is a meaningless concept.

260 Against these challenges, thickness and stiffness certainly exist in monolayer graphene,  
261 just as atomic radii exist (Sec. II A), and vary with pressure, which defines an atomic ra-  
262 dial stiffness. Electronic orbitals extend out of the plane of graphene nuclei and they resist  
263 compression. Such resistance (more accurately, compliance) consists of two parts. One is  
264 the Pauli exclusion compliance from the overlap of the  $\pi$ -orbitals of graphene and the outer  
265 orbitals of the medium that applies compression. It naturally depends on what that medium  
266 is and how it is stacked onto graphene. Moreover, the compliance has to be apportioned  
267 between the compliance of the graphene and the compliance of the medium. Surprisingly,  
268 even if the compressing medium is another graphene monolayer AB-stacked to it, the out-

269 of-plane stiffness is calculated to be, not that of graphite, but only about half of it.<sup>35</sup> This  
 270 softness is attributed to the squeezing of  $\pi$ -orbitals through the graphene plane in a bilayer  
 271 system, whereas such squeezing-through is prohibited in graphite (infinite number of lay-  
 272 ers) by symmetry.<sup>35</sup> In addition to the compliance of the Pauli exclusion for undeformed  
 273  $\pi$ -orbitals, the other contribution from the graphene to the total compliance is from the  
 274 deformation of the  $\pi$ -orbitals of the graphene. This could be estimated by calculating the  
 275 energy difference between relaxed and deformed  $\pi$ -electron distributions.

276 In the absence of a conventionally-defined elastic constant  $c_{33}$  based on internuclear dis-  
 277 tances, one approach to define the out-of-plane stiffness of graphene is to use a related  
 278 quantity that is itself unambiguously defined and measurable. The in-plane bonds stiffen  
 279 under compressive in-plane strain, which can be expressed as a 2D strain and converted to  
 280 a 2D stress by  $c_{ij}^{2D}$ . That has been measured by the increase in G-mode phonon frequency  
 281 under pressure.<sup>31,34,36-38</sup> In graphene as in graphite, the 2D in-plane stress can be applied by  
 282 hydrostatic pressure, and the 2D stress is then directly proportional to the thickness. Since  
 283 graphite and graphene are very soft out-of-plane, under hydrostatic pressure the thickness  
 284 decreases significantly (the  $\pi$ -orbitals being considerably compressed). That gives a large  
 285 reduction of in-plane force below the linear proportionality with pressure, and therefore a  
 286 substantially sublinear shift of the G-mode frequency with pressure.<sup>39</sup> An experiment adopt-  
 287 ing this approach had large experimental uncertainties, but within experimental uncertainty  
 288 first confirmed from the shift-rate of the G-mode that the thickness of graphene is not sig-  
 289 nificantly different from its thickness in graphite. Then the sublinearity of the shift-rate  
 290 could not distinguish the graphene  $c_{33} = 0 \pm 300$  GPa<sup>40</sup> from graphite ( $38.7 \pm 0.7$  GPa).<sup>20</sup>  
 291 Of course, there are also possible effects of the pressure medium on the graphene response;  
 292 these are discussed further in Sec. VI below.

## 293 D. Properties not related to graphite

294 In contrast to the foregoing, there are some properties of graphene that are quite distinct  
 295 from, or unrelated to, any properties of graphite. It is probably accurate to say that these  
 296 are all properties related to the freedom graphene has to displace in the  $z$ -direction, out  
 297 of plane, in ways that are unavailable to the layers in graphite. Briefly, these include the  
 298 theoretical instability of a 2D sheet, the negative thermal expansion in-plane of graphene,

299 and the stiffness in bending of monolayer graphene and of multilayer graphene.

## 300 **1. Acoustic phonons in graphene; their effect on the thermal expansion and** 301 **stability of graphene samples**

302 In this section, and the following sections III D 2 to III D 4, we will review the nature  
303 of the acoustic phonon modes in graphene. They are responsible for some key properties  
304 of graphene: The observation of a negative thermal expansion coefficient under certain  
305 conditions, lack of mechanical stability and – in consequence of this – static ripples in  
306 the graphene monolayer. These properties reflect, in a fundamental way, the 2D nature  
307 of graphene: The lack of restoring forces from adjacent atomic layers in the out-of-plane  
308 direction, and the density of states for a 2D material varying in proportion to  $k$  rather than  
309  $k^2$ .

310 To begin, we must briefly review the low-energy part of the phonon dispersion relation  
311 of graphene. The dispersion relation has been studied for decades prior to the discovery of  
312 graphene, as a simplified model for the phonons in graphite.<sup>41–43</sup> Initially these calculations  
313 were performed using traditional semi-classical “ball and spring” force constant models, and  
314 the results obtained nowadays using DFT calculations<sup>22</sup> are in reasonably good agreement  
315 with those obtained previously using “pencil-and-paper” methods. Agreement is also good  
316 with the experimental data obtained on graphite using electron energy loss spectroscopy,<sup>44</sup>  
317 inelastic neutron<sup>42</sup> and X-ray scattering.<sup>26</sup> Fig. 1 shows the low-energy part of the dispersion  
318 relation, calculated in Ref. 22 using DFT. In this section we shall regard low energy as up to  
319 50 meV since we are interested in the phonons which can be excited in significant number  
320 by thermal energy at  $T \leq 300$  K. (At 300 K,  $k_B T \approx 25$  meV).

## 322 **2. Mechanical stability of graphene**

323 As shown in Fig. 1, there are three acoustic phonon modes which can be excited at 300  
324 K. They are longitudinal (LA) and transverse (TA) polarization in-plane modes (both with  
325 linear dispersion relations in the low  $k$  limit) and a transverse polarization out-of-plane mode  
326 (ZA) with a quadratic dispersion relation in the low  $k$  limit ( $E \propto k^2$ ).<sup>22,43</sup> The softness of  
327 this mode relative to the LA and TA modes is believed to be partially due to the lack of

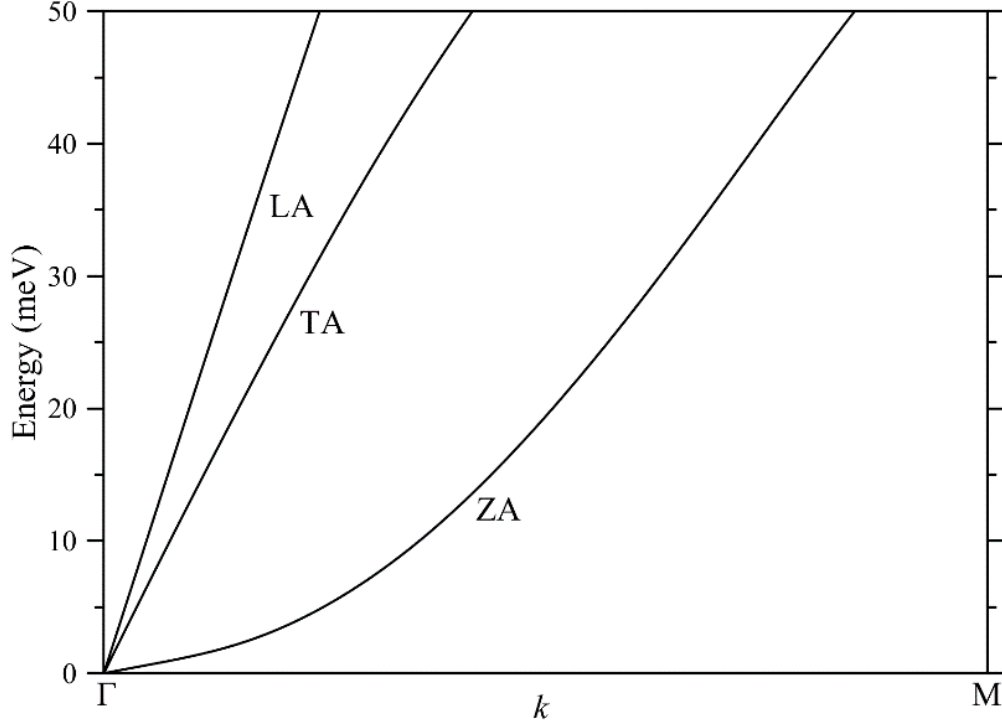


FIG. 1. Low-energy graphene phonon modes along the  $\Gamma$ -M direction in the first Brillouin zone, obtained in Ref. 22 using DFT. LA and TA modes are the longitudinal and transverse polarization in-plane modes and the ZA mode is the transverse polarization out-of-plane mode.

328 bending stiffness of graphene. However, the low bending stiffness is not necessary to explain  
 329 the quadratic dispersion relation. A transverse wave on a string (or sheet) with zero tension  
 330 but a bending stiffness  $D$  has  $\omega(k) = k^2(D/\rho)^{1/2}$ , so the quadratic dispersion relation is fully  
 331 consistent with the recently measured 1.7 eV bending stiffness of graphene.<sup>39,45</sup> The number  
 332 of phonons present at temperature  $T$  from branch  $i$  of the dispersion relation (hence with  
 333 energy  $E_i(k)$ ) is obtained by multiplying the Bose-Einstein distribution by the density of  
 334 states  $D(k)$  and integrating over all available  $k$  (Eq. 1). The lower limit  $k_{min}$  corresponds to  
 335 the longest wavelength mode that can exist on the graphene sheet. So  $k_{min} \approx 2\pi/L$  where  $L$   
 336 is the diameter of the graphene sheet. For macroscopic graphene samples therefore  $k_{min} \rightarrow 0$   
 337 is a reasonable approximation. Referring to Fig. 1 and the known graphene reciprocal lattice,  
 338 the path  $\Gamma \rightarrow M$  in reciprocal space covers a range of  $2.3 \times 10^9 \text{ m}^{-1}$ , whilst  $k_{min} \approx 10^5 \text{ m}^{-1}$   
 339 for a  $10 \mu\text{m}$  diameter graphene sheet.

340 The upper limit  $k_{max}$  should be set so as to integrate over all possible phonon modes, in  
 341 reality the upper limit of the integral is set by the Bose-Einstein distribution term dropping

342 to zero upon increasing  $k$ ,  $E$ .

$$N = \int_{k_{min}}^{k_{max}} \frac{1}{e^{\beta E(k)} - 1} D(k) dk \quad (1)$$

343 Here, we write  $\beta = 1/k_B T$  for convenience. The densities of states in 1D, 2D and 3D  
 344 systems, per unit area/volume, are given by:

$$\begin{aligned} D_{1D} &= \frac{1}{\pi} \\ D_{2D} &= \frac{k}{2\pi} \\ D_{3D} &= \frac{k^2}{2\pi^2} \end{aligned} \quad (2)$$

345 It has been shown that the value of the integral in Eq. 1 diverges to  $+\infty$  when a 2D  
 346 density of states function is utilized, combined with a quadratic dispersion relation.<sup>46</sup> This  
 347 is due to the value of the integrand diverging in the low- $k$  limit. The experimental obser-  
 348 vations that genuinely free-standing graphene sheets do not exist, and that all graphene  
 349 sheets are covered in static ripples (so, in at least one respect, not genuinely 2D) are at-  
 350 tributed to this divergence.<sup>46,47</sup> In addition, this divergence prevents the categorization of  
 351 free-standing graphene sheets as a metastable form of carbon in an equivalent manner to  
 352 diamond, nanotubes and fullerenes at ambient conditions.

353 In this section, we are going to explore the cause of this divergence in a little more  
 354 detail – can it be observed in systems with other dimensionalities, and with other dispersion  
 355 relations? In Table III we give the integrands that would be utilized in Eq. 1 for phonon  
 356 modes with quadratic and linear dispersion relations for 1D, 2D and 3D systems. Since we  
 357 seek only to evaluate which of these integrands diverge we have assumed a finite non-zero  
 358 temperature and omitted all constant terms, where we assume  $\beta$  is a finite constant since  
 359  $T > 0$  K. The integrands are evaluated in the low- $k$  limit (equivalent to assuming that  
 360 the sample is large enough to support phonons across essentially the entire Brillouin zone)  
 361 using first order expansions of the exponential term ( $e^x \approx 1 + x$ ), appropriate since we are  
 362 considering exclusively acoustic phonons for which  $E \rightarrow 0$  also in the low- $k$  limit.

364 Summarising the findings from Table III, we observe that in a 3D system divergence is not  
 365 observed for a linear or quadratic dispersion relation, for a 2D system divergence is observed  
 366 only with a quadratic dispersion relation, and for a 1D system divergence is observed with  
 367 either a linear or quadratic dispersion relation. These differences are due to the density of  
 368 states function being different in each case.

TABLE III. Integrands  $I_k^{(n)}$  to evaluate the number of phonons present at finite temperature for different dispersion relations, in systems with different dimensionality  $n$ . Constant terms and temperature dependence have been omitted.

	1D	2D	3D
$E \propto k$	$I_k^{(1)} = \frac{1}{e^k - 1}$ $\lim_{k \rightarrow 0} I_k^{(1)} = \frac{1}{k}$	$I_k^{(2)} = \frac{k}{e^k - 1}$ $\lim_{k \rightarrow 0} I_k^{(2)} = 1$	$I_k^{(3)} = \frac{k^2}{e^k - 1}$ $\lim_{k \rightarrow 0} I_k^{(3)} = k$
$E \propto k^2$	$I_{k^2}^{(1)} = \frac{1}{e^{k^2} - 1}$ $\lim_{k \rightarrow 0} I_{k^2}^{(1)} = \frac{1}{k^2}$	$I_{k^2}^{(2)} = \frac{k}{e^{k^2} - 1}$ $\lim_{k \rightarrow 0} I_{k^2}^{(2)} = \frac{1}{k}$	$I_{k^2}^{(3)} = \frac{k^2}{e^{k^2} - 1}$ $\lim_{k \rightarrow 0} I_{k^2}^{(3)} = 1$

369 To our knowledge, the consequences of this divergence have not been studied experimen-  
370 tally in 1D systems. Certainly its observation would require the existence of an extremely  
371 long system to ensure  $k_{min} \rightarrow 0$ , and for the system to be free-standing to allow these  
372 phonons to propagate. The nearest humankind has got to a genuinely 1D system is carbyne  
373 – in recent years carbyne chains up to 600 nm in length have been synthesized, satisfying  
374 the first condition.<sup>48</sup> But the requirement that they are enclosed inside a carbon nanotube  
375 probably prevents the second condition from being satisfied. Single-walled carbon nanotubes  
376 (SWCNTs) themselves are not strictly one-dimensional as far as the density of states func-  
377 tion is concerned. The quantization condition for the direction along the tube axis is the  
378 requirement for a standing wave with allowed wavelengths determined by the tube length,  
379 whilst the quantization condition for the direction tangential to the tube axis is for travel-  
380 ling waves with allowed wavelengths determined by the tube circumference. Thus, whilst  
381 the allowed quantum states are far more widely spaced in the tangential direction, the elec-  
382 tron and phonon wavevectors do still have 2 degrees of freedom, and the density of states  
383 function should follow a 2D form rather than the 1D form.

384 As far as graphene is concerned, the divergence in the number of out-of-plane phonons at  
385 finite temperature is believed to be responsible for the following experimental observations.  
386 Firstly, real monolayer graphene samples can only exist when provided with some mechanical  
387 support. Usually this is provided by a substrate. Samples may be described in the literature  
388 as “freestanding” when there is an aperture in the substrate or some similar arrangement, but  
389 there is always some mechanical support. Monolayer graphene samples may be suspended  
390 in a liquid such as water, in which the viscosity of the liquid provides adequate support.<sup>47,49</sup>

391 Secondly, real monolayer graphene samples are always rippled. These ripples are ex-  
392 pected from the findings of atomistic simulations.<sup>50</sup> They have been observed using electron  
393 diffraction<sup>51</sup> and also scanning tunnelling microscopy,<sup>52</sup> which has confirmed that they are  
394 static ripples, with  $\lambda \approx 5$  nm. The ripples become weaker for progressively thicker graphene  
395 samples as the thickness of the graphene sample itself provides the required rigidity. These  
396 ripples are a completely separate effect to the Brownian motion observed in graphene.<sup>53,54</sup>

397 The role of ripples in ensuring stability can be understood in terms of the restoring forces.  
398 The softness of the ZA mode shown in Fig. 1, compared to the in-plane modes, is because of  
399 the lack of restoring forces due to bond-stretching in the low amplitude limit, **and of those**  
400 **due to bending in the large-wavelength limit.** The curvature induced by the ripples ensures  
401 that there is some restoring force due to bond-stretching even in the low amplitude limit,  
402 making the mode — partially — analogous to the radial breathing mode in SWCNTs.<sup>55</sup>

### 403 ***3. Thermal expansion coefficient of graphene***

404 The existence of thermal expansion is perhaps the most intuitive example of the interplay  
405 between static and dynamic material properties. The lattice constant of a solid is considered  
406 the archetypal static property, yet at  $T > 0$  K it is altered (usually increased) by the presence  
407 of phonons; the archetypal dynamic property. The observation that the vast majority of  
408 materials expand upon heating is a consequence of the nature of the function  $V(r)$  giving  
409 the potential energy between two of the atoms comprising the solid as a function of their  
410 separation  $r$ . The Lennard-Jones potential is frequently utilized as a good approximation for  
411 covalently bonded solids even though it is only strictly correct for solids where the cohesion  
412 is due solely to vdW forces. In any case, the potential will always have three key features in  
413 common with the Lennard-Jones potential: (1) It will be attractive for moderate values of  
414  $r$ , with a minimum at  $r = r_0$ , the inter-atomic separation in the absence of phonon effects.  
415 (2) In the limit  $r \rightarrow \infty$ ,  $V \rightarrow 0$ . (3) In the limit  $r \rightarrow 0$ ,  $V \rightarrow +\infty$  to prevent atomic overlap.  
416 As a result of these features,  $V(r)$  is not symmetric about  $r = r_0$  and this asymmetry will,  
417 in the absence of other effects, favour thermal expansion rather than contraction.

418 This argument applies directly to any reasonably isotropic **and dense** 3D solid and, for  
419 that matter, a 2D solid existing in a 2D world (in which case out-of-plane phonon modes  
420 would not exist). However, graphene's position is as that of a 2D solid in a 3D world. In

421 this case, the excitation of an out-of-plane vibration does not cause any thermal expansion  
422 in the out-of-plane direction. However it can cause contraction in the in-plane direction as  
423 atoms are pulled inwards by the out-of-plane movement.

424 Thus, for graphene to exhibit a negative coefficient of thermal expansion coefficient  
425 (CTE), all that is necessary is for the contribution from the out-of-plane phonons to dom-  
426 inate over that from the in-plane phonons. We can see how this can be the case at low  
427 temperature from Fig. 1. The quantum states available for all phonons are equally spaced  
428 in  $k$ -space so, when phonons of all kinds (LA, TA, ZA) can be excited up to a certain energy,  
429 the out-of-plane ZA phonons dominate as they cover a wider area of  $k$ -space. The qualitative  
430 arguments proposed here are borne out by the findings of detailed theoretical calculations;<sup>22</sup>  
431 Graphene should indeed exhibit a negative CTE.

432 However, as shown earlier a graphene sheet which is genuinely freestanding, and therefore  
433 free to expand and contract, cannot exist. Experimental measurements of the CTE of  
434 graphene are therefore indirect and prone to large experimental, [theoretical and conceptual](#)  
435 [uncertainties](#).<sup>56</sup> Most commonly, it has been measured by varying temperature whilst the  
436 graphene is adhered to a substrate. The graphene is assumed to adhere perfectly to the  
437 substrate due to its extremely high surface area to volume ratio so, upon temperature  
438 increase the graphene would be forced to expand rather than contract and is therefore  
439 under significant tensile strain. The extent of this strain is usually calculated using Raman  
440 measurements on the G peak,<sup>57</sup> though grazing incidence X-ray diffraction has also been  
441 utilized.<sup>58</sup> Potential sources of uncertainty in such experiments include, but are not limited  
442 to:

- 443 • [The logic of such experiments is often not clearly presented. When a thin film fully](#)  
444 [adheres to a substrate, the difference in thermal expansions causes a stress in the film,](#)  
445 [not a strain. Stress cannot be measured by Raman. The CTE of the film should be](#)  
446 [directly measured by Raman of the thermal strain in a \*free-standing\* specimen of the](#)  
447 [film. Then to correct for the temperature effect on the phonon frequency, the phonon](#)  
448 [shift at known strain and ambient temperature is compared with the data from the](#)  
449 [film adhering to a substrate, at a known strain and elevated temperature. Given](#)  
450 [the difficulty of studying free-standing graphene, data from theoretical simulations is](#)  
451 [commonly used instead.](#)

- 452 • Commonly used substrates for graphene consist of layers of different materials with  
453 different TEC. It is not always clear which layer dominates, and to what extent the  
454 layers remain bonded.
- 455 • The out-of-plane phonons causing the negative TEC should be suppressed to some  
456 extent by the presence of the substrate. It is thus not clear how applicable findings  
457 regarding graphene on a substrate are to free-standing graphene.
- 458 • We assume a value for the Grüneisen parameter (for the phonon responsible for the G  
459 peak) when the strain is calculated from the G peak Raman measurement.
- 460 • Graphene does not always adhere perfectly to the substrate.

461 Notwithstanding these problems, the experimental evidence is consistent with graphene  
462 having a negative TEC at temperatures up to at least 500 K.<sup>56</sup> (and references therein) This is  
463 also the case for the in-plane measurements on graphite. [Indeed, comparing reported values  
464 and uncertainties of the TEC for graphene and for graphite in-plane,<sup>22,59–61</sup> it is difficult to  
465 find any justification for considering them to be different.](#) The small or negative CTE is  
466 reflected in the contrasting characteristics of graphene grown by chemical vapour deposition  
467 (CVD) and epitaxial growth (EG). Both growth processes take place at high temperature,  
468 followed by the substrate contracting upon cooling. In the case of the CVD graphene, Raman  
469 measurements at ambient conditions indicate that the graphene has “relaxed” *i.e.* slipped  
470 over the substrate upon cooling to stay in equilibrium. However, Raman measurements  
471 made on the EG graphene at ambient conditions indicate that it has remained adhered to the  
472 substrate upon cooling after growth.<sup>62</sup> As a consequence it is under significant compressive  
473 strain; equivalent to several GPa pressure.<sup>56</sup>

474 As briefly mentioned above, 3D materials with a layered structure can also exhibit a  
475 negative thermal expansion coefficient along one axis or in one plane,<sup>63–65</sup> although the  
476 phonon modes that cause this will cause positive thermal expansion along some other axes.  
477 In graphite at 300 K for example, the in-plane thermal expansion coefficient is *ca.*  $-1.4 \times 10^{-6}$   
478  $\text{K}^{-1}$ , but the out-of-plane thermal expansion coefficient is *ca.*  $+25 \times 10^{-6} \text{K}^{-1}$ .<sup>22</sup>

#### 479 **4. Grüneisen parameters and elastic bands**

480 The negative thermal expansion coefficient resulting from the ZA mode — by definition  
481 — results in this mode having a negative Grüneisen parameter (Grüneisen parameters for  
482 all phonon modes in graphene are calculated throughout the first Brillouin zone in Ref. 22).  
483 In the Grüneisen approximation, the pressure and temperature dependence of the phonon  
484 mode can both be incorporated into the volume or lattice parameter dependence on pressure  
485 and temperature, linked by the Grüneisen parameter. For a 2D material such as graphene  
486 we can write, following the approach in Ref. 34:

$$\frac{\omega(P, T)}{\omega_0} = \left( \frac{\alpha(P, T)}{\alpha_0} \right)^{-2\gamma_{ZA}} \quad (3)$$

487 where  $\alpha(P, T)$  is the pressure and temperature-dependent lattice parameter, as projected  
488 into the basal plane of the graphene lattice. In this case if  $\gamma_{ZA} < 0$ ,  $\omega(P, T)$  will decrease  
489 under isothermal compressive strain and increase under isothermal tensile strain. Whilst  
490 highly unusual on a microscopic level, it is the behaviour we are used to observing in common  
491 macroscopic 1D systems in everyday life: When you stretch elastic bands, or guitar strings,  
492 or the shrouds and stays of a yacht, they twang at a higher frequency!

#### 493 **5. Bending stiffness**

494 In 3D systems, while the elastic constants discussed above are properties of a material, a  
495 bending stiffness is a property, not of a material, but of a structure, i.e., related to geometry.  
496 It is however defined in a similar way. The elastic constants are the second derivatives of the  
497 potential energy with respect to deformation (strain). Graphene has the additional degree  
498 of freedom, of bending to a curvature  $\kappa$  ( $= 1/R$  where  $R$  is the radius of curvature). This  
499 additional degree of freedom, bending, and hence a bending stiffness, has no analogue in  
500 graphite. To account for the bending stiffness,  $D$ , defined by the energy of curvature  $\kappa$ ,

$$U = 1/2 D \kappa^2 \quad (4)$$

501 there is a large literature in which an effective Young's modulus  $Y_{eff}$  and an effective thick-  
502 ness  $h_{eff}$  are introduced such that both the in-plane elastic moduli and the bending stiffness

503 can be expressed:

$$\begin{aligned} Yh &= Y_{eff}h_{eff} \\ D &= \frac{Y_{eff}h_{eff}^3}{12} \text{ or } \frac{Y_{eff}}{1-\nu^2} \frac{h_{eff}^3}{12} \end{aligned} \quad (5)$$

504 where in the second expression for  $D$  it is the plane-strain modulus that is used, as is correct  
505 for a plate made of an isotropic material.

506 The model of Eq. 5 has had remarkable success in capturing the behaviour of graphene  
507 and nanotubes, particularly in contexts where beam, plate and shell theory are used to un-  
508 derstand buckling behaviour under load.<sup>6</sup> Due to the uncertainties of a definition of graphene  
509 thickness, on the other hand, it has led to claims that nanotubes have “an extremely large  
510 Young’s modulus”,<sup>66</sup> for example the value of 5.5 TPa given by Yakobson *et al.* for  $Y_{eff}$ .<sup>6</sup>  
511 Similarly, astonishment has been expressed at the small values of  $h_{eff}$ , as low as 0.066 nm,  
512 “ultrathin compared with the C-C bond length 0.142 nm”.<sup>66</sup> The very wide range of values  
513 reported for these parameters<sup>67</sup> has been described as a paradox (Yakobson’s paradox).<sup>68,69</sup>  
514 As some authors have recognised, there is no paradox,<sup>70–72</sup> but much of the literature fails  
515 to distinguish  $h$  and  $Y$  from  $h_{eff}$  and  $Y_{eff}$ . The wide ranges of values express only the im-  
516 precision in the determination of  $D$  by different methods. The unphysical values found for  
517  $Y_{eff}$  and  $h_{eff}$  simply reflected the unphysical nature of these parameters, which correspond  
518 to nothing in the real world but are simply convenient ways of representing  $D$  in structural  
519 engineering computational packages that do not permit  $D$  to be entered independently of  $Y$   
520 and  $h$  (if any such packages exist, which is doubtful, as engineers routinely analyse structures  
521 of this sort, such as honeycomb-filled or rib-reinforced plates).

522 Reported experimental methods of measuring  $D$  range from the collapse pressure  $P_C$  of  
523 nanotubes under high pressure ( $1.7 \pm 0.2$  eV),<sup>45</sup> to the taper angle of a strip torn from an ad-  
524 hesive substrate ( $2.1 \pm 0.1$  eV).<sup>73</sup> A value of 2 eV was estimated from the phonon dispersion  
525 measured by high resolution electron energy loss spectroscopy (HREELS), on Pt (111) sup-  
526 ported graphene.<sup>74</sup> Other measurements reported values as high as  $10^3 - 10^4$  eV for rippled  
527 monolayer<sup>75</sup> and  $35.5_{-15.0}^{+20.0}$  eV for bilayer.<sup>76</sup> Torres-Dias *et al.* found that for nanotubes of  
528 small diameters, the normalised collapse pressure  $P_C R^3 = 3D$  dropped substantially below  
529 the theoretical value, which could be due to the softened bending potentials at large bending  
530 angles, or an effect of atomicity.<sup>45</sup> Carter *et al.*<sup>77</sup> study the Euler buckling load for a straight  
531 pillar. When the compliance of a continuous pillar is concentrated at a few points (atoms,

532 or angular springs) between rigid portions, the buckling load is substantially reduced. The  
 533 effect is hard to explain, but is readily derived from the TA phonon dispersion curve of the  
 534 infinite linear chain, which predicts a decrease of the phase velocity of the TA mode as the  
 535 wavelength decreases. In any case, this observation requires that the bending stiffness of  
 536 flat graphene is obtained, as in Ref. 45, from the extrapolation of normalised experimental  
 537 collapse pressures to  $R^{-3} = 0$ .<sup>45,77</sup>

## 538 6. Folding

539 When a sheet of graphene is folded over onto itself, it adheres due to the vdW interaction.  
 540 The radius of the fold is determined by the strength of the vdW attraction and by the value of  
 541  $D$ , and is of the order of the radius of  $C_{60}$ . An example is found in large-diameter SWCNTs,  
 542 which are collapsed already at ambient pressure into the shape called “dogbone” or “peanut”.  
 543 This presents a cavity of  $\approx 0.6$  nm in diameter at the edge.<sup>78,79</sup> This small diameter reflects  
 544 the very small value of the bending stiffness of monolayer graphene, in the range of 1 eV,  
 545 but an accurate evaluation depends on knowing the strength of the vdW adhesion holding  
 546 the fold folded. The atomic nature of the sheet plays a role, and folding is angle dependent  
 547 as reported in the study of Zhang *et al.*<sup>80</sup> They reported that graphene sheet tends to fold  
 548 along armchair ( $0^\circ$  folding angle) and zigzag directions ( $30^\circ$  folding angle). Consequently  
 549 the spontaneous collapse of large nanotubes must depend on the chirality, which imposes  
 550 the folding angle. The most unfavorable direction has the folding angle of  $10^\circ$ . Under very  
 551 high temperature annealing (2000 °C) the unfavourable angle of folded graphene generates  
 552 defects such as pentagons, relaxing the stress and leading to an irregular edge composed of  
 553 zigzag and armchair directions.<sup>81</sup>

554 For bilayer and multilayer graphene with  $n$  layers ( $n > 1$ ), the angle dependance disap-  
 555 pears and this cavity size is governed by the number of layers,  $n$ . The length of the folding  
 556 (shape of a pear) is well described by:<sup>82</sup>

$$L(n) = \pi \sqrt{\frac{D}{\gamma}} = \left[ \pi \sqrt{\frac{Y}{\gamma} \frac{d_{vdW}^3}{12}} \right] n^{\frac{3}{2}} \quad (6)$$

557 where  $D$  is the bending stiffness of the multilayer per unit length,  $d_{vdW}$  is the equilibrium  
 558 distance between two graphene layers,  $Y$  is the Young’s modulus,  $\gamma$  surface adhesion energy  
 559 per unit length around  $260 \text{ mJ}\cdot\text{m}^{-2}$  (42.2 meV/atom).<sup>82</sup> In Chen *et al.*,<sup>83</sup> the bending stiffness

560  $D_n(\text{eV})$  is well fitted by  $6.7 \times (nh)^2$  with  $n$  between 2 to 6. These results are completely  
 561 different even if for both relations, the bending stiffness of multilayer graphene is higher  
 562 than a simple summation of the bending stiffness of each individual layer. The mechanical  
 563 properties of bilayer and multilayer graphene depend critically on the issue of slipping or  
 564 binding between layers. If layers slip freely, then the bending stiffness of  $n$ -layer graphene  
 565 will be  $nD_1$  which is not the case from simulation. On the other hand, if slipping does  
 566 not occur, the bending stiffness of a bilayer,  $D_2$ , will be largely unrelated to  $D_1$  as it then  
 567 derives directly from the in-plane stiffness (plus  $nD_1$ ).<sup>84</sup> Neglecting  $D_1$  for multilayers, we  
 568 have  $D_2 = 2(h/2)^2 c_{11}^{2D}$ ,  $D_3 = 2h^2 c_{11}^{2D}$  and  $D_4 = 2[(3h/2)^2 + (h/2)^2] c_{11}^{2D}$  and for large  $n$ , we  
 569 recover the usual relation:  $D_n = \frac{c_{33}}{1-\nu^2} \frac{(nh)^3}{12}$ . The numerical values  $D_1 = 0.7$ ,  $D_2 = 131$  and  
 570  $D_4 = 1308$  eV are to be compared to the value of  $D_1 = 2.1$ ,  $D_2 = 130$  and  $D_4 = 1199$  eV  
 571 reported by Sen *et al.*<sup>73</sup>

## 572 7. *Shearing, sliding and friction between graphene layers*

573 In multilayer graphene, as mentioned in the previous Section, whether shearing or sliding  
 574 occurs between layers determines the bending stiffness of the multilayer. In addition, a  
 575 Raman shear mode is observed at low wavenumbers, between  $31 \text{ cm}^{-1}$  (bilayer) to  $43 \text{ cm}^{-1}$   
 576 (bulk).<sup>85</sup> Considering a linear chain model, it is possible to define an interlayer coupling  
 577 stiffness,  $\alpha = 12.8 \times 10^{18} \text{ N}\cdot\text{m}^{-3}$ . The same value fits the Raman from bilayer through to  
 578 graphite. It is a microscopic measure of the shear modulus,  $\alpha d_0 = c_{44} = 4.3 \text{ GPa}$ , close to  
 579 the value of Table I. It corresponds to a spring constant  $k = 0.419 \text{ N}\cdot\text{m}^{-1}$  for an unit cell.  
 580 The existence of this mode shows the corrugation of the graphene surface at the atomic  
 581 scale. It is also possible by friction to characterize atomically the surface. For a monolayer,  
 582 the presence of ripples can increase the friction by 40% compared to bulk graphite where  
 583 the layers are flat.<sup>86</sup> The friction results are well reproduced by calculation.<sup>87</sup> Finally, the  
 584 sliding, corresponding to electrostatic interactions and dispersive forces, and its dependence  
 585 on atomic direction has been calculated.<sup>87</sup> During the sliding, the interlayer distance changes  
 586 by  $0.04 \text{ \AA}$  and the force is found to be in the range of  $1.92 \text{ pN/atom}$  considering no relaxation  
 587 of the atoms, which is close to the experimental value of  $2.11 \text{ pN/atom}$ . These values are  
 588 typical of flat 2D systems (h-BN).<sup>87</sup>

## 589 IV. MEASURING GRAPHENE MECHANICAL PROPERTIES

590 The nanoscale thickness of monolayer graphene makes the accurate measurement of its  
 591 mechanical properties a challenging task. A number of techniques have been proposed in  
 592 the literature<sup>88-90</sup> to measure the mechanical properties of graphene membranes. Some of  
 593 the most important ones are described here.

### 594 A. Atomic force microscopy

595 The use of AFM in the study of the mechanical properties of graphene usually involves  
 596 suspension of monolayer graphene over a substrate that has been previously patterned with  
 597 holes and then applying a local force to the surface of graphene with high precision. In  
 598 this way, the in-plane mechanical properties can be obtained. The work of Lee *et al.*<sup>25</sup>  
 599 was the first to measure the elastic modulus and fracture strength of graphene by using an  
 600 AFM tip to indent graphene that was suspended over circular wells. Force-displacement  
 601 (load-indentation) curves were obtained by indenting the membranes under constant speed.  
 602 The applied force can then be calculated. However, the exact theory is far from simple<sup>91</sup>  
 603 and many authors have used equations that appear to be over-simplified. The following  
 604 equation, for example, has been frequently used,<sup>25</sup>

$$F = \sigma_0^{2D}(\pi R)\left(\frac{\delta}{R}\right) + E^{2D}(q^3 R)\left(\frac{\delta}{R}\right)^3 \quad (7)$$

605 where  $R$  is the radius of the circular well,  $\delta$  is the indentation depth,  $\sigma_0^{2D}$  is the pre-tension  
 606 and  $E^{2D}$  is the 2D Young's modulus, and  $q$  can be expressed as  $1/(1.05 - 0.15\nu - 0.16\nu^2)$ ,  
 607 where  $\nu$  is the Poisson's ratio of graphene.<sup>25</sup> Given the uncertainties in the other parameters,  
 608 one may question the spurious precision implied by the inclusion of the factor  $q$ , which ranges  
 609 only from 0.95 to 1.05 over the whole range of possible values,  $0 < \nu < 0.5$ , and has the value  
 610 of 0.98 for the graphene value of  $\nu = 0.16$ . It is implausible that the contribution of the  
 611 pre-tension to the force, for a given depth, is independent of the radius of the well. Fitting  
 612 the data, values of the modulus and fracture strength of graphene are obtained. Similarly,  
 613 the breaking strength can be calculated from:

$$\sigma_{max} = \left[ \frac{F_{max} E^{2D}}{4\pi R_{tip}^2} \right]^2 \quad (8)$$

614 where  $R_{tip}$  is the radius of the AFM tip and  $F_{max}$  is the force at which the membrane breaks.

615 A variation of the AFM nanoindentation method where graphene suspended over a cir-  
 616 cular hole, is the so-called beam bending method, where the 2D membrane is now in the  
 617 form of a beam (or a stripe) and is suspended over a trough in the substrate. In this case  
 618 the load-deformation relationship is:<sup>92</sup>

$$F = \frac{Ew\pi^4}{6} \left(\frac{t}{L}\right)^3 \delta + \frac{\sigma_0 w \pi^2}{2} \left(\frac{t}{L}\right) \delta + \frac{Ew\pi^4}{8} \left(\frac{t}{L^3}\right) \delta^3 \quad (9)$$

619 where  $w$ ,  $t$ , and  $L$  are the width, thickness and length of the beam,  $\sigma_0$  is the intrinsic stress,  
 620  $\delta$  is the beam deflection,  $F$  is the load applied in the beam centre and  $E$  is the Young's  
 621 modulus.

622 Although the majority of the AFM-based results in the literature agree (within large  
 623 experimental uncertainties) with values estimated from the bulk materials and with theo-  
 624 retical calculations, it has been debated whether AFM nanoindentation can measure the  
 625 mechanical properties of macroscopic 2D membranes in a meaningful way.<sup>93</sup> The AFM tip  
 626 focuses on very small areas where the probability of defects is low. Intrinsic defects, rip-  
 627 ples and crumples that are known to reduce the inherent properties of a “perfect” material  
 628 are very common in 2D materials, yet are sometimes ignored or overlooked. Parameters  
 629 that introduce uncertainties into the interpretation of data include the initial stress of the  
 630 2D membranes, the position of the indenter (which needs to be in the exact centre of the  
 631 membrane) and the indenter radius. Nevertheless, AFM nanoindentation is one of the most  
 632 popular experimental methods to measure the mechanical properties of 2D membranes and  
 633 has been used for a number of 2D materials.

634 Lee *et al.*<sup>25</sup> found the Young's modulus of monolayer graphene to be  $E_{2D} = 340 \pm 50$  N  
 635  $\text{m}^{-1}$ , corresponding to  $E = 1.0 \pm 0.1$  TPa for a thickness of 3.35 Å. However, not all graphene  
 636 samples are flat. Nicholl *et al.*<sup>94</sup> and Ruiz-Vargas *et al.*<sup>95</sup> focused on crumpled and wrinkled  
 637 graphene prepared by CVD and found that the stiffness obtained by AFM nanoindentation  
 638 was reduced, compared to monocrystalline graphene.

639 A different, very useful application of AFM nanoindentation was reported by Cui *et al.*<sup>96</sup>  
 640 They performed a fatigue study using a combination of static and cyclic mechanical loading  
 641 of a suspended 2D film (Fig. 2 (a)). Monolayer and few-layer graphene survived more than  
 642 109 loading cycles at a mean stress of 71 GPa and a stress range of 5.6 GPa; that is higher  
 643 than any material reported so far.

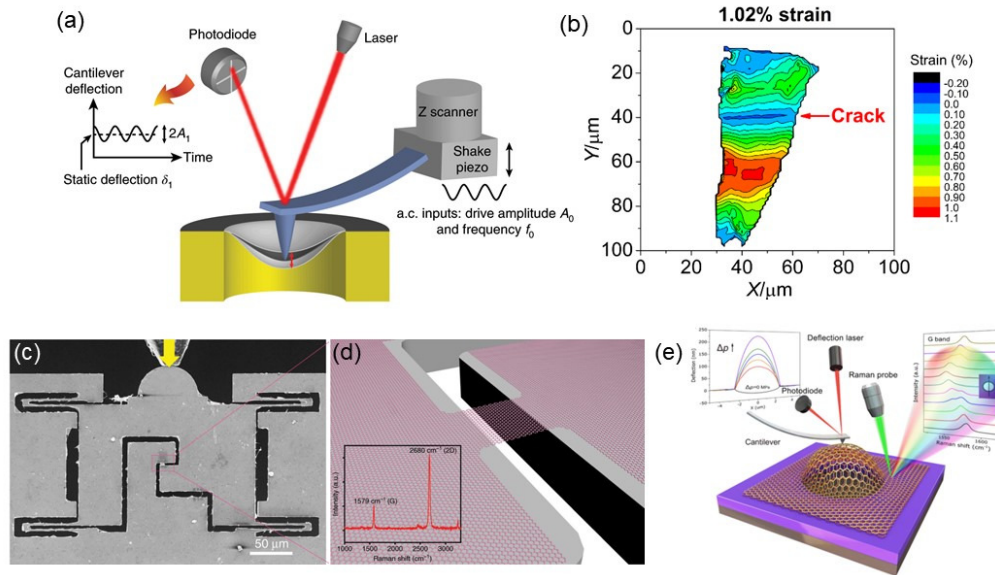


FIG. 2. (a) Schematic of the AFM fatigue testing set-up. Reproduced with permission from Nature Materials **19**, 405 (2020).<sup>96</sup> Copyright (2020) Springer Nature. (b) Strain contour map of a monolayer graphene flaked under 1.02% strain, where the strain distribution can be identified. The presence of a crack running through the upper part of the flake can be realised by the blue 0% strain line. Reproduced from Ref. [97](#) with permission from The Royal Society of Chemistry. (c) A deposited graphene sample in the centre of a push-to-pull micromechanical device, actuated by an external pico-indenter. The yellow arrow indicates the indentation direction during a tensile testing process. (d) Illustration of the graphene sample suspended between the device gap. (c) and (d) are reproduced from K. Cao, S. Feng, Y. Han, L. Gao, T. Hue Ly, Z. Xu, and Y. Lu, Nature Communications **11**, 284, 2020,<sup>98</sup> licensed under a Creative Commons Attribution (CC BY) license. (e) Schematic diagram of the bilayer graphene balloon. The left inset shows the increasing pressure on a graphene bubble, while the right inset shows the Raman G band of graphene across the balloon (line scan). Reproduced with permission from Phys. Rev. Lett. **119**, 036101 (2017).<sup>99</sup> Copyright (2017) The American Physical Society.

## 644 B. Raman spectroscopy

645 Raman spectroscopy has been used extensively for the study of the mechanical properties  
646 of carbon-based materials as a result of their strong resonant Raman scattering. The well-  
647 defined characteristic Raman peaks enable the observation of a number of very interesting  
648 phenomena and properties under uniaxial or biaxial strain.

649 For uniaxial strain, these experiments involve the deposition of monolayer or multilayer  
650 graphene flexible onto a polymeric substrate, which is subsequently strained by 2-, 3- or 4-  
651 point bending under a Raman spectrometer. The application of strain leads to an elongation  
652 of the C-C bonds and the lattice deformation is clearly and accurately evidenced by down-  
653 shifts of the Raman peaks. Mohiuddin *et al.*<sup>33</sup> first studied the deformation of monolayer  
654 graphene deposited onto a flexible substrate under uniaxial tensile strain and found that the  
655 shift of the 2D-mode is about  $-60 \pm 5 \text{ cm}^{-1}/\%$  strain. This downshift corresponds to the  
656 material having an elastic modulus in the order of 1 TPa and was subsequently confirmed  
657 by a number of research groups.<sup>1,97,100,101</sup> The G band is split by the uniaxial strain into  
658  $G^+$  and  $G^-$  peaks. The shift of the  $G^+$  band was  $-10.8 \text{ cm}^{-1}/\%$  strain while the shift of  
659 the  $G^-$  band was  $-31.7 \text{ cm}^{-1}/\%$  strain. The frequency of the G-mode is related to the C-C  
660 bond stiffness, though it contains non-negligible contribution from up to the fifth nearest  
661 neighbour (more details in Sec. VIII).<sup>26</sup> It is nevertheless reasonable to consider that its shift  
662 with strain has contribution only from the nearest neighbour, and is therefore determined  
663 by the anharmonicity of the C-C bond. The physical meaning of the shift of the 2D-mode is  
664 less clear as it is related to the evolution of the LO/TO phonon dispersion under strain.<sup>102</sup>

665 The strength of monolayer graphene can be also studied by *in situ* Raman mapping. Zhao  
666 *et al.*<sup>97</sup> prepared monolayer graphene by mechanical exfoliation, deposited the samples onto  
667 polymer substrates and performed *in situ* Raman mapping at different strain levels to obtain  
668 the strain distributions over the graphene flakes. Strain contour maps showed significant  
669 events such as strain build up, edge effects and cracks which developed with increasing strain  
670 (Fig. 2 (b)). Two main mechanisms of failure were observed: flake fracture, and failure  
671 of the graphene/polymer interface. Low strengths were observed for these macroscopic  
672 monolayer samples, only 10 – 15 GPa, an order of magnitude lower than the value of 130  
673 GPa that was reported by Lee *et al.*<sup>25</sup> Simulations suggest that this was due to the presence  
674 of defects.<sup>97</sup> Under large deformation, Raman observations also suggest a manifestation of

675 large nanometer-scale strain inhomogeneity within the laser spot size.<sup>103,104</sup>

676 In multilayer graphene, Gong *et al.*<sup>105</sup> studied the effect of the layer number on the  
677 downshift of the 2D band and found that monolayer and bilayer graphene displayed almost  
678 the same redshift rate. On the other hand, with further increasing layer number, the shift  
679 rate decreases significantly. The 2D Raman profile was fitted by a single Lorentzian, although  
680 a broadened 2D profile is expected with increasing number of layers as it contains more  
681 components,<sup>102</sup> and the decrease of the ‘average’ shift rate was interpreted as showing some  
682 slippage between the layers, *i.e.* reduced internal stress transfer. However, these spectra  
683 were recorded at the centres of the flakes. Similarly to shear lag, slippage between layers or  
684 between the lowest layer and the substrate should reduce the strain at the edge of the flake  
685 first and propagate inwards as the strain is increased (Fig. 2 (b)). More detailed studies  
686 would be desirable.

687 For biaxial strain, blister testing as described in Sec. IV D below is appropriate. G-mode  
688 shifts as large as  $-80 \text{ cm}^{-1}$  are obtained and the deduced Gruneisen parameter of  $1.8 \pm 10\%$   
689 is compatible with biaxial strain.<sup>106</sup> The calculated slope (with some approximation on  $Y$ ,  $D$   
690 and  $d_{vdW}$ )  $\Delta\omega_G/\epsilon = -57 \text{ cm}^{-1}/\%$  can be compared with later similar studies. Shin *et al.*<sup>103</sup>  
691 achieved biaxial reversible strain up to  $\approx 2\%$ . Using the same approximations, they found  
692  $\Delta\omega_G/\epsilon = -62 \text{ cm}^{-1}/\%$ . With large biaxial strain, the linewidth of the G-mode increases.

693 Interlayer modes, the layer breathing mode and shear mode, are convenient measures of  
694 adhesion and shear strength between graphene layers. A linear chain model describes the  
695 frequency of the shear mode, and its change with number of graphene layers very well, as  
696 discussed in Sec. III D 7. The model applies to the layer breathing mode too.<sup>107</sup> The layer  
697 breathing mode becomes Raman-active, when graphene layers are twisted from AB stack-  
698 ing. Its intensity is usually very weak, and requires resonance condition to be observable.  
699 Resonance Raman spectroscopy is particularly useful to study graphene and CNTs samples,  
700 where the resonance condition is that the energy of the in-coming or out-going laser matches  
701 the gap between van Hove singularities in these low-dimensional samples.<sup>108,109</sup>

### 702 C. *In situ* tensile tests

703 For *in-situ* tensile tests, nanomechanical testing devices are usually introduced within a  
704 scanning electron microscope (SEM) or transmission electron microscope (TEM) and the

705 deformation of the graphene is followed in the images. To study its fracture toughness, Zhang  
706 *et al.*<sup>110</sup> suspended nanocrystalline graphene over the jaws (gap) of a micromechanical device  
707 driven by a nanoindenter, within an SEM chamber. This imposed uniaxial tension on the  
708 graphene. Brittle fracture was observed when a central crack had been machined by FIB  
709 in the graphene samples prior to testing. The fracture toughness of graphene (important  
710 for engineering applications) was found to be  $K_c = 4.0 \pm 0.6$  MPa, while the critical strain  
711 energy release rate was  $G_c = 16 \pm 5$  J·m<sup>-2</sup> (where we estimate the uncertainty on  $G_c$  from  
712 their data). Cao *et al.*<sup>98</sup> reported *in situ* tensile tests within an SEM chamber and measured  
713 the elastic properties and stretchability of monolayer CVD graphene (Fig. 2 (c,d)). The  
714 Young's modulus was  $\sim 1$  TPa, while the tensile strength was around 50 – 60 GPa, when  
715 the elongation of the sample was  $\sim 6\%$ . Once again the actual strength of macroscopic  
716 graphene samples is significantly lower than the value of 130 GPa reported by Lee *et al.*<sup>25</sup> in  
717 AFM nanoindentation. Brittle fracture initiated from the edges of the samples, suggesting  
718 that control of the edge states and edge effects could lead to greater strength.

719 *In situ* TEM can offer useful information on cracks and defects in graphene. For example,  
720 Fujihara *et al.*<sup>111</sup> observed that crack propagation takes place along a specific crystallographic  
721 direction, in order to create zigzag edges. Kim *et al.*<sup>112</sup> showed that the presence of grain  
722 boundaries influences crack growth. When the stress is normal to the grain boundaries,  
723 the crack can follow the boundary; however, if the crack is initiated away from the grain  
724 boundaries and at some random orientation with respect to it (with the strain direction not  
725 normal to the grain boundary), the stiffness the tear experiences is more or less unaffected  
726 by the grain boundary and the crack will pass through the grain boundary, switching to the  
727 most favourable direction in the next grain.

#### 728 D. Pressurized blister method

729 The use of the pressurized blister (bulge, bubble, or balloon) method can provide infor-  
730 mation on the mechanical properties of 2D membranes and the interfacial adhesion between  
731 the substrate and the membrane. For these experiments, graphene is again suspended on  
732 top of a hole, or microcavity, in the substrate. The vdW forces between the substrate and  
733 the membrane hold the sample in place. Gas is fed in the hole thus pressurising the mem-  
734 brane. This leads to a spherical blister with a radius  $R$ . AFM is used to measure the blister

735 (compare Raman methods in Sec. IV B). The relation between its height,  $\delta$ , and the pressure  
736 difference inside and out,  $\Delta p$ , is,<sup>113</sup>

$$\Delta p = K(\nu)(Ed\delta^3)/R^4 \quad (10)$$

737 where  $E$  is the Young's modulus, and  $d$  is the graphene thickness.  $K(\nu)$  is a coefficient  
738 depending on Poisson's ratio only and is very close to 3. Thus the elastic modulus can be  
739 calculated from the measured AFM deflections.

740 The group of Bunch<sup>114</sup> first measured the adhesion of graphene on a silicon oxide substrate  
741 in this way. The adhesion strength is revealed by the pressure at which the blister diameter  
742 begins to exceed the hole diameter, i.e. when the graphene begins to peel away from the  
743 substrate. The relationship is given by Bodetti *et al* as Eq. 14 of their paper.<sup>115</sup> They obtain  
744 adhesion energies of  $0.45 \pm 0.02$  J/m<sup>2</sup> for monolayer graphene and  $0.31 \pm 0.03$  J/m<sup>2</sup> for  
745 few-layer graphene (2 – 5 sheets). With its high flexibility, graphene, especially monolayer  
746 graphene, is able to conform to the topography of very smooth surfaces, thus leading to high  
747 values of adhesion energy. However, much lower values may be observed, as adhesion between  
748 a graphene sheet and a substrate (or surface) is highly dependent on the surface conditions  
749 such as moisture, roughness, chemical reactivity and others and a considerable spread on  
750 the adhesion energies has been reported in the literature (see Ref. 2 and references therein).  
751 Similarly, weakening of the adhesion in turbostratic graphite compared with Bernal graphite  
752 is expected.<sup>5,116</sup> In a more recent report, Wang *et al.*<sup>99</sup> measured the interlayer shear stress  
753 of bilayer graphene by monitoring the strains in the graphene next to the blister but not  
754 lifted off the substrate (Figure 2 (e)). Here strain develops as a consequence of sliding. Their  
755 data provided evidence of both the lower monolayer sliding on the substrate, and the upper  
756 layer sliding on the lower layer. Analysis of the data gave the interfacial shear stress of  
757 monolayer graphene on SiO<sub>2</sub> as 1.64 MPa. This was much higher than the interlayer shear  
758 stress of bilayer graphene, 40 kPa (1.04 fN/atom). The implication is that the graphene-  
759 SiO<sub>2</sub> vdW bonding is much stronger than the weak dispersion vdW bonding that holds the  
760 two graphene sheets together.

## 761 E. Inelastic X-ray scattering

762 As discussed in Section III, some key elastic moduli of graphene come directly from the  
763 experimental values for graphite, measured by inelastic x-ray scattering (IXS). This measures

764 the acoustic phonon branches of graphite.<sup>20</sup> The initial slope of these branches along high-  
765 symmetry directions gives the sound velocity, and therefore the moduli by Christoffel's  
766 equation.<sup>117</sup> IXS is less sensitive to structural defects than ultrasonic methods and it does  
767 not have the difficulties in sample size and energy transfer limitations that inelastic neutron  
768 scattering suffers.<sup>20</sup> Experimentally IXS employed to measure graphite is not suitable for  
769 measurements on graphene due to the small sample volume. The alternative approaches  
770 to measure the in-plane elastic moduli of graphene are introduced above, and the results  
771 largely depend on interactions of graphene with its surroundings (substrates and/or [pressure](#)  
772 [transmitting media](#), PTM). Details will be discussed in Section V.

## 773 F. Density functional theory

774 This section particularly addresses properties that are anisotropic in-plane, which have  
775 been calculated but not confirmed by experiments. Whereas it is extremely difficult to  
776 do any mechanical testing on free-standing graphene, the in-plane graphene mechanical  
777 properties calculated by DFT are obtained naturally freestanding, and in vacuum. It is  
778 commonly considered that the calculated in-plane elastic constants are accurate (and in-  
779 deed they are close to the well-established experimental results on graphite)<sup>22</sup> and they  
780 are often used to parameterise various empirical models and evaluate the validity of classic  
781 simulations.<sup>22,118–121</sup> Strain is the input in a computational model and the resulting energy  
782 and stress are calculated. The ease with which the positions of the atoms can be specified  
783 enables the investigation of a number of anisotropic in-plane properties that result from  
784 strain along specific directions (armchair or zigzag).

785 The undeformed hexagonal lattice is isotropic. While in-plane uniaxial strain breaks  
786 the symmetry, the isotropy remains in the sense that most properties vary with the  
787 strain along most directions very similarly, except two specific directions.<sup>122,123</sup> We present  
788 clear anisotropic response of four properties to uniaxial strain along zigzag or armchair  
789 directions.<sup>121,124,125</sup> Fig. 3 (a) presents that the in-plane Poisson's ratio (corresponding to  
790 the elastic modulus  $c_{12}$ ) shifts differently with uniaxial strain along armchair or zigzag  
791 direction, and the stiffness (corresponding to  $c_{11}$ ) becomes different after 15% strain along  
792 armchair or zigzag direction.<sup>124</sup> Fig. 3 (b) shows that stress-strain curves of the shear de-  
793 formation (relevant to  $c_{66}$ ) along these two directions are different.<sup>121</sup> The ultimate stress of

794 graphene along these two directions is also calculated to be different by about 20%.<sup>120</sup> Zhou  
795 *et al.* plotted the electron density of graphene at zero, biaxial and uniaxial stress, as shown  
796 in Fig. 4.<sup>125</sup> In Fig. 4 (c), the high electron density area (red area) at uniaxial stress along  
797 zigzag direction attracts the nuclei at corners more than the central areas of those stretch  
798 bonds attracting those corresponding nuclei. That extra attraction stiffens the three-atom  
799 bending force constant labeled by  $k_{angle}$ , which supports the uniaxial stress. Differently,  
800 along uniaxial stress along the armchair direction, the supporting bending force constant  
801 (labeled as  $k_{angle}$  in Fig. 4 (d)) is stiffened by two high electron density areas (two red areas  
802 on the right). This was proposed as a possible interpretation for the anisotropy in ultimate  
803 strength<sup>125</sup> and could be relevant to other anisotropic properties.

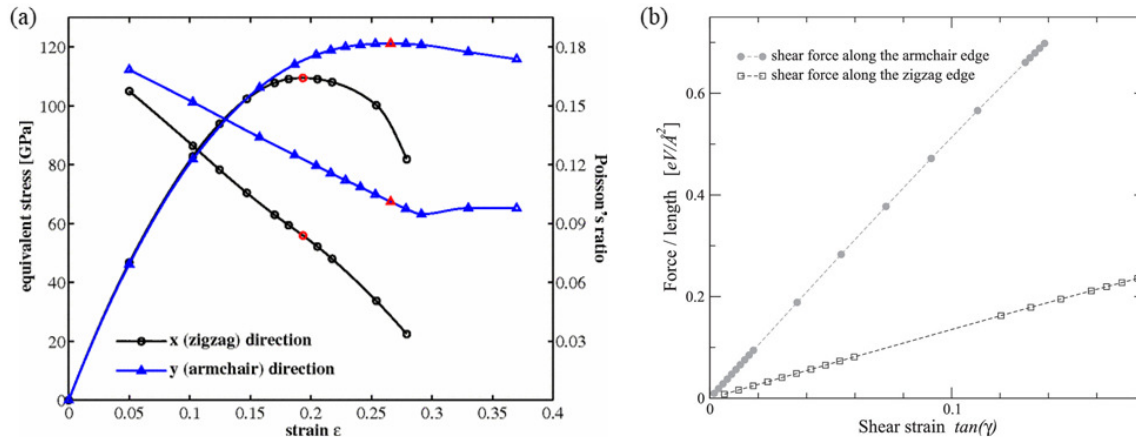


FIG. 3. (a) “The curves connected to the origin are the equivalent tensile stress ( $d_0=3.34 \text{ \AA}$ ) versus uniaxial strain in the  $x$  and  $y$  directions, respectively. The lines with initially negative slopes (scale labels to the right) are the finite-deformation Poisson’s ratios as functions of the uniaxial strain in the  $x$  and  $y$  directions, respectively. The red circles and triangles indicate the condition where peak stress could be attained for zigzag and armchair nanotubes, respectively.” Reproduced with permission from Phys. Rev. B **76**, 064120 (2007).<sup>124</sup> Copyright (2007) The American Physical Society. (b) “Stress-strain curves for shear deformations of graphene monolayers, obtained through MD simulations. Filled circles (open squares) show results corresponding to shear forces acting on the armchair edge (zigzag edge) of graphene. Dashed lines are guides to the eye.” Reproduced from G. Kalosakas, N. N. Lathiotakis, C. Galiotis, and K. Papagelis, Journal of Applied Physics **113**, 134307 (2013),<sup>121</sup> with the permission of AIP Publishing.

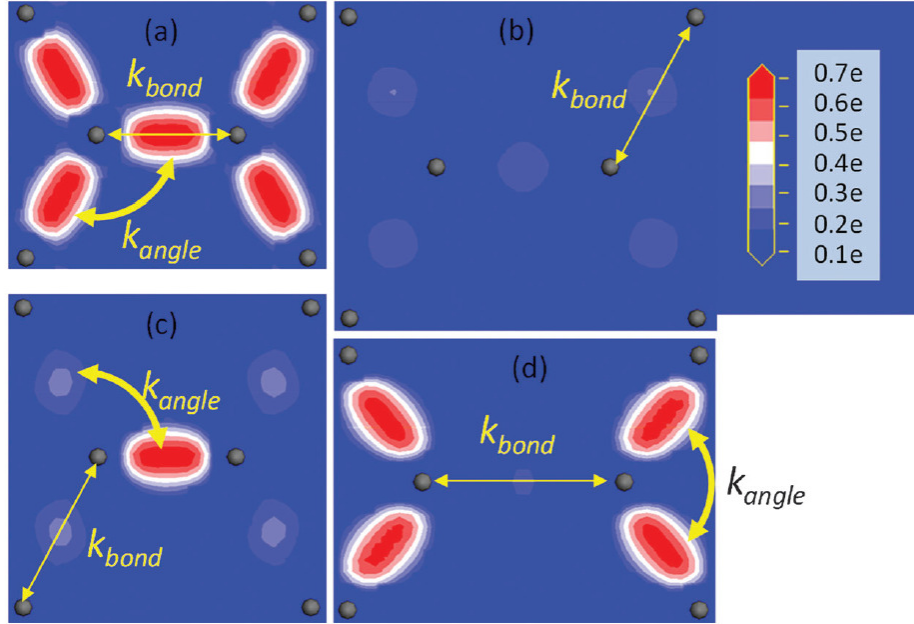


FIG. 4. “The electron density distribution contour of graphene under different tensile loads, (a)  $\epsilon=0$ ; (b) biaxial tension at  $\epsilon=0.28$  (the bond stretching ratio  $\xi=0.25$ ); (c) uniaxial tension along the zigzag direction at  $\epsilon=0.28$  (the bond stretching ratio  $\xi(\text{Bond I})=0.2$ ,  $\xi(\text{Bond II})=-0.03$ ); (d) uniaxial tension along the armchair direction at  $\epsilon=0.28$  (the bond stretching ratio  $\xi(\text{Bond I})=0.36$ ,  $\xi(\text{Bond II})=0.003$ ). Reproduced with permission from Phys. Chem. Chem. Phys. **18**, 1657 (2016).<sup>125</sup> Copyright 2016 The PCCP Owner Societies.

804 **V. GRAPHENE IN INTERACTION WITH ITS ENVIRONMENT AT**  
 805 **HIGH PRESSURE**

806 The mechanical properties of graphene can be probed by high pressure. In bulk materials,  
 807 high-pressure experiments can characterize the bulk modulus and its pressure derivative  
 808 through the equation of state, which links the volume variation to pressure. Many bulk  
 809 systems are anisotropic, and have an anisotropic elastic stiffness tensor  $c_{ij}$ . With more than  
 810 one atom per primitive cell, as in graphene, internal strains may occur. Particularly for 2D  
 811 systems, bond or directional compressibilities can be defined to fully describe the changes in  
 812 atomic positions due to the deformation under hydrostatic pressure.<sup>126</sup> Graphene is however  
 813 not only highly anisotropic but also is only one atom thick. While its in-plane deformation  
 814 modifies the C-C separation or  $sp^2$  bond length, its out-of-plane deformation can only be

815 described as deformation of the  $\pi$ -orbitals.

816 In high-pressure experiments, both the C-C  $sp^2$  bonds and the spatial extension of the  
817  $\pi$ -orbitals will be modified by interactions with the surrounding PTM (anything from he-  
818 lium, argon, through to water, ethanol or various oils), which itself increases in density  
819 with pressure. Interactions between graphene and the surrounding medium can range from  
820 weak vdW to strong covalent interactions. In particular, the vdW interactions will become  
821 stronger under pressure. The  $\pi$ -orbitals may become highly modified under pressure, per-  
822 haps creating strong dipolar interactions with neighboring molecules. At what point could  
823 we consider the system to be something other than graphene (as, *e.g.* graphene oxide)? The  
824 effects of pressure may be simply to change the graphene thickness, or may include doping  
825 or hybridization. As in any material, the  $c_{ij}$  are expected to increase with pressure, but  
826 since all the carbon atoms in graphene are in contact with the environment, we may expect  
827 that  $c_{ij}$  will depend on pressure and temperature, and also on the environment. It is likely  
828 that  $c_{33}$  will be most influenced by the pressure and the environment. But are the pressure  
829 dependencies of other parameters dominated by the pressure or by the environment? How  
830 best to compare the pressure responses of graphene and graphite? These issues are addressed  
831 here.

832 Graphene can be studied in suspension, with PTM on both sides, and when the PTM  
833 is liquid, the graphene is free of non-hydrostatic strains. When graphene is supported by a  
834 substrate, the situation is quite different. We must consider what differences are significant,  
835 and what can be learned from these different environments.

836 This section has three parts treating the pressure response of graphene in the different  
837 environments depicted in Fig. 5. First, we will discuss the case of graphene in suspension  
838 in a fluid as shown in Fig. 5 (a). Then, the case of supported graphene immersed in a fluid  
839 PTM (b). Finally, the case of graphene sandwiched between two different (Fig. 5 (c.1)) or  
840 identical (Fig. 5 (c.2)) solids. The Fig. 5 (c) cases are also relevant to help understand the  
841 mechanical response of graphene in composite materials.

## 842 A. Suspended graphene in a fluid PTM

843 This may be considered as the paradigmatic pressure experiment, with the two variants  
844 of Fig. 5(a). A few Raman scattering experiments have been reported corresponding to

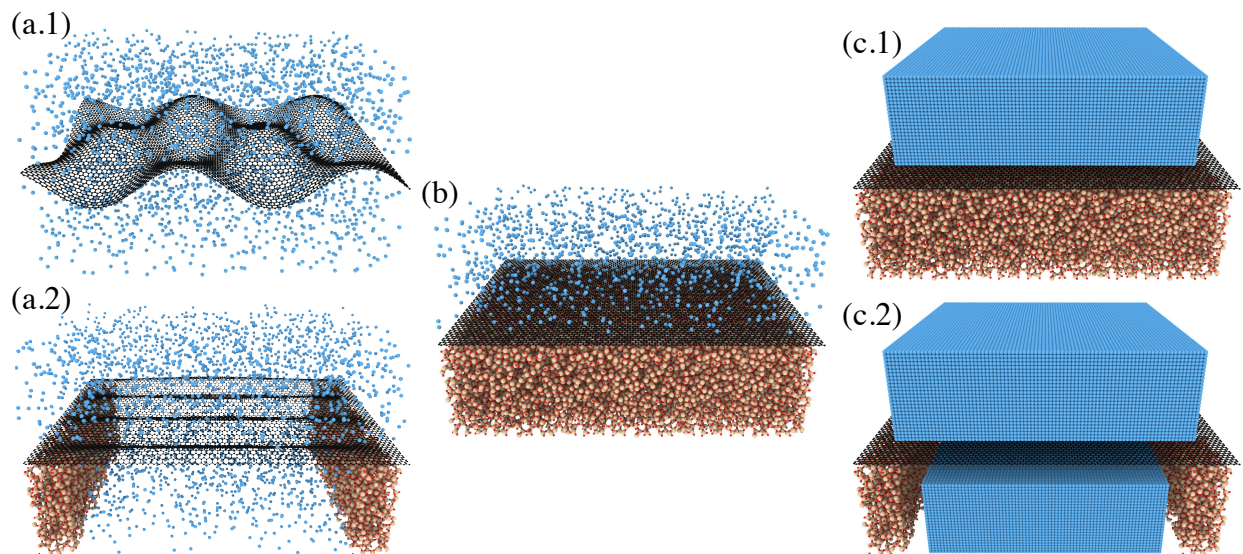


FIG. 5. The various cases encountered in high-pressure experiments and discussed in this section are: (a) suspended graphene in a fluid PTM, (b) supported graphene in a fluid PTM, and (c) graphene sandwiched between two solids. In cases (a) and (c), one needs to distinguish between (a.1) free-standing graphene and (a.2) graphene across a hole ; and (c.1) graphene sandwiched between two different solids and (c.2) graphene in a single solid. The presence of ripples is shown in (a.1) and wrinkles in (a.2).

845 these configurations: an ensemble of graphene layers in suspension and considered separated  
 846 each from the others (Fig. 5(a.1)) or supporting an individual graphene layer  
 847 substrate (Fig. 5(a.2)). In both cases, we may note that the graphene may not be flat due to  
 848 the spontaneous formation of ripples (Fig. 5(a.1)) and wrinkles (Fig. 5(a.2)).<sup>127,128</sup> Wrinkles  
 849 and ripples differ by their aspect ratio.<sup>127</sup> Ripples are isotropic, with an amplitude  $\sim$  nm,  
 850 and an aspect ratio  $\sim$  1. Wrinkles are more aligned and larger, having an aspect ratio  $>$  10,  
 851 due to the partial decoupling of bending and stretching modes.<sup>50,127,128</sup>

852 In Fig. 5 (a.2), while the graphene sheet may be under tension at ambient pressure  
 853 (resulting in wrinkles with an axis perpendicular to the trench),<sup>127</sup> we might expect that  
 854 differential contraction under pressure of the support and the graphene (unless the support  
 855 is made of diamond) would result in a loss of tension and eventually buckling in a different  
 856 direction or even crumpling.<sup>127</sup> However, this may be prevented by the evolution of the  
 857 adhesion of graphene to the internal walls of the trench. [Bunch \*et al.\* observe a minimum](#)

TABLE IV. Summary of high-pressure Raman experiments on suspended graphene.

Type	PTM <sup>1</sup>	$P_{hydrostatic}$ ( $P_{Max}$ ) [GPa]	$\frac{\partial\omega_G}{\partial P}$ hydro ( $P_{Max}$ ) [cm <sup>-1</sup> /GPa]	Ref
suspension <sup>(2)</sup>	N <sub>2</sub>	2 (8)	4.7	34
supported <sup>(3)</sup>	Fluorinert	1.0 (4.2)	- (5.6)	37
suspension	DMF	1.6 (7)	5.4	40
supported <sup>(4)</sup>	H <sub>2</sub> O	1.0 (35)	- (3.4)	131

(1) see text

(2) The sample were films with a mixture of monolayer, bilayer and few-layer graphene and having 2D characteristic signature of few-layer graphene rather than single-layer graphene.

(3) From the detachment from graphene supported on Si/SiO<sub>2</sub> using as PTM a 1:1 mixture of Fluorinert FC70 and FC77 (nonpolar).

(4) A gold microscopy grid was used to suspend graphene.

858 non-zero tension,<sup>129</sup> due to this, and analysed by Lu and Dunn.<sup>130</sup>

859 All high-pressure experiments on suspended graphene have used Raman spectroscopy as a  
860 probe. Raman spectroscopy does not give direct access to the pressure evolution of the unit  
861 cell parameters which would determine the elastic constants. Raman spectroscopy provides  
862 nevertheless a signature of the response of the C-C interatomic potential through the G-  
863 mode pressure dependence. Table IV summarizes the most relevant results from suspended  
864 graphene studies.

865 All the studies in Table IV were done using different PTM (FC-70 is perfluorotripropyl-  
866 amine and FC-77 is a perfluorocycloether; DMF is N,N-dimethylformamide). Only two  
867 studies (using nitrogen and DMF as the PTM) were performed in hydrostatic conditions  
868 throughout the pressure range (*i.e.* with a liquid PTM). On the other hand, the nitrogen  
869 PTM study was of a mixture of monolayer, bilayer and few-layer graphene, which makes its  
870 results difficult to interpret. The DMF PTM study is the only one in which a G-band pres-  
871 sure dependence has been obtained for a monolayer graphene sample suspended in liquid.  
872 This study was able to obtain a  $\frac{\partial\omega_G}{\partial P}$  in hydrostatic conditions from a careful analysis from  
873 a total of 4 pressure points in the DMF hydrostatic domain up to 1.6 GPa. The value of  
874 5.4 cm<sup>-1</sup>/GPa was obtained with a linear fit and 5.6 cm<sup>-1</sup>/GPa with a quadratic fit using

875 the quadratic coefficient of the graphite fit.<sup>28</sup> These are 15 to 25 % higher than the graphite  
876 G-mode slope which is 4.3 – 4.7 cm<sup>-1</sup>/GPa using the same quadratic coefficient.<sup>28</sup> This  
877 difference is partly due to the non-negligible impact of interlayer-coupling on the in-plane  
878 vibrations in graphite (see Sec. VI C). There are reports pointing to PTM-induced charge  
879 transfer to graphene in polar media<sup>132,133</sup> even from the first stages of compression,<sup>133</sup> and of  
880 pressure-induced reactivity with water.<sup>134</sup> Doping, *p* or *n*, leads to an enhanced value of the  
881 G-mode frequency<sup>135</sup> which may explain an increase of the G-mode pressure coefficient in  
882 graphene. Experiments using an inert PTM would clarify whether there is a difference be-  
883 tween graphene in-plane elastic constants and those of graphite, or if the observed differences  
884 are related to polarization-induced modifications of the electronic structure of graphene.

885 Another interesting aspect is that, as pressure is increased, the PTM fluid viscosity  
886 increases. The vdW graphene-fluid interaction may overcome the thermal energy of the  
887 fluid molecules. An organized fluid layer may then appear in contact with graphene. This  
888 constitutes a loss of 2D character which may also affect the mechanical properties of graphene  
889 and may explain differences in the Raman response with different PTM. DFT and MD  
890 modelling - DFT is performed at zero temperature - have in fact shown in carbon nanotubes  
891 under high pressure the formation of a structurally coherent contact layer of CO<sub>2</sub> or water  
892 around carbon nanotubes.<sup>136,137</sup> In fact, DFT modelling shows that in carbon aromatic  
893 systems such as benzene, vdW interaction plays an important role in phase stability at high  
894 pressures.<sup>138</sup>

895 We may conclude this part by underlining that dipole or other enhanced VdW interactions  
896 with the PTM molecules and the possible loss of 2D character through the formation of a  
897 PTM contact layer need to be explored as possible mechanisms modifying the graphene  
898 mechanical properties at high pressure.

## 899 B. Supported Graphene in a fluid PTM

900 This is the case depicted in Fig. 5 (b), *i.e.* graphene on a substrate and immersed in a  
901 fluid PTM. In this case, the PTM applies hydrostatic pressure on the graphene-substrate  
902 system. With increasing pressure, the substrate (unless it is diamond) contracts much faster  
903 than the graphene, which puts the graphene under a large biaxial compression. How much  
904 graphene contracts and is strained in response to the substrate shrinking is governed by the

905 graphene-substrate adhesion and friction, graphene/PTM adhesion, graphene stiffness, and  
906 graphene bending modulus. We will now discuss the role of each parameter.

### 907 **1. Role of the substrate**

908 Graphene stiffness is one of the largest-ever measured, with a Young’s modulus of  $\sim 1$  TPa  
909 (Table II),<sup>25,139</sup> while its bending stiffness is often considered as negligible,<sup>140,141</sup> indeed so  
910 small that it is hard to measure in a direct manner. Many reported values (depending on  
911 the temperature and flake size) are often about 1 eV,<sup>142</sup> and it was measured in carbon nan-  
912 otubes as 1.7 eV (see Sec. III D 5).<sup>45</sup> Thus, it is expected that graphene will tend to bend or  
913 wrinkle rather easily in order to relieve in-plane compression.<sup>143–145</sup> The interaction between  
914 the graphene layer and its supporting surface, namely the graphene-substrate adhesion, is  
915 therefore an extremely important parameter governing the graphene response to biaxial  
916 compression: if the graphene-substrate adhesion is poor, the graphene will not fully follow  
917 the substrate’s deformation and instead will slide or wrinkle to reduce its stress. However,  
918 the adhesion of graphene to its substrate is an intricate mixture of (a) the interaction energy  
919 between carbon and surface atoms, (b) substrate surface roughness, (c) graphene number  
920 of layers, (d) commensurability of the graphene and substrate lattices, and (e) the normal  
921 force from the PTM, which must modify the effects of (a) to (d). As a consequence, each  
922 graphene-substrate system is unique and the amount of strain transferred from the substrate  
923 to the graphene layer can only be assessed in a phenomenological way, for example with a  
924 “strain transfer efficiency” parameter  $\alpha$ .<sup>38,146</sup> Now to discuss each of these parameters:

925 (a) The strength of the graphene-substrate interaction energy can be assessed from the  
926 graphene-substrate distance, which varies greatly from one substrate type to another – as  
927 shown in Table I which gives some experimentally measured distances. Graphene deposited  
928 on metals tends to form covalent bonds that greatly decrease the graphene-substrate dis-  
929 tance. This would correspond to a much increased adhesion energy and forces for peeling  
930 off and for sliding. One thus expect the strain transfer efficiency  $\alpha$  to be close to 1 in such  
931 systems – and  $\alpha = 1$  for a copper substrate was indeed observed up to a critical stress of  
932 2 GPa.<sup>34,38</sup> Moreover, the history of the graphene sample plays a huge role in the interaction  
933 with its substrate: whether the graphene was transferred or grown on the substrate has  
934 a large impact on its adhesion and residual stress. As discussed in Sec. III D 3, epitaxial

935 graphene is under large strain after cooling (hence showing  $\alpha = 1$ ), whereas CVD (usually  
936 on Cu) graphene shows the occurrence of ripples to release the stress (resulting in a  $\alpha < 1$ ).  
937 An even lower  $\alpha$  on Cu is expected if graphene is transferred onto it.

938 (b) When the surface roughness is too high, total unbinding from the substrate surface  
939 can occur, at ambient pressure<sup>145,147</sup> or under high pressure.<sup>37</sup> Some substrates show the oc-  
940 currence of a critical stress beyond which the strain transfer efficiency is greatly diminished,<sup>38</sup>  
941 which is probably due to a partial unbinding of the graphene layer from its substrate. While  
942 not measured experimentally, this critical stress is supposed to be roughness-dependent for  
943 a given substrate. The substrate surface roughness also greatly influences the *friction* be-  
944 tween the graphene layer and its substrate, which in turns plays a role on the mechanism of  
945 the mechanical response of graphene to biaxial compression. When the strain transfer effi-  
946 ciency  $\alpha < 1$ , it means that either (a) graphene slips all over the substrate; or (b) graphene  
947 wrinkles, ripples or crumples. Or a combination of (a) and (b) may occur. In the case of a  
948 rough substrate with a conforming graphene (as is the case most of the time), case (a) has  
949 an extended energy cost because it involves the whole graphene surface, while case (b) only  
950 involves the local elastic energy cost of buckling. Depending on the substrate roughness, a  
951 varying proportion of slipping and buckling may thus occur. However, the application of a  
952 normal force by the hydrostatic pressure to the surface will certainly hinder the formation of  
953 wrinkles or ripples. Wrinkles were however observed under hydrostatic pressure (at 4 GPa)  
954 even in nano-graphite ( $\sim 30$ -layer graphene).<sup>148</sup>

955 (c) In the same manner, adhesion to a rough substrate is decreased when the number  
956 of graphene layers increases, *i.e.* when the graphene bending rigidity increases.<sup>36</sup> With  
957 an increasing number of layers, the conformation of graphene to its rough substrate may  
958 decrease, resulting in a decreased friction. We may note that in MoS<sub>2</sub>, which has a much  
959 higher bending stiffness than graphene, a bimodal behavior has been seen when supported  
960 on Si/SiO<sub>2</sub>. A mixture of regions showing strong adhesion and other regions showing weak  
961 adhesion was seen.<sup>149</sup>

962 (d) Finally, it was for example shown that for a given substrate such as Co(0001), the  
963 graphene-substrate distance decreases when the graphene lattice is matched with the sub-  
964 strate lattice,<sup>150</sup> allowing for covalent C-Co bonding. Such an effect therefore plays a large  
965 role on the starting *stress+doping* state of graphene. In the following however, we will not  
966 consider substrates in which this type of interaction may happen. Pressure-induced doping

967 effects will then be due essentially to interaction with the PTM and will be discussed in  
968 the following subsection. One should also note that the (in)commensurability of the lattices  
969 should also play a role in the friction between graphene and its substrate.

970 (e) All these parameters may be impacted by the modification of the graphene-substrate  
971 distance due to the application of pressure. However, in pressure ranges for which the PTM  
972 is liquid (hydrostatic pressure), the graphene Raman response is always linear,<sup>34,37,38,40,131,133</sup>  
973 which tends to show that this effect is limited at pressures below  $\sim 10$  GPa.

974 The mechanical response of graphene to high pressures is usually followed through *in situ*  
975 Raman spectroscopy, as stress induces a deformation of the carbon bonds and thus shifts  
976 the Raman features such as the G-mode ( $\omega_G$ ) or the 2D-mode ( $\omega_{2D}$ ). But similar shifts can  
977 also arise from doping. Graphene is a  $\pi$ -conjugated 2D material, thus its electronic struc-  
978 ture is highly sensitive to its environment. This charge sensitivity allows doping through  
979 gating or intercalating (“substrate doping”, see *e.g.* Ref. 151 for a review), but it can also  
980 occur due to the interaction with polar molecules in the PTM which can be enhanced at  
981 high pressure<sup>133</sup> (“PTM doping”). Overall, the doping and strain contribution to the  $\omega_G$   
982 shift can be unravelled by following the slope of  $\partial\omega_{2D}/\partial\omega_G$ <sup>151,152</sup> (see Fig. 6). Finally, the  
983 substrate type and the graphene preparation method (as-prepared, transferred, synthesised,  
984 exfoliated...) play a large role in the  $\omega_G$  frequency<sup>150,151</sup> and the graphene-substrate dis-  
985 tance (Table I). Large variations of the  $\omega_G$  peak position can be observed for graphene on  
986 a substrate according to the crystallographic orientation, matching or random. For exam-  
987 ple, while  $\omega_G = 1581 \text{ cm}^{-1}$  for free graphene, it redshifts down to  $1452 \text{ cm}^{-1}$  for oriented  
988 graphene on Co(0001), and it can vary between  $\sim 1550$  and  $1600 \text{ cm}^{-1}$  across a single sam-  
989 ple of misaligned graphene on Co(0001).<sup>150</sup> In the case of Co(0001), matching the graphene  
990 and substrate lattice orientations allows chemical bonding between the two, resulting in a  
991 shortening of the graphene-substrate distance and a significant stretching of the graphene  
992 lattice, thus decreasing the  $\omega_G$  frequency. However, this is peculiar to Co(0001) as, usually,  
993 the CVD synthesis of graphene on a metallic substrate results in a compressive stress of the  
994 graphene layer, and thus an increased  $\omega_G$  frequency.<sup>151</sup> On the other hand, the incommen-  
995 surability of both lattices can result in large local variations of the  $\omega_G$  position, that can be  
996 due to both strain and/or doping.

997 In conclusion, the substrate plays a very important role both at ambient pressure and  
998 under high pressure. Before the application of pressure, and together with the history of

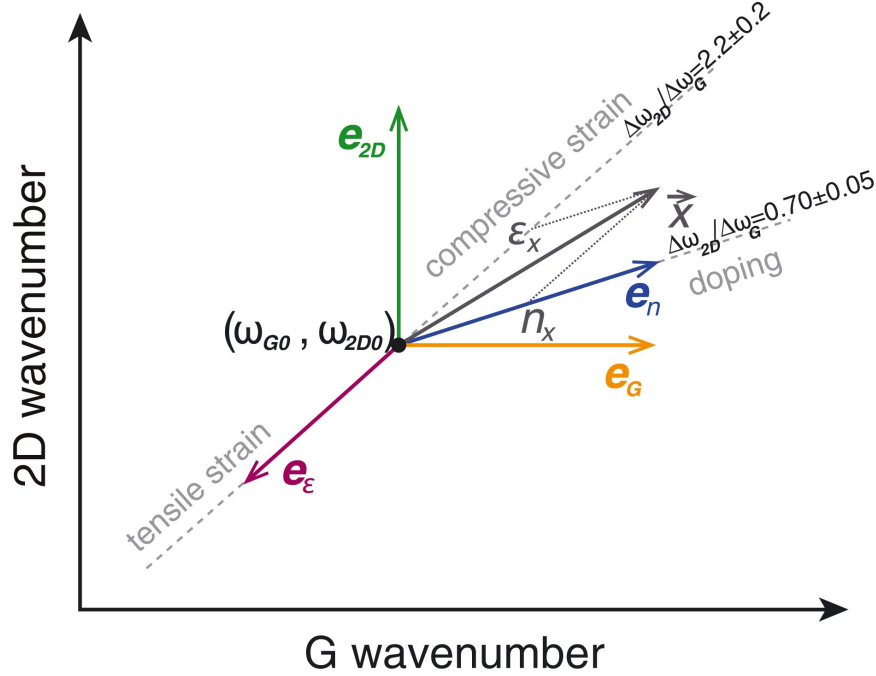


FIG. 6. Lee diagram<sup>152</sup> allowing retrieving the strain and doping ( $\varepsilon_X$  and  $n_X$ ) at a point  $X$  in the  $(\omega_G, \omega_{2D})$  space. The origin  $(\omega_G, \omega_{2D})_0$  is the reference state at ambient conditions. Reproduced with permission from J. Raman Spectrosc. **49**, 130 (2018).<sup>151</sup> Copyright 2018 John Wiley & Sons, Ltd.

999 the sample, the substrate determines the reference state of the graphene, *i.e.* the graphene-  
1000 substrate distance as well as the initial stress and doping states. During pressure application,  
1001 it determines the strain of the graphene layer through the phenomenological parameter  $\alpha$ ,  
1002 this strain being relative to the initial state. It is inappropriate to consider the evolution  
1003 of the Raman G-mode frequency as a function of pressure;<sup>38</sup> rather, it should be considered  
1004 as a function of the strain, the actual strain depending on the reduction of the substrate  
1005 dimensions. Overall, in the simple case where  $\alpha = 1$  and *in the absence of doping*, a Raman  
1006 G-mode frequency dependence on substrate strain  $\varepsilon$  of  $\frac{\partial \Delta \omega_G}{\partial \varepsilon} = -60 \pm 3 \text{ cm}^{-1}/\%$  is expected.<sup>38</sup>  
1007 Since  $\frac{\omega}{\omega_0} = (1 + \varepsilon)^{-2\gamma_{E_{2g}}}$  for in-plane biaxial compression,<sup>34</sup> this corresponds to a Grüneisen  
1008 parameter  $1.8 < \gamma_{E_{2g}} < 2.0$  – in excellent agreement with uniaxial strain experiments<sup>33</sup> and  
1009 *ab initio* modeling.<sup>153</sup> This further confirms the importance of substrate-induced biaxial  
1010 strain on the properties of graphene.

## 1011 2. Role of the PTM

1012 *a. Mechanical response* When the PTM is fluid, it has a much larger compressibility  
1013 than the substrate. This, of course, is of no importance while it exerts purely hydrostatic  
1014 pressure. However, fluid PTM display large viscosities at pressures in the GPa range, and  
1015 local crystallisation of the fluids occurs at the graphene surface.<sup>154</sup> Whatever the state of  
1016 the PTM, this configuration results in a biaxial stress field in the system: the top surface  
1017 of the graphene layer is in contact with the fluid that applies hydrostatic stress, while  
1018 its bottom surface is in contact with the solid substrate which imposes a bi-axial stress  
1019 that is determined by the equation of state of the substrate. By symmetry, there are no  
1020 shear stresses  $\sigma_{xz}$  and  $\sigma_{yz}$  applied to the graphene, except at the edges and other lateral  
1021 inhomogeneities.

1022 In the case of monolayer graphene, the mechanical response of the graphene layer is mainly  
1023 governed by the substrate.<sup>34,36–38,146</sup> In the case of bilayer graphene, that remains so while the  
1024 PTM remains liquid<sup>133</sup> (however, after solidification of the PTM, a stress gradient between  
1025 layers could be measured, as will be discussed in the next section). One might expect, indeed,  
1026 that the application of pressure would result in an increased graphene-substrate adhesion by  
1027 reducing the graphene-substrate distance; and also that it would prevent the graphene layer  
1028 from buckling and hence forming wrinkles or ripples. As mentioned in (b) above, substrate  
1029 surface roughness can cause a critical stress above which the graphene layer is not able to  
1030 follow the deformation of its substrate.<sup>38</sup> So the reality is more complex: despite gigapascals  
1031 of pressure applied on the graphene layer, it seems that it is still able to buckle to reduce  
1032 stress.<sup>148</sup>

1033 To sum up, while the PTM remains liquid, the evidence is that the *mechanical response*  
1034 of graphene is fully governed by the adhesion to the substrate. This goes for mono- and  
1035 bilayer graphene only; for thicker samples the graphene bending rigidity increases and the  
1036 adhesion to the (usually rough) substrate is reduced, leading to a mechanical response closer  
1037 to graphite.<sup>36,146</sup>

1038 *b. Electronic response* Comparing inert PTM (such as Ar, N<sub>2</sub>) with polar PTM (such  
1039 as 4:1 methanol:ethanol), a significant increase in the pressure coefficient of the Raman G-  
1040 band was reported, from  $\sim 7$  to  $\sim 10$  cm<sup>-1</sup> GPa<sup>-1</sup> for SiO<sub>2</sub>/Si substrate), for both mono-  
1041 and bilayer graphene.<sup>36</sup> This change was however later refuted.<sup>37,38</sup> Nevertheless, a pressure-

1042 induced decrease of the G-band FWHM was observed when using 4:1 methanol:ethanol  
1043 PTM, which was attributed to a doping contribution.<sup>36</sup> However, it was not clear whether  
1044 this doping remained constant over the whole pressure range.<sup>37</sup> A recent study of twisted  
1045 isotopically-labelled bilayer graphene in 4:1 methanol:ethanol PTM by Forestier *et al.*<sup>133</sup>  
1046 clarified the doping effect of the PTM. Here, the observation of a difference in the response  
1047 of the two layers made it possible to conclude that there was a pressure-induced doping due  
1048 to the alcohol PTM: the G-mode of the upper layer in contact with the PTM showed a  
1049 larger pressure shift than the lower layer in contact with the substrate, demonstrating the  
1050 occurrence of a doping due to the polar PTM which increases with pressure. It is worth  
1051 mentioning here that the isotopically-labelled bilayer graphene of this study is made of two  
1052 CVD graphene layers transferred on top of each other, resulting in a sample behaving like  
1053 two independent layers on top of each other. The difference in isotopic masses decouples the  
1054 G-modes of the two layers, so that they can be separately resolved.

### 1055 C. Graphene sandwiched between two solids

1056 The investigation of the mechanical behavior of graphene monolayers and bilayers inter-  
1057 acting with solids under pressure on both sides, as in Fig. 5 (c), constitutes an interesting  
1058 route to better understand the mechanical properties of graphene-based nanocomposites.

1059 Under sufficient pressure, any fluid transforms to a solid at ambient temperature. There-  
1060 fore, increasing the pressure sufficiently in the two situations discussed in the previous sub-  
1061 sections, the systems will evolve to i) graphene between two different solids (Fig. 5 (c.2), for  
1062 supported graphene on a substrate) or ii) graphene between two identical solids (Fig. 5 (c.1),  
1063 for graphene in suspension). This leads to an asymmetrical or to a symmetrical environment.

1064 Crystallization of the PTM has at least two effects. First, macroscopically, it modifies the  
1065 stress field with the appearance of differential strain at the graphene-PTM interface. Second,  
1066 microscopically, it creates a periodic potential in interaction with the graphene sheet.

#### 1067 1. *Different solids*

1068 Crystallization of the PTM when compressing a supported graphene leads to an asymme-  
1069 try of the environments and of the associated stress fields. Each side of the graphene plane

1070 is in contact with a different solid medium. However, the change of state (fluid to solid) of  
1071 the PTM is usually unnoticed in high-pressure Raman spectroscopy on supported monolayer  
1072 graphene.<sup>146</sup> The preferred PTM are soft vdW solids (such as argon or nitrogen) and are  
1073 considered to provide quasi-hydrostatic conditions even after solidification.<sup>155</sup> The bonding  
1074 of such solids only leads to weak vdW type interactions with the graphene. The interactions  
1075 between these solids and the graphene can only marginally modify the pressure-induced  
1076 behavior which remains dominated by the effect of the substrate.<sup>146</sup>

1077 In contrast, crystallization of the PTM is clearly observed by Raman spectroscopy exper-  
1078 iments on bilayer graphene where each layer experiences different conditions. The signature  
1079 of the solidification is a change in the pressure-dependence of the G-peak position and/or a  
1080 change of the width of this peak. The change of slope may be attributed to additional differ-  
1081 ential strain components and the broadening is related to inhomogeneity of the stress field.  
1082 As the spectroscopic signatures are mainly affected by these external effects, it is difficult  
1083 to assess any intrinsic effect, *i.e.* any modification of the elastic properties of graphene.

1084 The difference of the applied stress on each side of a twisted bilayer graphene have been  
1085 evidenced and quantified by the high-pressure Raman experiment on isotopically labelled  
1086 bilayer graphene mentioned in Sec. VB2b. Strain differences up to  $\sim 0.1\%$  between the  
1087 two graphene layers were observed when applying pressures of up to 10 GPa with nonpolar  
1088 solid environments.<sup>133</sup>

## 1089 **2. Identical solids**

1090 There are only a few reports of high-pressure experiments on graphene in suspension  
1091 above the crystallization pressure of the PTM. It represents a major experimental challenge  
1092 to characterize and manipulate a mono- or bi-layer, to load it in a high-pressure cell as  
1093 suspended and to follow experimentally the high-pressure behavior across and above the  
1094 solidification of the PTM. A particularly important issue is the form of suspension. If the  
1095 graphene is freely floating in the PTM, then after solidification it will be subject to the  
1096 strain of the PTM as pressure is further increased and the sample volume decreases and  
1097 changes shape. However, if the graphene is supported over a trench in a substrate, then  
1098 after solidification it will be pressed down into the trench, as the PTM will typically be  
1099 much more compressible than the substrate, and this will put the graphene under high

1100 tensile strain.

1101 Table IV includes data from studies before and after solidification of the PTM. Sun *et al.*  
1102 dissolved PMMA on which CVD-grown graphene had been transferred.<sup>40</sup> The solvent (DMF)  
1103 was used as the PTM. So this graphene was assumed to be freely-floating. The G-peak pres-  
1104 sure coefficient changed at around 2 GPa, from 5.4 cm<sup>-1</sup>/GPa to 7.5 cm<sup>-1</sup>/GPa. This  
1105 was interpreted as resulting from the adhesion to the more compressible solid PTM, with  
1106 the strain transmission effect as for supported graphene. In Tao *et al.*<sup>131</sup> bilayer graphene  
1107 suspended on Au grid was sandwiched between ice in different phases. It was not possible  
1108 to fit the G-band data evolution using the quadratic term of graphite determined by Han-  
1109 fland *et al.*<sup>28</sup> Tao *et al.* report a linear G-band evolution with a low pressure coefficient of  
1110 3.4 cm<sup>-1</sup>/GPa up to pressures of 40 GPa<sup>131</sup> without any noticeable variation at the PTM  
1111 freezing point. Filintoglou *et al.*<sup>37</sup> observed graphene sandwiched in solid fluorinert and  
1112 obtained a G-band pressure slope of 5.4 cm<sup>-1</sup>/GPa. These results, with G-band pressure  
1113 coefficients between 3.4 and 7.5 cm<sup>-1</sup>/GPa, show the extreme sensitivity of graphene to the  
1114 nature of the PTM, and the details of the experiment influencing the transmitted strain.  
1115 Solidification has a drastic impact for suspended graphene, contrary to the previous case,  
1116 supported graphene, for which the solidification has almost no noticeable effect. The high-  
1117 pressure mechanical response of graphene can be related to graphene composites. In partic-  
1118 ular, and not surprisingly, it has been shown that the level of adhesion between graphene  
1119 and polymer matrix is a key factor in the mechanical response of nanocomposites.<sup>156,157</sup>

1120 After solidification (crystallization or vitrification), the main issue the nature of the ap-  
1121 plied stress that includes shear components. However, one may consider the effect of the  
1122 increasing pressure on the intrinsic mechanical properties of graphene, especially the  $c_{33}$  elas-  
1123 tic constant. Increasing interaction between  $\pi$ -orbitals and the surrounding solid media can  
1124 strongly modify the  $\pi$ -orbitals and hence perhaps the  $sp^2$  bonds. A detailed quantification  
1125 will be introduced in Sec. VIC. This seems to be especially true of polar PTM that ex-  
1126 hibit piezo-doping and ultimately the formation of covalent bonds.<sup>134</sup> In this case, graphene  
1127 cannot be considered still as an isolated system under external perturbation.

## 1128 VI. DRESSED GRAPHENE

### 1129 A. Functionalisation

1130 Graphene can react with, for instance, oxygen, hydrogen or fluorine. When covalent bonds  
1131 develop with other molecules in low proportions we may speak about defective graphene.  
1132 When those bonds develop extensively we will prefer to speak about other materials, some  
1133 aperiodic, such as graphene oxide, some periodic, such as graphane (hydrogenated graphene  
1134 monolayer) or diamane (hydrogenated bilayer of graphene)<sup>158</sup> (see Fig. 7) or fluorinated  
1135 single-layer diamond.<sup>159</sup> In these cases there will be either local or extended modifications of  
1136 the covalent graphene bonding scheme, with a modification of the associated elastic stiffness  
1137 constants. For single-layer graphene oxide, the experimental Young's modulus derived from  
1138 AFM measurements is substantially reduced to  $207.6 \pm 23.4$  GPa.<sup>160</sup> As most of these other  
1139 materials are new, their properties are derived from *ab initio* calculations.<sup>161</sup> For instance  
1140 it has been shown by DFT calculations that graphene oxide with increasing proportions  
1141 of (-O) or (-OH) displays a progressive elongation of the C-C bond and a softening of the  
1142 mechanical properties.<sup>162</sup>

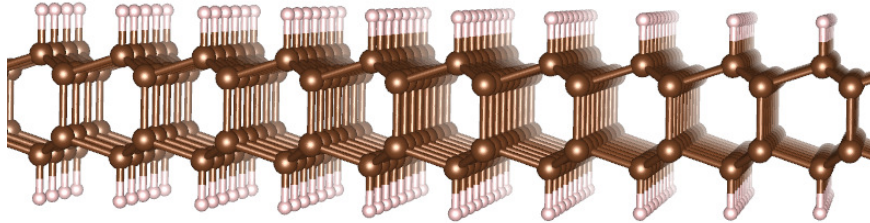


FIG. 7. Diamane structure with  $sp^3$  bonding for C atoms.

### 1143 B. Derivative geometry

1144 We may also consider making a nanotube by rolling up a graphene sheet until we connect  
1145 the edges through covalent bonds. This change in geometry leads to a topologically different  
1146 graphene-based system, the carbon nanotube. Of course, the synthesis of carbon nanotubes  
1147 does not correspond with this *gedanken* experiment, which, rather, raises the issue whether  
1148 carbon nanotubes should be considered to be a material, derived from graphene by the

1149 change in geometry, or to be a structure made of graphene. Many DFT calculations find  
1150 that the in-plane Young's modulus of small-diameter carbon nanotubes walls is reduced, due  
1151 to the curvature-induced modification of the C-C hybridization. We may then expect that  
1152 extensively corrugated, ripple or wrinkled graphene could exhibit an average bonding scheme  
1153 differing from flat graphene and hence with different local 2D elastic stiffness constants as  
1154 well as the large-scale reduced stiffness due to the corrugation. See Sec. VII for further  
1155 discussion of nanotubes.

### 1156 C. Effect of vdW interactions

1157 Geometry and covalent bonding have an effect on the 2D elastic stiffness constants of  
1158 graphene. What about vdW interactions? Consider the difference between graphene in  
1159 graphite and in epitaxially grown bilayer graphene, two different cases of vdW graphene  
1160 stacking. In graphite the vdW distance between graphene layers is 3.35 Å which may be  
1161 considered as the graphene thickness in that particular case (see Sec. II A and Table I). In  
1162 bilayer graphene grown on a SiC(0001) surface, the measured graphene-graphene distance is  
1163 3.24 Å.<sup>163</sup> In multilayer graphene grown on an SiC substrate, the distance between graphene  
1164 layers is found to be 3.9 Å after the first graphene layer in contact with the SiC substrate.<sup>164</sup>  
1165 X-ray diffraction measurements have revealed a certain degree of rotational disorder in the  
1166 stacking of these graphene layers.<sup>116</sup> Do these differences in thickness imply changes in the  
1167 C-C sp<sup>2</sup> bonding?

1168 The thickness of graphene in these different cases is to be related to the extension of its  $\pi$ -  
1169 orbitals. This is certainly a point of view in rupture with the Galilean continuum mechanics  
1170 approach, but wholly consistent with the modern approach to the radius of atoms. In  
1171 vacuum, of course, quantum mechanics tells us that the spatial extension of the  $\pi$ -orbitals  
1172 electron cloud is to infinity, like the hydrogen 1s state. Any definition of a finite extension  
1173 of an electron orbital in vacuum (such as the Bohr radius) is thus entirely arbitrary. Indeed  
1174 such definitions are better described as characteristic lengths (such as the Bohr radius) which  
1175 are not arbitrary, but also not obviously the extension or size of the atom. Where the  $\pi$ -  
1176 orbitals of a graphene monolayer are delimited by meeting the electronic orbitals of adjacent  
1177 materials, their extension is to be defined in just the same way as the size of atoms is defined  
1178 (see Sec. II A and V). ) In the case of graphite, it is very simple - the distance to the point

1179 between the graphene layers about which the  $\pi$ -electron density is symmetrical. In the case  
 1180 of a graphene monolayer with other materials either side, or multilayer graphene in other  
 1181 than Bernal stacking, we need to seek criteria (as with the size of atoms in multi-element  
 1182 mixtures and compounds) which allow the consistent attribution of a thickness to, e.g. the  
 1183 side of a graphene monolayer in contact with another layer in AA or in turbostratic contact,  
 1184 and also to the other side in contact with perhaps sapphire. We should certainly define the  
 1185 graphene thickness in the asymmetric context as the addition of two different contributions  
 1186 on each side of the carbon nuclei.

1187 Practically, the shift of the G-mode frequency under out-of-plane compression is a suitable  
 1188 quantity to quantify the weak modification of the in-plane elastic constants by deformation  
 1189 of  $\pi$ -orbitals. The G-mode, as mentioned previously, is an in-plane anti-phase vibration  
 1190 of C-C atom pairs and is therefore closely related to the in-plane stiffness of graphene and  
 1192 graphite. Its eigenvectors ( $E_{2g}$ ) in graphene and graphite are shown in Fig. 8. The dynamical  
 1193 equation of a 1D spring can be written as  $Ku = \omega^2 u$ , where  $K$  is the force constant,  $u$  is  
 1194 the displacement and  $\omega$  is the frequency. And it can be extended to 2D for the G-mode of  
 1195 graphene:<sup>166</sup>

$$\begin{pmatrix} \omega_0^2 & 0 \\ 0 & \omega_0^2 \end{pmatrix} \begin{pmatrix} u_1 \\ u_2 \end{pmatrix} = \omega^2 \begin{pmatrix} u_1 \\ u_2 \end{pmatrix}, \quad (11)$$

1196 where the  $u_1$  and  $u_2$  are the relative displacement of the two carbon atoms along the two  
 1197 equivalent in-plane directions, as the hexagonal lattice of graphene is isotropic in-plane.  
 1198 When an additional graphene layer is added, Eq. 11 becomes<sup>167</sup>

$$\begin{pmatrix} \omega_0^2 & 0 & C & 0 \\ 0 & \omega_0^2 & 0 & C \\ C & 0 & \omega_0^2 & 0 \\ 0 & C & 0 & \omega_0^2 \end{pmatrix} \begin{pmatrix} u_1 \\ u_2 \\ u_3 \\ u_4 \end{pmatrix} = \omega^2 \begin{pmatrix} u_1 \\ u_2 \\ u_3 \\ u_4 \end{pmatrix}, \quad (12)$$

1199 where  $u_3$  and  $u_4$  are the displacement of the two carbon atoms in the added layer, and  $C$   
 1200 accounts for the interlayer coupling. The longitudinal and transverse modes are not coupled  
 1201 due to the hexagonal lattice, hence all the zero elements in the force constant tensor. The  
 1202 solutions to the secular equation of Eq. 12 are

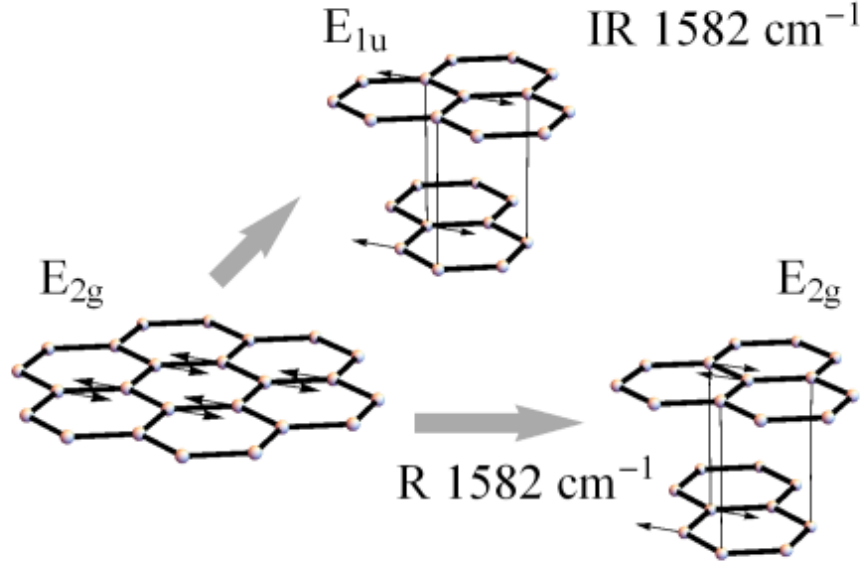


FIG. 8. “Phonon eigenvectors of graphene and graphite. Every phonon eigenvector of graphene gives rise to two vibrations of graphite. For example, the in-phase combination of the two layers for the  $E_{2g}$  optical mode of graphene yields  $E_{2g} \otimes A_{1g} = E_{2g}$  and the out-of-phase combination  $E_{2g} \otimes B_{1u} = E_{1u}$ . Next to the graphite modes it is indicated whether they are Raman (R) or infrared (IR) active and the experimentally observed phonon frequencies. The translations of graphite are omitted from the figure.” Reproduced with permission from Phil. Trans. Roy. Soc. A **362**, 2271 (2004).<sup>165</sup> Copyright 2004 The Royal Society.

$$\begin{aligned}\omega_{(1)}^2 &= \omega_0^2 + C \\ \omega_{(2)}^2 &= \omega_0^2 + C \\ \omega_{(3)}^2 &= \omega_0^2 - C \\ \omega_{(4)}^2 &= \omega_0^2 - C\end{aligned}$$

1203 The two different solutions correspond to the  $E_{1u}$  and  $E_{2g}$  G-modes of graphite, where car-  
 1204 bon atoms in both layers in a unit cell vibrate in-plane and in anti-phase, but the vibrations of  
 1205 the two layers are in-phase and out-of-phase, respectively. Typical experimentally measured  
 1206 values of the graphite  $E_{1u}$  and  $E_{2g}$  frequencies are 1587 and 1580  $\text{cm}^{-1}$ , respectively.<sup>27,168</sup>  
 1207 From the measured frequencies of  $E_{1u}$  and  $E_{2g}$  of graphite, we can calculate the  $\omega_0=1583.5$

1208  $\text{cm}^{-1}$  for the G-mode of a graphene plane in graphite – the G-mode frequency of graphene  
 1209 should be slightly higher than graphite, even their in-plane stiffnesses are the same.

1210 To quantify the effect of deformation of the  $\pi$ -orbitals on the G-mode frequency, we can  
 1211 introduce out-of-plane strain and calculate the shift of G-mode frequency. The off-diagonal  
 1212 term  $C$  in Eq. 12 for interlayer coupling can be expanded in terms of out-of-plane strain  
 1213  $\varepsilon_{zz}$ . The diagonal terms can be expanded too, to account for the possible modification of  
 1214 the in-plane  $\text{sp}^2$  bond stiffness by the compression of the  $\pi$ -orbitals,

$$\begin{pmatrix} \omega_0^2 + A\varepsilon_{zz} & 0 & C + B\varepsilon_{zz} & 0 \\ 0 & \omega_0^2 + A\varepsilon_{zz} & 0 & C + B\varepsilon_{zz} \\ C + B\varepsilon_{zz} & 0 & \omega_0^2 + A\varepsilon_{zz} & 0 \\ 0 & C + B\varepsilon_{zz} & 0 & \omega_0^2 + A\varepsilon_{zz} \end{pmatrix} \begin{pmatrix} u1 \\ u2 \\ u3 \\ u4 \end{pmatrix} = \omega^2 \begin{pmatrix} u1 \\ u2 \\ u3 \\ u4 \end{pmatrix} \quad (13)$$

1215 and the solution to the secular equation is:

$$\begin{aligned} \omega_{(1)}^2 &= \omega_0^2(E_{2g}^{(2)}) + (A + B) \times \varepsilon_{zz} \\ \omega_{(2)}^2 &= \omega_0^2(E_{2g}^{(2)}) + (A + B) \times \varepsilon_{zz} \\ \omega_{(3)}^2 &= \omega_0^2(E_{1u}) + (A - B) \times \varepsilon_{zz} \\ \omega_{(4)}^2 &= \omega_0^2(E_{1u}) + (A - B) \times \varepsilon_{zz} \end{aligned}$$

1216 which indicates an increasing  $E_{1u}$  and  $E_{2g}$  splitting, and therefore different shift rates with  
 1217 pressure of these two modes. Without the contribution from the coupling to adjacent layers,  
 1218 the G-mode frequency of graphene under out-of-plane compression is  $\omega = \omega_0 + A \times \varepsilon_{zz}$ .  
 1219 Sun *et al.* calculated the G-mode frequencies of graphite under out-of-plane compression  
 1220 by DFT, and introduced a new parameter  $\gamma'$  to compare the contribution from out-of-plane  
 1221 strain on with that from in-plane strain.<sup>167</sup>

$$\frac{\Delta\omega}{\omega_0} = -\gamma(\varepsilon_{xx} + \varepsilon_{yy}) \mp \frac{1}{2}SDP(\varepsilon_{xx} - \varepsilon_{yy}) - \gamma'\varepsilon_{zz} \quad (14)$$

1222 where  $\gamma$  is the Grüneisen parameter and SDP is the shear deformation potential. The  
 1223 values of  $\gamma'$  are  $-0.0131$  and  $0.0585$  for  $E_{2g}$  (GM) and  $E_{1u}$  of graphite, respectively, and the  
 1224 value for the GM of graphene is in the middle. These values, compared to a typical value  
 1225  $1.90$  of the Grüneisen parameter for the in-plane strain contribution,<sup>33,62,166</sup> are indeed very  
 1226 small. However, both graphene and graphite are about 30 times more compressible out-of-  
 1227 plane than in-plane.<sup>20</sup> So, under hydrostatic compression, the contribution to the G-mode

1228 frequency from out-of-plane compression, while smaller than the in-plane contribution, is  
1229 not negligible.

1230 Three useful points can be summarised from the above discussion: first, deformation  
1231 of  $\pi$ -orbitals can modify the in-plane bond stiffness by a non-negligible amount, especially  
1232 when the vdW interaction between graphene and the surrounding medium increases under  
1233 compression; second, although the G-mode is a good measure of in-plane stiffness, its fre-  
1234 quencies in graphene and graphite are slightly different even if the in-plane stiffnesses are  
1235 the same; and third, the shift rate of the monolayer graphene G-mode with pressure should  
1236 be higher than that graphite, because for the graphene G-mode, there is no impact from the  
1237 coupled vibration in adjacent layers.

1238 Returning to the issue of different vdW interactions with different media at ambient  
1239 pressure, some authors have proposed that the graphene layers in multilayer graphene on  
1240 4H-SiC(0001) behave as monolayer graphene<sup>116</sup> due to the predominant rotational stacking  
1241 faults weakening the graphene-graphene interaction. Hence, following the same principle of  
1242 thickness definition, the flat turbostratic (free-standing) graphene thickness will be 3.9 Å,  
1243 *i.e.*  $\sim 6.5\%$  greater than the vdW graphite distance.

1244 We may then conclude that different schemes of vdW stacking lead to changes in the  
1245  $\pi$ -orbitals. If we need to consider effects on the 2D elastic stiffness constants of the  $\pi$ -  
1246 orbitals, then they should be considered as affected by graphene stacking schemes. The  
1247 effect of such changes on the  $sp^2$  bonds are from deformed  $\pi$ -orbitals modifying the in-plane  
1248 C-C  $sp^2$  bonds. The weak modifications of the C-C  $sp^2$  bonds by the  $\pi$ -orbitals can be  
1249 quantified in detail as above. In particular, as graphene is little affected by weak van der  
1250 Waals interactions or geometry variations with curvatures less than about  $\sim 1\text{ nm}^{-1}$ , the  
1251 electronic structure bonding scheme determining the 2D elastic constants of graphene is  
1252 preserved. Flat or weakly bent graphene in vacuum or in graphite or in single-wall and  
1253 multi-wall nanotubes may be then considered as having the same 2D elastic constants as  
1254 graphite.

## 1255 VII. CARBON NANOTUBES: PROPERTIES OF GRAPHENE

1256 Carbon nanotubes, particularly single-walled and double-walled carbon nanotubes, are  
1257 interesting structures in their own right (but that is outside the scope of this review). They

1258 provide perhaps the only way in which graphene can be studied free-standing and in vacuum  
 1259 - graphene with nothing touching either side and nothing to constrain it in-plane either.  
 1260 Closed nanotubes provide the opportunity to study graphene with vacuum inside and other  
 1261 media outside, while open-ended nanotubes provide other possibilities. Most important, and  
 1262 our focus here, they can reveal aspects of the mechanical properties of graphene, such as its  
 1263 bending stiffness, that are difficult or impossible to study in other forms of graphene. Many  
 1264 of the opportunities to learn about graphene by studying nanotubes have not yet been fully  
 1265 exploited, as we shall see below.

1266 Most of the work we discuss depends on Raman spectroscopy, observing the G-mode and  
 1267 the other graphene/graphite phonons, but crucially the radial breathing mode (RBM) which  
 1268 has no equivalent in graphite.

## 1269 A. G-mode in nanotubes

1270 The G-mode has the inconvenience that it is hard to resolve the contributions of nan-  
 1271 otubes of different diameters and chiralities. For that reason, much more attention has been  
 1272 paid to the RBM (Sec. VII B).

1273 The G-mode frequency is sensitive to confinement effects, dynamical effects, and curva-  
 1274 ture, which lift the degeneracy to give  $G^+$  and  $G^-$  peaks.<sup>169</sup> In Piscanec *et al.*,<sup>169</sup> the effect  
 1275 of curvature is deduced from the difference between experimental phonon wavenumbers and  
 1276 calculations and obeys  $\Delta\omega = -\zeta \times d^{-2}$ . Values are given for the TO mode (circumferential  
 1277 motion) with  $\zeta = 25.16 \text{ cm}^{-1}\cdot\text{nm}^2$  and LO modes (axial motion) with  $\zeta = 12.0 \text{ cm}^{-1}\cdot\text{nm}^2$ .  
 1278 Up to now, there is no direct calculation of the curvature effect. However, it can be esti-  
 1279 mated from a simple continuum model. We consider the thickness of the graphene  $h_G$  and  
 1280 treat the electrons on both sides ( $i$  for inner and  $o$  for outer) in a first approximation as a  
 1281 continuous medium. The tension ( $o$ ) and compression ( $i$ ) are opposite but not equal, giving  
 1282 a strain at the centre. Energy equilibrium gives  $\epsilon_i^2 \times (d/2 - h_G/4) = \epsilon_o^2 \times (d/2 + h_G/4)$ .  
 1283 For a curved plate, we have:  $\epsilon_o = h_G/2d$ . So we deduce the average strain for the center  
 1284 to be  $\langle \epsilon \rangle = (\epsilon_i + \epsilon_o)/2 = h_G^2/(8d^2)$ . Using the strain coefficient  $-57 \text{ cm}^{-1}/\%$ ,<sup>170</sup> we find  
 1285  $\Delta\omega_{TO} = -80.0 \times d^{-2}$ . This gives the correct dependence on  $d$  but too large a value for  $\zeta$ .  
 1286 However, a homogenous medium is not a satisfactory model for graphene (*c.f.* the Yacobson  
 1287 paradox, Sec. II A). Refining the model as a structure, ( $\sigma$  bonds at the centre, and  $\pi$  for

1288 the inner and outer material), the relation is the same but the coefficient is different. From  
 1289 energy equilibrium, we have  $\epsilon_\sigma = \sqrt{\frac{c_{11}^\sigma(h_G-h_\sigma)}{c_{11}^\pi h_\sigma}} \times \epsilon_\pi = \sqrt{\frac{c_{11}^\sigma(h_G-h_\sigma)}{c_{11}^\pi h_\sigma}} \times \epsilon_\pi = 0.170 \times \epsilon_\pi$  leading  
 1290 to  $\Delta\omega_{TO} = -13.6 \times d^{-2}$ , which is in a more reasonable range and  $\epsilon_\sigma = \frac{2.38 \times 10^{-3}}{d^2}$ , to be  
 1291 compared with  $\frac{1.6 \times 10^{-3}}{d^2}$  from calculation.<sup>171</sup>

## 1292 B. RBM in nanotubes

1293 In the RBM fundamental, all atoms move radially together. The restoring force is  
 1294 straightforwardly due to  $c_{11}$ , and the frequency depends inversely on the diameter, and to a  
 1295 much lesser extent on the chirality, in the 100-300  $\text{cm}^{-1}$  region of the spectrum. Moreover,  
 1296 tunable excitation picks out those tubes that are resonant with the excitation wavelength.  
 1297 Consequently, very detailed studies of the RBM have been reported.<sup>172</sup>

1298 Simple models can account for this mode using continuous mechanics or atomic descrip-  
 1299 tions. We start by supposing the nanotube wall to consist of a 2D sheet of continuum  
 1300 material with the 2D graphene elastic constants  $c_{11}^{2D} = c_{11}d = 372 \text{ Nm}^{-1}$  and  $c_{12}^{2D} = c_{12}d =$   
 1301  $47 \text{ Nm}^{-1}$ . In the RBM motion, the wall has tangential strain but no axial strain (the RBM  
 1302 frequency is too high to induce any axial motion), so the relevant elastic stiffness constant  
 1303 is  $c_{11}^{2D}$ . In contrast, the approach of Mahan,<sup>173</sup> modelling with a three-dimensional isotropic  
 1304 plate, invokes not only  $c_{11}$  but also  $c_{12}$ , which is incorrect. The potential energy per unit  
 1305 length of tube at the extreme of a sinusoidal motion  $r = A \cos \omega t$  is

$$U_{max} = \frac{1}{2} c_{11}^{2D} \epsilon^2 \times 2\pi R_C = \pi R_C c_{11}^{2D} \frac{A^2}{R_C^2} \quad (15)$$

1306 while the kinetic energy at the center of the motion is

$$E_{max} = \frac{1}{2} mA^2\omega^2 = \frac{1}{2} A^2\omega^2 \times 2\pi R_C N m_0 \quad (16)$$

1307 where  $N = 3.8 \times 10^{19}$  is the number of carbon atoms of mass  $m_0$  in a unit area of graphene.  
 1308 Equating  $U_{max}$  and  $E_{max}$ , and rearranging, we have

$$\omega_{RBM} = \frac{1}{R_C} \sqrt{\frac{k_{11}}{N m_0}} \equiv \frac{235}{d(nm)} \text{cm}^{-1} \quad (17)$$

1309 where the diameter  $d = 2R_C$ , in excellent agreement with experiments.<sup>174</sup> At much higher  
 1310 frequency, 1590  $\text{cm}^{-1}$ , the G-mode phonon corresponds to atomic motion in antiphase. To

1311 relate the RBM to the G-mode considering atomic motion, a 1D model (atoms equispaced  
 1312 around a circle) has been proposed by Gerber *et al.*<sup>175</sup> leading to :

$$\omega_{RBM} = \frac{a_0}{d} \omega_G = \frac{0.142 \text{nm} \times 1590 \text{cm}^{-1}}{d(\text{nm})} = \frac{226}{d(\text{nm})} \text{cm}^{-1} \quad (18)$$

1313 in excellent agreement with Eq. 17. Considering a 2D system, the equations are the same  
 1314 because the  $E_{2g}$  G-mode is doubly degenerate in the plane allowing the basis to be aligned  
 1315 with the chiral vector, which is the circumference. The approximation here is that the  
 1316 G-mode degeneracy is not lifted by the curvature.

1317 For nanotubes in a medium (e.g. a liquid or nanotube bundles) the vdW interaction leads  
 1318 to an upshift of the RBM frequencies above the values of Eq. 17 by some  $10 - 20 \text{ cm}^{-1}$ .  
 1319 The stiffening of the vdW interaction under pressure is largely responsible for the further  
 1320 increase of RBM frequencies under pressure.<sup>136</sup>

1321 The phonon spectrum of nanotubes includes also the soft modes, in the  $10 - 100 \text{ cm}^{-1}$   
 1322 spectral region, which are the higher-order modes of a series in which the RBM is the zeroth  
 1323 member. Unlike the RBM, the soft modes depend on the bending stiffness  $D$ . The  $n^{\text{th}}$  soft  
 1324 mode has  $2n + 2$  nodes around the circumference of the tube. They should soften under  
 1325 pressure, and would go to zero frequency at the collapse pressure. However, like the RBM,  
 1326 they are raised in frequency by the vdW interaction with the PTM, and the increase in this  
 1327 interaction with pressure actually results in the soft modes stiffening instead of softening  
 1328 under pressure.<sup>176</sup>

### 1329 C. SWCNTs under pressure

1330 The pressure dependence of single-walled nanotubes provides two opportunities at least  
 1331 to learn about graphene. The diameters of nanotubes are usually given as defined by the  
 1332 nuclear positions, [in contrast to taking the outside diameter over the electron orbitals](#). That  
 1333 is what the general formula  $d = a_0 \sqrt{n^2 + mn + m^2}$  gives, and that is the diameter usually  
 1334 considered when analysing the response of nanotubes to high pressure, for example, the rate  
 1335 of shift of the G-mode and RBM phonon frequencies under pressure. If the pressure  $P$  were  
 1336 applied at the radius  $r = d/2$ , pressure coefficients of, for example, the G-mode phonon would  
 1337 be expected to be approximately  $r/h$  times the graphite or graphene pressure coefficients,  
 1338 where  $h$  is the relevant graphene thickness (see Sec. II A). (A full analysis would take into

1339 account the differing tangential and axial stresses in a tube under pressure, respectively  $Pr$   
1340 and  $Pr/2$ .) However, if the graphene has a thickness  $h$  and the pressure is applied at a  
1341 radius  $r + h/2$ , the stresses on the  $sp^2$  bonds will be greater and the pressure coefficients  
1342 correspondingly increased. How much they are increased, however, depends critically on the  
1343 mechanical properties of graphene and their response to pressure and bending. We are not  
1344 aware of a full analysis along these lines of the nanotube pressure coefficients. The situation  
1345 is further confused by the stiffening of the RBM mode which is largely due to the increasing  
1346 vdW interaction between the PTM and the nanotube,<sup>136</sup> and also by any effects of the PTM  
1347 on the graphene as discussed in the previous section, which may account for the different  
1348 pressure coefficients reported for nanotubes in different PTM.<sup>177–180</sup>

#### 1349 D. SWCNT Collapse

1350 At sufficiently high pressures or large diameters, nanotubes collapse. Collapse of nan-  
1351 otubes under high pressure has also been challenging, not least because, apparently as ob-  
1352 vious a case of Euler buckling as the collapse of pillars, the collapse of tubes under external  
1353 hydrostatic pressure is mathematically intractable. Many experimental observations have  
1354 been interpreted as corresponding to collapse, at a very wide range of pressures, and fitted to  
1355 a variety of theoretical equations. A complete solution for the simple (ideal) elastic ring was  
1356 reported only in 2011.<sup>181</sup> Good agreement with the Levy-Carrier formula for a thin-walled  
1357 tube,  $P_C = \frac{3D}{R^3}$  where  $D$  is the bending stiffness was confirmed, and the collapse to a peanut  
1358 shape above  $P_C$  was found to be quite slow, complete only at about  $1.5P_C$ .<sup>182</sup> Torres-Dias  
1359 *et al.* reported that this fitted experimental data for the quenching of the RBM for a range  
1360 of SWCNT diameters, giving an estimate of  $D = 1.7$  eV.<sup>45</sup>

1361 Some caveats must be mentioned. First, the effects of the thickness  $h$  need to be known  
1362 and taken into account, as for the pressure coefficients. Also, it is clear that vdW inter-  
1363 actions will reduce the collapse pressure, so that SWCNTs tubes above about 4 nm will  
1364 spontaneously collapse (the same physics as the folding of Sec. III D 6). This scarcely affects  
1365 smaller tubes where the bending energies involved are very much greater. Then, for diam-  
1366 eters below about 1 nm, Torres-Dias *et al.*<sup>45</sup> reported that the collapse pressure is reduced  
1367 below the Levy-Carrier formula. This is quite a strong effect, observed experimentally and  
1368 in theoretical modelling,<sup>45</sup> and also previously noticed by Elliott *et al.*<sup>183</sup> It extrapolates to

1369  $P_C = 0$  for a diameter of about 0.4 nm, not much smaller than the smallest nanotubes ever  
1370 reported.<sup>184</sup> One source of this behaviour could be softening of the bending potential with  
1371 angle. Another source is the reduction in the Euler buckling load even of straight pillars  
1372 when the compliance is discretised rather than continuous. This effect is reported by Carter  
1373 et al,<sup>77</sup> and discussed in Sec. III D 5. Both of these explanations remain to be analysed in  
1374 detail.

1375 When the diameter of a SWCNTs is large enough, *i.e.* above about 5 nm, a spontaneous  
1376 collapse occurs. This leads to a cross-section in the form of a dogbone or peanut with a  
1377 twist along the axis<sup>185</sup> if the SWCNT is free (in liquid or gas for example). The cavities of  
1378 the edges have a diameter of the order of  $C_{60}$  fullerene, like the cavities of folded graphene  
1379 (Section III D 6) while the stacking depends on the chirality.<sup>186</sup> Indeed, the phenomenon is  
1380 very closely related to folding, with the same balance between adhesion energy and bending  
1381 stiffness. Like folding, it has not been fully exploited to refine our knowledge of these two  
1382 important mechanical parameters of graphene.

1383 Del Grande *et al.*<sup>187</sup> note that the energy barrier for a circular tube to collapse is many eV,  
1384 so it should not be possible for it to happen through thermal activation – but once initiated  
1385 at one point in the tube, the collapse will readily propagate along the tube. This is not an  
1386 uncommon situation in condensed matter physics. It may be compared with the initiation  
1387 of plastic deformation in a perfect crystal, where the activation energy for the creation of  
1388 a dislocation is very high, or with boiling in a pure liquid, where the activation barrier for  
1389 the formation of a bubble is very high. In these examples as in doubtless many others, it is  
1390 a local defect, impurity, or perturbation that breaks the impasse. Del Grande *et al.* suggest  
1391 that the collapse of large SWCNTs is likely to be produced by small mechanical stresses  
1392 that naturally occur during synthesis. The nanoscale force required to initiate collapse, to  
1393 bypass the energy barrier, is about 5 nN<sup>187</sup> which is easily achievable in AFM compression  
1394 experiments.<sup>188</sup>

## 1395 E. DWCNTs coefficients under pressure

1396 While the mechanical behaviour of SWCNTs under pressure is reasonably well understood  
1397 as described in the previous section, double-walled nanotubes provide further opportunities  
1398 - and challenges - to better understand the mechanical properties of graphene. Again, these

1399 opportunities come from the pressure coefficients of the phonon modes while the tubes  
1400 remain circular, and then from the collapse pressures and modes of collapse. Many papers  
1401 report pressure coefficients of the Raman G-modes of the outer and inner walls of DWCNTs  
1402 which are not dissimilar. Yet it is hard to understand how the external pressure may be  
1403 transmitted to the inner tube, given the enormous anisotropy of the graphite elastic stiffness  
1404 tensor. Moreover, the sum of the reported pressure coefficients of the inner and outer tube  
1405 is usually considerably in excess of the coefficient of an empty outer tube, *i.e.* an SWCNT of  
1406 the same diameter. Yet the load on the walls of the inner and out tubes should sum to the  
1407 load of an SNCNT of the same diameter, and so therefore should the pressure coefficients.

1408 Experimentally, pressure transmitted to an inner nanotube can be monitored by the  
1409 upshift of the GM or RBM. The former should be less dependent on the PTM as the upshift  
1410 is from the C-C bond stiffening under pressure, whereas the latter is from the increasing  
1411 interaction of a tube with its surroundings. Consequently, it is easier to describe the GM  
1412 pressure coefficient. The experimental challenge to monitor pressure by the GM frequency  
1413 is the assignment of the GM to tubes of a specific diameter and chirality, and, further, to  
1414 distinguish inner and outer tubes in DWCNTs. While the RBM is diameter-dependent,  
1415 tubes of different diameters have very similar GM frequency, if not the same, at ambient  
1416 condition. [An ideal situation would be to have only one RBM and its corresponding G-mode](#)  
1417 [dominating the spectrum \(either due to a special sample containing only one chirality, or](#)  
1418 [having only one chirality in resonance at a specific laser excitation\)](#). Many factors can add to  
1419 the complication of the situation: 1) common CNT samples contain tubes of many different  
1420 chiralities; 2) many more than one chirality can be in resonance or close to the resonance  
1421 condition; 3) while the outgoing laser energy is only shifted by 10 – 20 meV for the RBM,  
1422 the difference is 200 meV for the GM, making it possible that the GM is in resonance with  
1423 the outgoing laser while its corresponding RBM is far from the resonance condition; 4)  
1424 for DWCNTs, one has to further assign Raman peaks to the outer or the inner tube, and  
1425 the interaction between inner and outer tubes modifies the Kataura plot,<sup>172</sup>. In particular,  
1426 Hirschmann *et al.*<sup>189</sup> showed that the wall-to-wall distance between inner and outer tubes in  
1427 DWCNTs increases with increasing tube diameters, which makes the RBM upshifts of the  
1428 inner tubes from intertube interaction no longer a constant, as most earlier work supposed.  
1429 This requires further caution on the assignment of RBMs to inner tubes, but can be used  
1430 to refine our calculations if needed.

1431 Early studies on DWCNTs under pressure observed at least two components in a GM  
 1432 profile, shifting with pressure at different rates. It is tempting to assign these two components  
 1433 to outer and inner tubes for two reasons, one is that stress transmitted to the inner tube  
 1434 should be lower than hydrostatic pressure, resulting in two different responses to pressure,  
 1435 and the other is that outer (or inner) tubes in resonance at the same condition can have very  
 1436 close diameters and they should response similarly to pressure. Among various work, the  
 1437 GM pressure coefficients can be different, as different tubes are in resonance; they can be  
 1438 either PTM dependent, as PTM modifies the transition energy of CNTs, making different  
 1439 tubes in resonance, or PTM independent as no other charility in those samples is available  
 1440 near the resonance condition. The results of these high pressure study on DWCNTs are  
 1441 summarised in Table V below.

TABLE V. Experimental shift rates of DWCNTs GM with pressure.

Outer tube ( $\text{cm}^{-1}\text{GPa}^{-1}$ )	Inner tube ( $\text{cm}^{-1}\text{GPa}^{-1}$ )	PTM	Laser Excitation (nm)	Reference and notes
9.6	6.4	paraffin oil	514	Ref. 190
8.4	5.5	NaCl	514	Ref. 190
5.8	3.3	methanol-ethanol	633	Ref. 191
6.9	4.1	Oxygen	633	Ref. 191
8.6	5.1	Argon	633	Ref. 191
5.5	4.3	methanol-ethanol	514	Ref. 192

1442

1443

1444 In this section we have seen that much could be learned about the mechanical proper-  
 1445 ties of graphene from further experimental and theoretical work on nanotubes, particularly  
 1446 under pressure. The major obstacle is that the RBM modes are highly resonant and the  
 1447 resonances shift with pressure. For the G-mode, this means that as pressure increases, dif-  
 1448 ferent diameter tubes (which are not well-resolved) may dominate the Raman spectrum at  
 1449 different pressures.<sup>193</sup> For the RBM the tubes of different diameters and chiralities are well-  
 1450 resolved. However, both for identifying or for choosing which tubes are observed, and for  
 1451 tracking given tubes over a substantial pressure range, tunable Raman excitation is needed  
 1452 (*e.g.* a dye laser or Ti-sapphire laser), together with a tunable Raman spectrometer. The  
 1453 number of laboratories worldwide with such equipment, and also a high-pressure capability,

1454 is small indeed.

## 1455 VIII. MODELS FOR THE MECHANICS OF GRAPHENE

1456 Mechanical properties, more perhaps than any other properties of matter, invite the  
1457 construction of models, for purposes ranging from visualisation, through understanding, to  
1458 prediction. We comment briefly here on what can be suitably expressed by or learnt from  
1459 different models, starting from the simplest. Continuum models for graphene have been  
1460 considered. The flat plate of isotropic material and a thickness chosen to give the right  
1461 bending stiffness was mentioned in Section II A. While useful for considering the behaviour  
1462 of graphene as a beam, plate or shell, the model does not attempt to replicate the thickness  
1463  $a_{33}$  or the out-of-plane compressibility  $c_{33}$  of graphite. For that reason a continuum model  
1464 was considered in which the nuclei and the  $sp^2$  bonding orbitals were treated as an infinitely  
1465 thin sheet with the 2D  $c_{11}$  and  $c_{12}$  values of graphene, sandwiched between two layers of soft  
1466 material modelling the pi-orbitals.<sup>39</sup> This model could replicate the thickness, the bending  
1467 stiffness and the out-of-plane compressibility by a suitable choice of an anisotropic 3D elastic  
1468 tensor for this soft material. The model is suitable for considering the behaviour of, for  
1469 example, nanotubes under pressure (see above, Sec. VII C). For example, it can be used to  
1470 consider questions such as the radius at which a nanotube is loaded by external pressure. It  
1471 is also a model that can be readily discretised as a ball-and-spring model. In this case, the  
1472 nuclei are the balls, the  $sp^2$  bonds are springs (2D stretching potentials) between them and  
1473 the pi-orbitals are springs that terminate on a point that is not an atom. These points could  
1474 also be joined by springs that give the bending stiffness.<sup>39</sup> That introduces the question,  
1475 whether this is the physically-realistic representation of the origin of the bending stiffness of  
1476 graphene, or whether it actually arises from the torsional stiffness of the  $sp^2$  bonds through  
1477 4-atom potentials in-plane. A comparison with the torsional vibrational modes of ethane  
1478 ( $sp^3$ ) and ethylene ( $sp^2$ ) could be useful here,

1479 At this point we are approaching the valence force field (VFF, Keating) models<sup>194</sup> and  
1480 those used in MD and Monte Carlo simulation. Keating, however, used only two-atom  
1481 (stretch) and three-atom (angular) springs, or interactions, with nearest neighbours only to  
1482 model the elastic constants  $c_{ij}$  and internal strains of, *e.g.* silicon. Keating did not consider  
1483 phonon frequencies. It is in considering the phonons as well as the elastic constants that

1484 Keating models tend to break down.

1485 In MD simulation, Ref. 26 used two-atom interactions with atoms out to the fifth-nearest  
1486 neighbours to model the phonon frequencies and the phonon dispersions. The necessity  
1487 to include the fifth-nearest neighbours is demonstrated by investigating the origin of the  
1488 GM frequency. Consideration of the 2D bulk modulus, or area modulus  $A$ , gives the force  
1489 constant of the C-C bonds as 748 N/m, or  $46.7 \text{ eV}/\text{Å}^2$ , from the experimental values of elastic  
1490 constants of graphite.<sup>20</sup> We assume that the GM frequency comes only from the nearest C-C  
1491 stretching, and we can obtain the GM frequency as  $1450 \text{ cm}^{-1}$ . The gap to the experimental  
1492 value of about  $1580 \text{ cm}^{-1}$  can be filled by other contributions beyond the nearest neighbour.  
1493 Quantifying these contributions requires more information than the frequency of LO at  $\Gamma$   
1494 point (G-Mode)<sup>27</sup> in the phonon dispersion relation of graphite. We have already given an  
1495 example that one has to include the second nearest neighbour out-of-plane interaction to  
1496 describe the separation of  $E_{1u}$  and  $E_{2g}$ . It was found that up to the fourth nearest neighbour  
1497 interaction has to be included to well fit the dispersion from  $\Gamma$  point to M (especially the  
1498 initial increase of  $E_{1u}$  frequency from  $\Gamma$  point),<sup>41</sup> obtained by inelastic neutron scattering.<sup>42</sup>  
1499 A further fifth nearest neighbour interaction was included to fit more recent in-elastic x-ray  
1500 data, which gave a finer description of the local minimum of TO at K point.<sup>26</sup> Surprisingly,  
1501 the empirical force constant model including up to the fifth nearest neighbour that fits well  
1502 the experimental data of the full phonon dispersion of graphite (as shown in Fig. 9), gives a  
1503 force constant for the nearest neighbour C-C stretching, as small as  $25.88 \text{ eV}/\text{Å}^2$ , indicating  
1504 that about half of the contributions to the C-C vibrational frequency in graphite come from  
1505 other interactions than the nearest C-C stretching. This is truly unexpected, yet explaining  
1506 the existing data best.

1507 Despite contributing only half to the G-mode frequency, the nearest C-C stretching is  
1508 expected to contribute dominantly to the upshift of G-mode with pressure from Pauli exclu-  
1509 sion, which is a measure of C-C bond anharmonicity. The evolution of the phonon dispersion  
1510 relation in graphite would not only verify or dispute the small value of the nearest C-C force  
1511 constant, but also quantify the anharmonicity, when it becomes available. We should point  
1512 out that in addition to in-plane contributions, the GM frequency can also be modified by  
1513 deformed  $\pi$ -orbitals from out-of-plane, as discussed in section VIB.

1514 It is clear that Keating potentials are not generally capable of representing both the  
1515 elastic constants and the phonon frequencies, and certainly fail in this regard for graphene.



1529 obtaining the electronic structure<sup>201</sup> but is not suitable for mechanical properties.

1530 DFT provides models that can be made to replicate experimental data excellently.<sup>22</sup>  
1531 However, apart from the maps of electron density, there is little in DFT output that can  
1532 assist a physical understanding of the predicted properties. It could be said that in graphene  
1533 research as in high-pressure research, the greatest value of DFT is that it can tell us what  
1534 happens under experimental conditions that are not (yet) accessible to experimenters. For  
1535 that reason we discuss it under different headings above. An example in graphite is the  
1536 determination of  $c_{13}$  (Sec. III A, see also Sec. IV F).

## 1537 IX. CONCLUSIONS

1538 This paper reviews the mechanical properties of graphene, both those that are expected  
1539 to be similar to graphite and those expected to be different from graphite – and anomalies.  
1540 Graphene is commonly called a 2D material, which implies a thickness tending to zero.  
1541 However, the  $\pi$ -electrons above and below the 2D plane of carbon nuclei extend the electron  
1542 density of monolayer graphene into the third dimension, perpendicular to the 2D plane. For  
1543 example, we can define a vdW thickness of graphene, 3.35 Å, which is the experimentally  
1544 measured spacing of graphene layers in graphite. One key conclusion is that, far from being  
1545 a 2D material, graphene has a well-defined 3D structure, which may be modelled in various  
1546 ways to help understand its mechanical properties. That is not to say that it cannot display  
1547 2D physics, much as can a 100 Å quantum well – which has a 3D physical structure of *e.g.*  
1548 GaAs sandwiched between GaAlAs. Following from that, those of its mechanical properties  
1549 which are related to those of graphite are indeed very similar, if not identical.

1550 Without neighboring layers, unsupported graphene is not mechanically stable and has  
1551 intrinsic ripples. The low bending stiffness further promotes the formation of ripples, making  
1552 them common in graphene samples. It also contributes to the softening of the ZA phonon  
1553 dispersion, resulting in a negative thermal expansion (although, again, it is not clear whether  
1554 this is significantly different from that of graphite). Properties such as the out-of-plane  
1555 stiffness, though expected to be similar to graphite, require indirect approaches to define  
1556 and to quantify.

1557 Due to the small sample size of exfoliated graphene – at least out-of-plane – experiments  
1558 to measure many of its mechanical properties requires special design. In addition, the

1559 environment surrounding graphene adds further complexity to the interpretation of these  
1560 experimental data, from determining factors as substrates transferring strain to graphene,  
1561 to subtle modification by influencing the  $\pi$ -orbital distribution.

1562 There are many derivative structures from graphene, in a way making the extraordinary  
1563 properties of graphene tunable. They can also be used to help understand the properties  
1564 of graphene. Among those, measurements on carbon nanotubes in some circumstances give  
1565 the most accurate values for mechanical properties of graphene, perhaps even better than  
1566 measurements on graphene itself, as nanotubes can be self-supporting, free-standing, and  
1567 stable, thus excluding many of those complexities.

1568 Finally, composite materials in which matrix material is reinforced mechanically by the  
1569 inclusion of graphene flakes are perhaps one of the most exciting applications in which the  
1570 mechanical properties of graphene are central. Many other so-called 2D materials are also  
1571 used, and their mechanical properties are often less well characterised than those of graphite.  
1572 One may expect them to be related to the corresponding bulk materials much as graphene  
1573 is related to graphite.

## 1574 **ACKNOWLEDGMENTS**

1575 DGP acknowledges the support from “Graphene Core 3” GA: 881603 which is imple-  
1576 mented under the EU-Horizon 2020 Research and Innovation Actions (RIA) and is finan-  
1577 cially supported by EC-financed parts of the Graphene Flagship.

## 1578 **DATA AVAILABILITY**

1579 Data sharing is not applicable to this article as no new data were created or analyzed in  
1580 this review.

## 1581 **REFERENCES**

- 1582 <sup>1</sup>D. G. Papageorgiou, I. A. Kinloch, and R. J. Young, [Progress in Materials Science](#) **90**,  
1583 [75](#) (2017).  
1584 <sup>2</sup>D. Akinwande, C. J. Brennan, J. S. Bunch, P. Egberts, J. R. Felts, H. Gao, R. Huang,  
1585 J.-S. Kim, T. Li, Y. Li, K. M. Liechti, N. Lu, H. S. Park, E. J. Reed, P. Wang, B. I.

- 1586 Yakobson, T. Zhang, Y.-W. Zhang, Y. Zhou, and Y. Zhu, [Extreme Mechanics Letters](#)  
1587 [13](#), 42 (2017).
- 1588 <sup>3</sup>B. Sundqvist, [Physics Reports](#) (2021), <https://doi.org/10.1016/j.physrep.2020.12.007>.
- 1589 <sup>4</sup>G. Galilei, *Dialogues Concerning Two New Sciences by Galileo Galilei* (New York:  
1590 Macmillan, New York, 1914).
- 1591 <sup>5</sup>M. Short and P. Walker Jr, [Carbon](#) **1**, 3 (1963).
- 1592 <sup>6</sup>B. I. Yakobson, C. J. Brabec, and J. Bernholc, [Phys. Rev. Lett.](#) **76**, 2511 (1996).
- 1593 <sup>7</sup>W. L. B. M.A, [The London, Edinburgh, and Dublin Philosophical Magazine and Journal](#)  
1594 [of Science](#) **40**, 169 (1920).
- 1595 <sup>8</sup>W. P. Davey, [Phys. Rev.](#) **19**, 248 (1922).
- 1596 <sup>9</sup>R. W. G. Wyckoff, [Proc Natl Acad Sci U S A](#) **9**, 33 (1923).
- 1597 <sup>10</sup>G. W. Stewart, [Phys. Rev.](#) **33**, 889 (1929).
- 1598 <sup>11</sup>A. Camerman and J. Trotter, [Acta Cryst](#) **18**, 636 (1965).
- 1599 <sup>12</sup>F. Jean, T. Zhou, N. Blanc, R. Felici, J. Coraux, and G. Renaud, [Phys. Rev. B](#) **91**,  
1600 [245424](#) (2015).
- 1601 <sup>13</sup>P. Sutter, J. T. Sadowski, and E. Sutter, [Phys. Rev. B](#) **80**, 245411 (2009).
- 1602 <sup>14</sup>I. Razado-Colambo, J. Avila, D. Vignaud, S. Godey, X. Wallart, D. P. Woodruff, and  
1603 M. C. Asensio, [Sci. Rep.](#) **8**, 10190 (2018).
- 1604 <sup>15</sup>X. Fei, L. Zhang, W. Xiao, H. Chen, Y. Que, L. Liu, K. Yang, S. Du, and H.-J. Gao, [J.](#)  
1605 [Phys. Chem. C](#) **119**, 9839 (2015).
- 1606 <sup>16</sup>D. Eom, D. Prezzi, K. T. Rim, H. Zhou, M. Lefenfeld, S. Xiao, C. Nuckolls, M. S.  
1607 Hybertsen, T. F. Heinz, and G. W. Flynn, [Nano Lett.](#) **9**, 2844 (2009).
- 1608 <sup>17</sup>A. Dahal and M. Batzill, [Nanoscale](#) **6**, 2548 (2014).
- 1609 <sup>18</sup>Y. Gamo, A. Nagashima, M. Wakabayashi, M. Terai, and C. Oshima, [Surface Science](#)  
1610 [374](#), 61 (1997).
- 1611 <sup>19</sup>G. E. Bacon, [Acta Cryst](#) **4**, 558 (1951).
- 1612 <sup>20</sup>A. Bosak, M. Krisch, M. Mohr, J. Maultzsch, and C. Thomsen, [Phys. Rev. B](#) **75**, 153408  
1613 (2007).
- 1614 <sup>21</sup>O. L. Blakslee, D. G. Proctor, E. J. Seldin, G. B. Spence, and T. Weng, [Journal of](#)  
1615 [Applied Physics](#) **41**, 3373 (1970).
- 1616 <sup>22</sup>N. Mounet and N. Marzari, [Phys. Rev. B](#) **71**, 205214 (2005).
- 1617 <sup>23</sup>M. Birowska, K. Milowska, and J. Majewski, [Acta Phys. Pol. A](#) **120**, 845 (2011).

- 1618 <sup>24</sup>A. G. Kolpakov, [Journal of Applied Mathematics and Mechanics](#) **49**, 739 (1985).
- 1619 <sup>25</sup>C. Lee, X. Wei, J. W. Kysar, and J. Hone, [Science](#) **321**, 385 (2008).
- 1620 <sup>26</sup>M. Mohr, J. Maultzsch, E. Dobardžić, S. Reich, I. Milošević, M. Damnjanović, A. Bosak,  
1621 M. Krisch, and C. Thomsen, [Phys. Rev. B](#) **76**, 035439 (2007).
- 1622 <sup>27</sup>F. Tuinstra and J. L. Koenig, [The Journal of Chemical Physics](#) **53**, 1126 (1970).
- 1623 <sup>28</sup>M. Hanfland, H. Beister, and K. Syassen, [Phys Rev B](#) **39**, 12598 (1989).
- 1624 <sup>29</sup>L. Zhenxian, W. Lizhong, Z. Yongnian, C. Qilang, and Z. Guangtian, [J Phys Cond Mat](#)  
1625 **2**, 8083 (1990).
- 1626 <sup>30</sup>M. Peña-Álvarez, E. del Corro, V. G. Baonza, and M. Taravillo, [J Phys Chem C](#) **118**,  
1627 **25132** (2014).
- 1628 <sup>31</sup>F. Ding, H. Ji, Y. Chen, A. Herklotz, K. Dörr, Y. Mei, A. Rastelli, and O. G. Schmidt,  
1629 [Nano Lett](#) **10**, 3453 (2010).
- 1630 <sup>32</sup>M. S. Dresselhaus, A. Jorio, M. Hofmann, G. Dresselhaus, and R. Saito, [Nano Letters](#)  
1631 **10**, 751 (2010).
- 1632 <sup>33</sup>T. M. G. Mohiuddin, A. Lombardo, R. R. Nair, A. Bonetti, G. Savini, R. Jalil, N. Bonini,  
1633 D. M. Basko, C. Galiotis, N. Marzari, K. S. Novoselov, A. K. Geim, and A. C. Ferrari,  
1634 [Phys Rev B](#) **79**, 205433 (2009).
- 1635 <sup>34</sup>J. E. Proctor, E. Gregoryanz, K. S. Novoselov, M. Lotya, J. N. Coleman, and M. P.  
1636 Halsall, [Phys Rev B](#) **80**, 073408 (2009).
- 1637 <sup>35</sup>Y. W. Sun, D. Holec, D. Gehringer, O. Fenwick, D. J. Dunstan, and C. J. Humphreys,  
1638 [Phys. Rev. B](#) **101**, 125421 (2020).
- 1639 <sup>36</sup>J. Nicolle, D. Machon, P. Poncharal, O. Pierre-Louis, and A. San-Miguel, [Nano Lett](#) **11**,  
1640 **3564** (2011).
- 1641 <sup>37</sup>K. Filintoglou, N. Papadopoulos, J. Arvanitidis, D. Christofilos, O. Frank, M. Kalbac,  
1642 J. Parthenios, G. Kalosakas, C. Galiotis, and K. Papagelis, [Phys Rev B](#) **88**, 045418  
1643 (2013).
- 1644 <sup>38</sup>C. Bousige, F. Balima, D. Machon, G. S. Pinheiro, A. Torres-Dias, J. Nicolle, D. Kalita,  
1645 N. Bendiab, L. Marty, V. Bouchiat, G. Montagnac, A. Gomes de Souza Filho, P. Pon-  
1646 charal, and A. San-Miguel, [Nano Lett](#) **17**, 21 (2017).
- 1647 <sup>39</sup>Y. W. Sun, D. J. Dunstan, M. A. Hartmann, and D. Holec, [PAMM](#) **13**, 7 (2013).
- 1648 <sup>40</sup>Y. Sun, W. Liu, I. Hernandez, J. Gonzalez, F. Rodriguez, D. Dunstan, and C. Humphreys,  
1649 [Physical Review Letters](#) **123**, 135501 (2019).

- 1650 <sup>41</sup>R. Al-Jishi and G. Dresselhaus, [Phys. Rev. B](#) **26**, 4514 (1982).
- 1651 <sup>42</sup>R. Nicklow, N. Wakabayashi, and H. G. Smith, [Phys. Rev. B](#) **5**, 4951 (1972).
- 1652 <sup>43</sup>R. Saito, G. Dresselhaus, and M. Dresselhaus, *Physical Properties of Carbon Nanotubes*  
1653 (Imperial College Press, 1998).
- 1654 <sup>44</sup>S. Siebentritt, R. Pues, K.-H. Rieder, and A. M. Shikin, [Phys. Rev. B](#) **55**, 7927 (1997).
- 1655 <sup>45</sup>A. C. Torres-Dias, T. F. Cerqueira, W. Cui, M. A. Marques, S. Botti, D. Machon, M. A.  
1656 Hartmann, Y. Sun, D. J. Dunstan, and A. San-Miguel, [Carbon](#) **123**, 145 (2017).
- 1657 <sup>46</sup>A. H. Castro Neto, F. Guinea, N. M. R. Peres, K. S. Novoselov, and A. K. Geim, [Reviews](#)  
1658 [of Modern Physics](#) **81**, 109 (2009).
- 1659 <sup>47</sup>A. K. Geim and K. S. Novoselov, [Nature Materials](#) **6**, 183 (2007).
- 1660 <sup>48</sup>L. Shi, P. Rohringer, M. Wanko, A. Rubio, S. Waßerroth, S. Reich, S. Cambré, W. Wense-  
1661 leers, P. Ayala, and T. Pichler, [Phys. Rev. Materials](#) **1**, 075601 (2017).
- 1662 <sup>49</sup>Y. Hernandez, V. Nicolosi, M. Lotya, F. M. Blighe, Z. Sun, S. De, I. McGovern, B. Hol-  
1663 land, M. Byrne, Y. K. Gun'Ko, J. J. Boland, P. Niraj, G. Duesberg, S. Krishnamurthy,  
1664 R. Goodhue, J. Hutchison, V. Scardaci, A. C. Ferrari, and J. N. Coleman, [Nature Nan-](#)  
1665 [otechnology](#) **3**, 563 (2008).
- 1666 <sup>50</sup>A. Fasolino, J. H. Los, and M. I. Katsnelson, [Nat. Mater.](#) **6**, 858 (2007).
- 1667 <sup>51</sup>J. C. Meyer, A. K. Geim, M. I. Katsnelson, K. S. Novoselov, D. Obergfell, S. Roth,  
1668 C. Girit, and A. Zettl, [Solid State Communications Exploring graphene](#), **143**, 101 (2007).
- 1669 <sup>52</sup>R. Zan, C. Muryn, U. Bangert, P. Mattocks, P. Wincott, D. Vaughan, X. Li, L. Colombo,  
1670 R. S. Ruoff, B. Hamilton, and K. S. Novoselov, [Nanoscale](#) **4**, 3065 (2012).
- 1671 <sup>53</sup>O. M. Marago, F. Bonaccorso, R. Saija, G. Privitera, P. G. Gucciardi, G. Iati, Maria  
1672 A. and Calogero, P. H. Jones, F. Borghese, P. Denti, V. Nicolosi, and A. C. Ferrari, [ACS](#)  
1673 [Nano](#) **4**, 7515 (2010).
- 1674 <sup>54</sup>P. Thibado, P. Kumar, S. Singh, M. Ruiz-Garcia, A. Lasanta, and L. Bonilla, [Physical](#)  
1675 [Review E](#) **102**, 042101 (2020).
- 1676 <sup>55</sup>J. M. Carlsson, [Nature Materials](#) **6**, 801 (2007).
- 1677 <sup>56</sup>J. E. Proctor, D. M. Armada, and A. Vijayaraghavan, *An Introduction to Graphene and*  
1678 *Carbon Nanotubes* (CRC Press, 2017).
- 1679 <sup>57</sup>P. R. Shaina, L. George, V. Yadav, and M. Jaiswal, [J. Phys.: Condens. Matter](#) **28**,  
1680 [085301](#) (2016).

- 1681 <sup>58</sup>F. Jean, T. Zhou, N. Blanc, R. Felici, J. Coraux, and G. Renaud, [Phys. Rev. B \*\*88\*\*,](#)  
1682 [165406 \(2013\)](#).
- 1683 <sup>59</sup>H. Pierson, *Handbook of Carbon, Graphite, Diamond and Fullerenes: Properties, Process-*  
1684 *ing and Applications* (Noyes Publications, 1993).
- 1685 <sup>60</sup>A. Bailey and B. Yates, [Journal of Applied Physics \*\*41\*\*,](#) 5088 (1970).
- 1686 <sup>61</sup>B. Marsden, A. Mummery, and P. Mummery, [Proc. R. Soc. A. \*\*474\*\*,](#) 20180075 (2018).
- 1687 <sup>62</sup>Z. H. Ni, W. Chen, X. F. Fan, J. L. Kuo, T. Yu, A. T. S. Wee, and Z. X. Shen, [Phys.](#)  
1688 [Rev. B \*\*77\*\*,](#) 115416 (2008).
- 1689 <sup>63</sup>M. Senn, A. Bombardi, C. Murray, C. Vecchini, A. Scherillo, X. Luo, and S. Cheong,  
1690 [Phys. Rev. Lett. \*\*114\*\*,](#) 035701 (2015).
- 1691 <sup>64</sup>W. Miller, C. W. Smith, D. S. Mackenzie, and K. E. Evans, [J Mater Sci \*\*44\*\*,](#) 5441 (2009).
- 1692 <sup>65</sup>M. T. Dove and H. Fang, [Rep. Prog. Phys. \*\*79\*\*,](#) 066503 (2016).
- 1693 <sup>66</sup>L. Wang, Q. Zheng, J. Z. Liu, and Q. Jiang, [Phys. Rev. Lett. \*\*95\*\*,](#) 105501 (2005).
- 1694 <sup>67</sup>Y. Huang, J. Wu, and K. C. Hwang, [Phys. Rev. B \*\*74\*\*,](#) 245413 (2006).
- 1695 <sup>68</sup>O. A. Shenderova, V. V. Zhirnov, and D. W. Brenner, [Critical Reviews in Solid State](#)  
1696 [and Materials Sciences \*\*27\*\*,](#) 227 (2002).
- 1697 <sup>69</sup>M. A. Hartmann, M. Todt, F. G. Rammerstorfer, F. D. Fischer, and O. Paris, [EPL \*\*103\*\*,](#)  
1698 [68004 \(2013\)](#).
- 1699 <sup>70</sup>M. M. J. Treacy, T. W. Ebbesen, and J. M. Gibson, [Nature \*\*381\*\*,](#) 678 (1996).
- 1700 <sup>71</sup>D.-B. Zhang, E. Akatyeva, and T. Dumitrică, [Phys. Rev. Lett. \*\*106\*\*,](#) 255503 (2011).
- 1701 <sup>72</sup>J. Peng, J. Wu, K. C. Hwang, J. Song, and Y. Huang, [Journal of the Mechanics and](#)  
1702 [Physics of Solids \*\*56\*\*,](#) 2213 (2008).
- 1703 <sup>73</sup>D. Sen, K. S. Novoselov, P. M. Reis, and M. J. Buehler, [Small \*\*6\*\*,](#) 1108 (2010).
- 1704 <sup>74</sup>A. Politano, A. R. Marino, D. Campi, D. Farías, R. Miranda, and G. Chiarello, [Carbon](#)  
1705 [50,](#) 4903 (2012).
- 1706 <sup>75</sup>M. K. Bles, A. W. Barnard, P. A. Rose, S. P. Roberts, K. L. McGill, P. Y. Huang, A. R.  
1707 Ruyack, J. W. Kevek, B. Kobrin, D. A. Muller, *et al.*, [Nature \*\*524\*\*,](#) 204 (2015).
- 1708 <sup>76</sup>N. Lindahl, D. Midtvedt, J. Svensson, O. A. Nerushev, N. Lindvall, A. Isacson, and  
1709 E. E. B. Campbell, [Nano Lett. \*\*12\*\*,](#) 3526 (2012).
- 1710 <sup>77</sup>D. Carter, D. Dunstan, W. Just, O. Bandtlow, and A. S. Miguel, (2020),  
1711 [arXiv:2011.14120 \[cond-mat.other\]](#).

- 1712 <sup>78</sup>C. Zhang, K. Bets, S. S. Lee, Z. Sun, F. Mirri, V. L. Colvin, B. I. Yakobson, J. M. Tour,  
1713 and R. H. Hauge, *ACS Nano* **6**, 6023 (2012).
- 1714 <sup>79</sup>A. Impellizzeri, P. Briddon, and C. Ewels, *Physical Review B* **100**, 115410 (2019).
- 1715 <sup>80</sup>J. Zhang, J. Xiao, X. Meng, C. Monroe, Y. Huang, and J.-M. Zuo, *Physical Review*  
1716 *Letters* **104**, 166805 (2010).
- 1717 <sup>81</sup>Z. Liu, K. Suenaga, P. J. Harris, and S. Iijima, *Physical Review Letters* **102**, 015501  
1718 (2009).
- 1719 <sup>82</sup>S. Cranford, D. Sen, and M. J. Buehler, *Applied Physics Letters* **95**, 123121 (2009).
- 1720 <sup>83</sup>X. Chen, C. Yi, and C. Ke, *Applied Physics Letters* **106**, 101907 (2015).
- 1721 <sup>84</sup>D.-B. Zhang, E. Akatyeva, and T. Dumitrică, *Physical Review Letters* **106**, 255503  
1722 (2011).
- 1723 <sup>85</sup>P. H. Tan, W. P. Han, W. J. Zhao, Z. H. Wu, K. Chang, H. Wang, Y. F. Wang, N. Bonini,  
1724 N. Marzari, N. Pugno, and et al., *Nat. Mater* **11**, 294 (2012).
- 1725 <sup>86</sup>C. Lee, Q. Li, W. Kalb, X.-Z. Liu, H. Berger, R. W. Carpick, and J. Hone, *Science* **328**,  
1726 76 (2010).
- 1727 <sup>87</sup>W. Gao and A. Tkatchenko, *Physical Review Letters* **114**, 096101 (2015).
- 1728 <sup>88</sup>J. H. Kim, J. H. Jeong, N. Kim, R. Joshi, and G.-H. Lee, *J. Phys. D: Appl. Phys.* **52**,  
1729 083001 (2018).
- 1730 <sup>89</sup>D. G. Papageorgiou, Z. Li, M. Liu, I. A. Kinloch, and R. J. Young, *Nanoscale* **12**, 2228  
1731 (2020).
- 1732 <sup>90</sup>H. Zhan, D. Guo, and G. Xie, *Nanoscale* **11**, 13181 (2019).
- 1733 <sup>91</sup>C. Jin, A. Davoodabadi, J. Li, Y. Wang, and T. Singler, *Journal of the Mechanics and*  
1734 *Physics of Solids* **100**, 85 (2017).
- 1735 <sup>92</sup>M. W. Pruessner, T. T. King, D. P. Kelly, R. Grover, L. C. Calhoun, and R. Ghodssi,  
1736 *Sensors and Actuators A: Physical* **105**, 190 (2003).
- 1737 <sup>93</sup>J. Han, N. M. Pugno, and S. Ryu, *Nanoscale* **7**, 15672 (2015).
- 1738 <sup>94</sup>R. J. T. Nicholl, H. J. Conley, N. V. Lavrik, I. Vlassiuk, Y. S. Puzyrev, V. P. Sreenivas,  
1739 S. T. Pantelides, and K. I. Bolotin, *Nature Communications* **6**, 8789 (2015).
- 1740 <sup>95</sup>C. S. Ruiz-Vargas, H. L. Zhuang, P. Y. Huang, A. M. van der Zande, S. Garg, P. L.  
1741 McEuen, D. A. Muller, R. G. Hennig, and J. Park, *Nano Lett.* **11**, 2259 (2011).
- 1742 <sup>96</sup>T. Cui, S. Mukherjee, P. M. Sudeep, G. Colas, F. Najafi, J. Tam, P. M. Ajayan, C. V.  
1743 Singh, Y. Sun, and T. Filleter, *Nature Materials* **19**, 405 (2020).

- 1744 <sup>97</sup>X. Zhao, D. G. Papageorgiou, L. Zhu, F. Ding, and R. J. Young, [Nanoscale](#) **11**, 14339  
1745 (2019).
- 1746 <sup>98</sup>K. Cao, S. Feng, Y. Han, L. Gao, T. Hue Ly, Z. Xu, and Y. Lu, [Nature Communications](#)  
1747 **11**, 284 (2020).
- 1748 <sup>99</sup>G. Wang, Z. Dai, Y. Wang, P. Tan, L. Liu, Z. Xu, Y. Wei, R. Huang, and Z. Zhang,  
1749 [Phys. Rev. Lett.](#) **119**, 036101 (2017).
- 1750 <sup>100</sup>G. Tsoukleri, J. Parthenios, K. Papagelis, R. Jalil, A. C. Ferrari, A. K. Geim, K. S.  
1751 Novoselov, and C. Galiotis, [Small](#) **5**, 2397 (2009).
- 1752 <sup>101</sup>Z. Li, R. J. Young, D. G. Papageorgiou, I. A. Kinloch, X. Zhao, C. Yang, and S. Hao,  
1753 [2D Mater.](#) **6**, 045026 (2019).
- 1754 <sup>102</sup>A. C. Ferrari, J. C. Meyer, V. Scardaci, C. Casiraghi, M. Lazzeri, F. Mauri, S. Piscanec,  
1755 D. Jiang, K. S. Novoselov, S. Roth, and et al., [Phys Rev Lett](#) **97** (2006), 10.1103/phys-  
1756 revlett.97.187401.
- 1757 <sup>103</sup>Y. Shin, M. Lozada Hidalgo, J. L. Sambricio Garcia, I. Grigorieva, A. Geim, and C. Casir-  
1758 aghi, [Appl Phys Lett](#) **108**, 221907 (2016).
- 1759 <sup>104</sup>C. Neumann, S. Reichardt, P. Venezuela, M. Drögeler, L. Banszerus, M. Schmitz,  
1760 K. Watanabe, T. Taniguchi, F. Mauri, B. Beschoten, *et al.*, [Nature Communications](#)  
1761 **6**, 1 (2015).
- 1762 <sup>105</sup>L. Gong, R. J. Young, I. A. Kinloch, I. Riaz, R. Jalil, and K. S. Novoselov, [ACS Nano](#)  
1763 **6**, 2086 (2012).
- 1764 <sup>106</sup>J. Zabel, R. R. Nair, A. Ott, T. Georgiou, A. K. Geim, K. S. Novoselov, and C. Casiraghi,  
1765 [Nano Letters](#) **12**, 617 (2012).
- 1766 <sup>107</sup>J.-B. Wu, Z.-X. Hu, X. Zhang, W.-P. Han, Y. Lu, W. Shi, X.-F. Qiao, M. Ijiäs, S. Milana,  
1767 W. Ji, A. C. Ferrari, and P.-H. Tan, [ACS Nano](#) **9**, 7440 (2015).
- 1768 <sup>108</sup>H. Kataura, Y. Kumazawa, Y. Maniwa, I. Umezumi, S. Suzuki, Y. Ohtsuka, and Y. Achiba,  
1769 [Synth Met](#) **103**, 2555 (1999).
- 1770 <sup>109</sup>I. Brihuega, P. Mallet, H. González-Herrero, G. Trambly de Laissardière, M. M. Ugeda,  
1771 L. Magaud, J. M. Gómez-Rodríguez, F. Ynduráin, and J.-Y. Veuillen, [Physical Review](#)  
1772 [Letters](#) **109** (2012), 10.1103/PhysRevLett.109.196802.
- 1773 <sup>110</sup>P. Zhang, L. Ma, F. Fan, Z. Zeng, C. Peng, P. E. Loya, Z. Liu, Y. Gong, J. Zhang,  
1774 X. Zhang, P. M. Ajayan, T. Zhu, and J. Lou, [Nature Communications](#) **5**, 3782 (2014).

- 1775 <sup>111</sup>M. Fujihara, R. Inoue, R. Kurita, T. Taniuchi, Y. Motoyui, S. Shin, F. Komori,  
1776 Y. Maniwa, H. Shinohara, and Y. Miyata, [ACS Nano](#) **9**, 9027 (2015).
- 1777 <sup>112</sup>K. Kim, V. I. Artyukhov, W. Regan, Y. Liu, M. F. Crommie, B. I. Yakobson, and  
1778 A. Zettl, [Nano Lett.](#) **12**, 293 (2012).
- 1779 <sup>113</sup>J. Williams, [International Journal of Fracture](#) **87**, 265 (1997).
- 1780 <sup>114</sup>S. P. Koenig, N. G. Boddeti, M. L. Dunn, and J. S. Bunch, [Nature Nanotechnology](#) **6**,  
1781 543 (2011).
- 1782 <sup>115</sup>N. G. Boddeti, S. P. Koenig, R. Long, J. Xiao, J. S. Bunch, and M. L. Dunn, [Journal of](#)  
1783 [Applied Mechanics](#) **80** (2013), 10.1115/1.4024255.
- 1784 <sup>116</sup>J. Hass, F. Varchon, J. E. Millán-Otoya, M. Sprinkle, N. Sharma, W. A. de Heer,  
1785 C. Berger, P. N. First, L. Magaud, and E. H. Conrad, [Phys. Rev. Lett.](#) **100**, 125504  
1786 (2008).
- 1787 <sup>117</sup>B. A. Auld, *Acoustic Fields and Waves in Solids* (Wiley, 1973).
- 1788 <sup>118</sup>K. H. Michel and B. Verberck, [Phys. Status Solidi B](#) **245**, 2177 (2008).
- 1789 <sup>119</sup>F. Memarian, A. Fereidoon, and M. Darvish Ganji, [Superlattices and Microstructures](#)  
1790 **85**, 348 (2015).
- 1791 <sup>120</sup>B. D. Jensen, K. E. Wise, and G. M. Odegard, [J. Phys. Chem. A](#) **119**, 9710 (2015).
- 1792 <sup>121</sup>G. Kalosakas, N. N. Lathiotakis, C. Galiotis, and K. Papagelis, [Journal of Applied Physics](#)  
1793 **113**, 134307 (2013).
- 1794 <sup>122</sup>I. V. Lebedeva, A. S. Minkin, A. M. Popov, and A. A. Knizhnik, [Physica E: Low-](#)  
1795 [dimensional Systems and Nanostructures](#) **108**, 326 (2019).
- 1796 <sup>123</sup>G. Gui, J. Li, and J. Zhong, [Phys. Rev. B](#) **78**, 075435 (2008).
- 1797 <sup>124</sup>F. Liu, P. Ming, and J. Li, [Phys. Rev. B](#) **76**, 064120 (2007).
- 1798 <sup>125</sup>L. Zhou and G. Cao, [Phys. Chem. Chem. Phys.](#) **18**, 1657 (2016).
- 1799 <sup>126</sup>J. Pellicer-Porres, A. Segura, C. Ferrer, V. Muñoz, A. San Miguel, A. Polian, J. P. Itié,  
1800 M. Gauthier, and S. Pascarelli, [Phys. Rev. B](#) **65**, 174103 (2002).
- 1801 <sup>127</sup>S. Deng and V. Berry, [Materials Today](#) **19**, 197 (2016).
- 1802 <sup>128</sup>J. C. Meyer, A. K. Geim, M. I. Katsnelson, K. S. Novoselov, T. J. Booth, and S. Roth,  
1803 [Nature](#) **446**, 60 (2007).
- 1804 <sup>129</sup>J. S. Bunch, S. S. Verbridge, J. S. Alden, A. M. van der Zande, J. M. Parpia, H. G.  
1805 Craighead, and P. L. McEuen, [Nano Letters](#) **8**, 2458 (2008).
- 1806 <sup>130</sup>Z. Lu and M. L. Dunn, [Journal of Applied Physics](#) **107**, 044301 (2010).

1807 <sup>131</sup>Z. Tao, J. Du, Z. Qi, K. Ni, S. Jiang, and Y. Zhu, [Appl. Phys. Lett.](#) **116**, 133101 (2020).

1808 <sup>132</sup>J. Nicolle, *Etude Du Graphène Sous Pression Par Spectroscopie Raman*, Ph.D. thesis,  
1809 Université Claude Bernard Lyon 1 (2011).

1810 <sup>133</sup>A. Forestier, F. Balima, C. Bousige, G. d. S. Pinheiro, R. Fulcrand, M. Kalbáč, D. Machon,  
1811 and A. San-Miguel, [J. Phys. Chem. C](#) **124**, 11193 (2020).

1812 <sup>134</sup>L. G. P. Martins, M. J. S. Matos, A. R. Paschoal, P. T. C. Freire, N. F. Andrade, A. L.  
1813 Aguiar, J. Kong, B. R. A. Neves, A. B. de Oliveira, M. S. Mazzoni, and et al., [Nat.](#)  
1814 [Comm](#) **8** (2017), 10.1038/s41467-017-00149-8.

1815 <sup>135</sup>A. Das, S. Pisana, B. Chakraborty, S. Piscanec, S. K. Saha, U. V. Waghmare, K. S.  
1816 Novoselov, H. R. Krishnamurthy, A. K. Geim, A. C. Ferrari, and A. K. Sood, [Nature](#)  
1817 [Nanotech](#) **3**, 210 (2008).

1818 <sup>136</sup>M. J. Longhurst and N. Quirke, [Phys. Rev. Lett.](#) **98**, 145503 (2007).

1819 <sup>137</sup>W. Cui, T. F. T. Cerqueira, S. Botti, M. A. L. Marques, and A. San-Miguel, [Phys. Chem.](#)  
1820 [Chem. Phys.](#) **18**, 19926 (2016).

1821 <sup>138</sup>S. Azadi and R. E. Cohen, [J. Chem. Phys.](#) **145**, 064501 (2016).

1822 <sup>139</sup>J.-U. Lee, D. Yoon, and H. Cheong, [Nano Lett.](#) **12**, 4444 (2012).

1823 <sup>140</sup>D. Davidovikj, F. Alijani, S. J. Cartamil-Bueno, H. S. J. van der Zant, M. Amabili, and  
1824 P. G. Steeneken, [Nat Commun](#) **8**, 1 (2017).

1825 <sup>141</sup>B. Sajadi, F. Alijani, D. Davidovikj, J. H. Goosen, P. G. Steeneken, and F. van Keulen,  
1826 [Journal of Applied Physics](#) **122**, 234302 (2017).

1827 <sup>142</sup>B. Sajadi, S. van Hemert, B. Arash, P. Belardinelli, P. G. Steeneken, and F. Alijani,  
1828 [Carbon](#) **139**, 334 (2018).

1829 <sup>143</sup>P. Lambin, [Appl. Sci.](#) **4**, 282 (2014).

1830 <sup>144</sup>P. Lambin, [Applied Sciences](#) **7**, 830 (2017).

1831 <sup>145</sup>O. Pierre-Louis, [Phys Rev E](#) **78**, 021603 (2008).

1832 <sup>146</sup>D. Machon, C. Bousige, R. Alencar, A. Torres-Dias, F. Balima, J. Nicolle, G. Pinheiro de  
1833 Sousa, A. G. de Souza Filho, and A. San-Miguel, [J Raman Spectrosc](#) **49**, 121 (2018).

1834 <sup>147</sup>A. Reserbat-Plantey, D. Kalita, Z. Han, L. Ferlazzo, S. Autier-Laurent, K. Komatsu,  
1835 C. Li, R. Weil, A. Ralko, L. Marty, S. Guéron, N. Bendiab, H. Bouchiat, and V. Bouchiat,  
1836 [Nano Lett](#) **14**, 5044 (2014).

1837 <sup>148</sup>A. Forestier, *Dimensionality effects in graphene at high hydrostatic pressure*, Ph.D. thesis,  
1838 Université Claude Bernard Lyon 1 (2020).

- 1839 <sup>149</sup>R. S. Alencar, K. D. A. Saboia, D. Machon, G. Montagnac, V. Meunier, O. P. Ferreira,  
1840 A. San-Miguel, and A. G. Souza Filho, *Phys Rev Mater.* **1** (2017), [10.1103/physrevma-](https://doi.org/10.1103/physrevmaterials.1.024002)  
1841 [terials.1.024002](https://doi.org/10.1103/physrevmaterials.1.024002).
- 1842 <sup>150</sup>D. Y. Usachov, V. Y. Davydov, V. S. Levitskii, V. O. Shevelev, D. Marchenko, B. V.  
1843 Senkovskiy, O. Y. Vilkov, A. G. Rybkin, L. V. Yashina, E. V. Chulkov, I. Y. Sklyadneva,  
1844 R. Heid, K.-P. Bohnen, C. Laubschat, and D. V. Vyalikh, *ACS Nano* **11**, 6336 (2017).
- 1845 <sup>151</sup>N. Bendiab, J. Renard, C. Schwarz, A. Reserbat-Plantey, L. Djevahirdjian, V. Bouchiat,  
1846 J. Coraux, and L. Marty, *J. Raman Spectrosc.* **49**, 130 (2018).
- 1847 <sup>152</sup>J. E. Lee, G. Ahn, J. Shim, Y. S. Lee, and S. Ryu, *Nat. Comm* **3**, 1024 (2012).
- 1848 <sup>153</sup>C. Thomsen, S. Reich, and P. Ordejón, *Phys Rev B* **65**, 073403 (2002).
- 1849 <sup>154</sup>W. Cui, T. F. T. Cerqueira, S. Botti, M. A. L. Marques, and A. San-Miguel, *Phys Chem*  
1850 *Chem Phys* **18**, 19926 (2016).
- 1851 <sup>155</sup>S. Klotz, J. Chervin, P. Munsch, and G. Le Marchand, *J Phys Appl Phys* **42**, 075413  
1852 (2009).
- 1853 <sup>156</sup>R. J. Young, L. Gong, I. A. Kinloch, I. Riaz, R. Jalil, and K. S. Novoselov, *ACS Nano*  
1854 **5**, 3079 (2011), pMID: 21395299.
- 1855 <sup>157</sup>R. J. Young, I. A. Kinloch, L. Gong, and K. S. Novoselov, *Composites Science and*  
1856 *Technology* **72**, 1459 (2012).
- 1857 <sup>158</sup>F. Piazza, K. Cruz, M. Monthieux, P. Puech, and I. Gerber, *Carbon* **169**, 129 (2020).
- 1858 <sup>159</sup>P. V. Bakharev, M. Huang, M. Saxena, S. W. Lee, S. H. Joo, S. O. Park, J. Dong, D. C.  
1859 Camacho-Mojica, S. Jin, Y. Kwon, *et al.*, *Nature Nanotechnology* **15**, 59 (2020).
- 1860 <sup>160</sup>J. W. Suk, R. D. Piner, J. An, and R. S. Ruoff, *ACS Nano* **4**, 6557 (2010).
- 1861 <sup>161</sup>L. A. Chernozatonskii, P. B. Sorokin, A. A. Kuzubov, B. P. Sorokin, A. G. Kvashnin,  
1862 D. G. Kvashnin, P. V. Avramov, and B. I. Yakobson, *Journal of Physical Chemistry C*  
1863 **115**, 132 (2011).
- 1864 <sup>162</sup>A. R. Khoei and M. S. Khorrami, *Fullerenes, Nanotubes and Carbon Nanostructures* **24**,  
1865 [594](https://doi.org/10.1080/15339075.2016.1191111) (2016).
- 1866 <sup>163</sup>I. Razado-Colambo, J. Avila, D. Vignaud, S. Godey, X. Wallart, D. P. Woodruff, and  
1867 M. C. Asensio, *Scientific Reports* **8**, 10190 (2018).
- 1868 <sup>164</sup>F. Varchon, R. Feng, J. Hass, X. Li, B. N. Nguyen, C. Naud, P. Mallet, J.-Y. Veuillein,  
1869 C. Berger, E. H. Conrad, and L. Magaud, *Phys. Rev. Lett.* **99**, 126805 (2007).

- 1870 <sup>165</sup>S. Reich and C. Thomsen, *Philosophical Transactions of the Royal Society of London.*  
1871 *Series A: Mathematical, Physical and Engineering Sciences* **362**, 2271 (2004).
- 1872 <sup>166</sup>M. Huang, H. Yan, C. Chen, D. Song, T. F. Heinz, and J. Hone, *Proceedings of the*  
1873 *National Academy of Sciences* **106**, 7304 (2009).
- 1874 <sup>167</sup>Y. W. Sun, D. Holec, and D. J. Dunstan, *Physical Review B* **92** (2015), 10.1103/Phys-  
1875 *RevB.92.094108*.
- 1876 <sup>168</sup>R. A. Friedel and G. L. Carlson, *J. Phys. Chem.* **75**, 1149 (1971).
- 1877 <sup>169</sup>S. Piscanec, M. Lazzeri, J. Robertson, A. C. Ferrari, and F. Mauri, *Physical Review B*  
1878 **75**, 035427 (2007).
- 1879 <sup>170</sup>J. Zabel, R. R. Nair, A. Ott, T. Georgiou, A. K. Geim, K. S. Novoselov, and C. Casiraghi,  
1880 *Nano Lett* **12**, 617 (2012).
- 1881 <sup>171</sup>V. N. Popov, *New J. Phys.* **6**, 17 (2004).
- 1882 <sup>172</sup>J. Maultzsch, H. Telg, S. Reich, and C. Thomsen, *Phys. Rev. B* **72**, 205438 (2005).
- 1883 <sup>173</sup>G. Mahan, *Physical Review B* **65**, 235402 (2002).
- 1884 <sup>174</sup>S. M. Bachilo, M. S. Strano, C. Kittrell, R. H. Hauge, R. E. Smalley, and R. B. Weisman,  
1885 *Science* **298**, 2361 (2002).
- 1886 <sup>175</sup>I. C. Gerber, P. Puech, A. Gannouni, and W. Bacsa, *Physical Review B* **79**, 075423  
1887 (2009).
- 1888 <sup>176</sup>Y. Shen and D. Zerulla, *Phys. Rev. B* **95**, 205434 (2017).
- 1889 <sup>177</sup>A. J. Ghandour, D. J. Dunstan, and A. Sapelkin, *J. Raman Spectrosc.* **42**, 1611 (2011).
- 1890 <sup>178</sup>J. E. Proctor, M. P. Halsall, A. Ghandour, and D. J. Dunstan, *Journal of Physics and*  
1891 *Chemistry of Solids* **67**, 2468 (2006).
- 1892 <sup>179</sup>C. Thomsen, S. Reich, H. Jantoljak, I. Loa, K. Syassen, M. Burghard, G. Duesberg, and  
1893 S. Roth, *Applied Physics A: Materials Science & Processing* **69**, 309 (1999).
- 1894 <sup>180</sup>D. Christofilos, J. Arvanitidis, C. Tzampazis, K. Papagelis, T. Takenobu, Y. Iwasa,  
1895 H. Kataura, C. Lioutas, S. Ves, and G. Kourouklis, *Diamond and Related Materials*  
1896 **15**, 1075 (2006).
- 1897 <sup>181</sup>P. Djondjorov, V. Vassilev, and I. Mladenov, *International Journal of Mechanical Sciences*  
1898 **53**, 355 (2011).
- 1899 <sup>182</sup>V. M. Vassilev, P. A. Djondjorov, and I. M. Mladenov, *Journal of Applied Physics* **117**,  
1900 **196101** (2015).

1901 <sup>183</sup>J. A. Elliott, J. K. W. Sandler, A. H. Windle, R. J. Young, and M. S. P. Shaffer, *Phys.*  
1902 *Rev. Lett.* **92**, 095501 (2004).

1903 <sup>184</sup>N. Wang, Z.-K. Tang, G.-D. Li, and J. Chen, *Nature* **408**, 50 (2000).

1904 <sup>185</sup>H. R. Barzegar, A. Yan, S. Coh, E. Gracia-Espino, C. Ojeda-Aristizabal, G. Dunn, M. L.  
1905 Cohen, S. G. Louie, T. Wågberg, and A. Zettl, *Nano Research* **10**, 1942 (2017).

1906 <sup>186</sup>A. Impellizzeri, P. Briddon, and C. Ewels, *Physical Review B* **100**, 115410 (2019).

1907 <sup>187</sup>R. R. Del Grande, A. F. Fonseca, and R. B. Capaz, *Carbon* **159**, 161 (2020).

1908 <sup>188</sup>A. Barboza, H. Chacham, and B. Neves, *Physical Review Letters* **102**, 025501 (2009).

1909 <sup>189</sup>T. C. Hirschmann, P. T. Araujo, H. Muramatsu, J. F. Rodriguez-Nieva, M. Seifert,  
1910 K. Nielsch, Y. A. Kim, and M. S. Dresselhaus, *ACS Nano* **8**, 1330 (2014).

1911 <sup>190</sup>A. Aguiar, E. Barros, R. Capaz, A. Souza Filho, P. Freire, J. M. Filho, D. Machon,  
1912 C. Caillier, Y. Kim, H. Muramatsu, M. Endo, and A. San-Miguel, *J. Phys. Chem. C*  
1913 **115**, 5378 (2011).

1914 <sup>191</sup>P. Puech, H. Hubel, D. J. Dunstan, R. Bacsá, C. Laurent, and W. Bacsá, *Physical Review*  
1915 *Letters* **93**, 095506 (2004).

1916 <sup>192</sup>J. González, C. Power, E. Belandria, J. Jorge, F. Gonzalez-Jimenez, M. Millot, S. Nanot,  
1917 J. M. Broto, and E. Flahaut, *High Pressure Research* **28**, 577 (2008).

1918 <sup>193</sup>A. J. Ghandour, I. F. Crowe, J. E. Proctor, Y. W. Sun, M. P. Halsall, I. Hernandez,  
1919 A. Sapelkin, and D. J. Dunstan, *Phys. Rev. B* **87**, 085416 (2013).

1920 <sup>194</sup>P. N. Keating, *Phys. Rev.* **145**, 637 (1966).

1921 <sup>195</sup>J. Maultzsch, S. Reich, C. Thomsen, H. Requardt, and P. Ordejón, *Physical Review*  
1922 *Letters* **92**, 075501 (2004).

1923 <sup>196</sup>A. Lajevardipour, M. Neek-Amal, and F. M. Peeters, *J. Phys.: Condens. Matter* **24**,  
1924 **175303** (2012), publisher: IOP Publishing.

1925 <sup>197</sup>D. L. Nika and A. A. Balandin, *J. Phys.: Condens. Matter* **24**, 233203 (2012).

1926 <sup>198</sup>D. W. Brenner, O. A. Shenderova, J. A. Harrison, S. J. Stuart, B. Ni, and S. B. Sinnott,  
1927 *Journal of Physics: Condensed Matter* **14**, 783 (2002).

1928 <sup>199</sup>S. G. Srinivasan, A. C. Van Duin, and P. Ganesh, *The Journal of Physical Chemistry A*  
1929 **119**, 571 (2015).

1930 <sup>200</sup>W. Duan, Q. Wang, K. M. Liew, and X. He, *Carbon* **45**, 1769 (2007).

1931 <sup>201</sup>S. Reich, J. Maultzsch, C. Thomsen, and P. Ordejon, *Physical Review B* **66**, 035412  
1932 (2002).